Exploring the Dynamics of Convection-Driven Dynamos in Rotating Spherical Shells

Parag Gupta

SUBMITTED IN FULFILMENT OF THE REQUIREMENTS FOR THE DEGREE
OF
DOCTOR OF PHILOSOPHY

SCHOOL OF MATHEMATICS AND STATISTICS

COLLEGE OF SCIENCE AND ENGINEERING

JULY 2024

To my family for their constant support, and to my supervisors and colleagues for guiding and inspiring me throughout this journey.

Abstract

This thesis explores the dynamics of convection-driven dynamos in rotating spherical shells through three detailed studies. The first study investigates the relative importance of helicity and cross-helicity electromotive dynamo effects for the self-sustained generation of magnetic fields by chaotic thermal convection in rotating spherical shells as a function of shell thickness. Direct numerical simulations reveal two distinct branches of dynamo solutions coexisting for shell aspect ratios between 0.25 and 0.6: a mean-field dipolar regime and a fluctuating dipolar regime. The study compares and contrasts the properties of these coexisting dynamo attractors, including differences in temporal behavior and the spatial structures of both magnetic fields and rotating thermal convection. In the fluctuating dipolar regime, the helicity α-effect and the cross-helicity γ-effect are found to be of comparable intensity, with their ratio remaining relatively constant across different shell thicknesses. Conversely, in the mean-field dipolar regime, the helicity α-effect is dominant, exceeding the cross-helicity γ-effect by approximately two orders of magnitude, and its strength increases as the shell thickness decreases. The second study focuses on the importance of global magnetic helicity in self-consistent spherical dynamos. Magnetic helicity serves as a fundamental constraint in both ideal and resistive magnetohydrodynamics, offering crucial insights into the internal dynamics of dynamo processes that generate global magnetic fields on celestial bodies like the Sun and stars. This study investigates the behavior of global relative magnetic helicity through three self-consistent spherical dynamo solutions of increasing complexity. Magnetic helicity describes the global linkage between poloidal and toroidal magnetic fields weighted by magnetic flux. Our findings reveal distinct preferred states of this linkage, suggesting that global magnetic field reversals may act to preserve this preferred state. Specifically, when either the poloidal or toroidal field alone undergoes reversal, the preferred linkage state is disrupted. We demonstrate that magnetic helicity serves as a predictive

indicator for the onset of these reversals, potentially observable at the outer surface of celestial bodies. The third study investigates differential rotation in convecting spherical shells with non-uniform viscosity and entropy diffusivity. Current three-dimensional, physics-based simulations of the solar convection zone show significant discrepancies when compared to observations. These simulations present differential rotation patterns that are notably different from those inferred by solar helioseismology and display convective "Busse" columns that are absent in actual observations. To address this "convection conundrum," we employ a three-dimensional pseudospectral simulation code to explore the impact of radially non-uniform viscosity and entropy diffusivity on differential rotation and convective flow patterns in density-stratified, rotating spherical fluid shells. Our findings indicate that radial non-uniformity in fluid properties enhances polar convection, which creates significant lateral entropy gradients, leading to substantial deviations from differential rotation geostrophy due to thermal wind balance. We demonstrate simulations where this mechanism sustains differential rotation patterns closely resembling the true solar profile outside the tangent cylinder, although some discrepancies persist at high latitudes. This is particularly important as differential rotation is crucial for sustaining solar-like cyclic dipolar dynamos. This thesis uncovers new insights into how magnetic fields are created and sustained in rotating spherical fluid shells, revealing the intricate relationships between fluid dynamics, magnetic fields, and convective motions. These findings contribute to a deeper understanding of solar, stellar, and geomagnetic dynamo mechanisms, with implications for advancing research in both astrophysics and geophysics.

Contents

Abstract v

Acknowledgements xiii

Declaration xiv

1 Introduction 1

1.1 Topic of thesis . . . 1

1.2 Structure of thesis . . . 5

1.3 List of relevant publications . . . 6

2 Dynamo theory: from celestial bodies to computational models 7

2.1 Earths's interior and its magnetic field dynamics . . . 8

2.1.1 Secular variation and magnetic polarity reversal. . . . 10

2.2 Sun's interior and its magnetic field dynamics . . . 13

2.2.1 Maintenance of differential rotation . . . 16

2.3 Introduction to dynamo modelling . . . 22

2.3.1 Kinematic dynamo . . . 23

2.3.2 Mean-field dynamo . . . 24

2.3.3 MHD dynamo . . . 27

2.4 Geodynamo models . . . 29

2.4.1 Challenges in geodynamo modelling . . . 31

2.4.2 Recommendations for Future Research . . . 33

2.5 Recent solar dynamo models . . . 36

2.5.1 Challenges in solar dynamo modelling . . . 39

2.5.2 Recommendations for future research . . . 40
2.6 Concluding remarks . . . 42

3 A mathematical approach: self-consistent dynamos in rotating spherical fluid shells 43

3.1 Setting of the problem . . . 44
3.2 MHD dynamo equations . . . 45
3.2.1 Anelastic approximation . . . 46
3.2.2 Reduction to Boussinesq approximation . . . 57
3.3 Taylor's constraint and Taylor-Proudman theorem . . . 66

4 Discretization and numerical method 69

4.1 Pseudo-Spectral method . . . 71
4.1.1 Spectral decomposition . . . 72
4.1.2 Temporal discretization . . . 78
4.2 Implementation procedure . . . 82
4.2.1 Initialization . . . 82
4.2.2 Time Stepping Loop: . . . 84
4.3 Concluding remarks . . . 85

5 Effects of shell thickness on cross-helicity generation in convection-driven spherical dynamos 86

5.1 Introduction . . . 86
5.2 Mathematical model . . . 92
5.3 Onset of thermal convection: linear analysis . . . 95
5.4 Finite-amplitude convection and dynamo dynamics . . . 97
5.5 Shell thickness variation: bistability and general effects . . . 103
5.6 The cross-helicity effect . . . 106
5.7 Characteristics and significance of cross-helicity . . . 110
5.8 Concluding remarks . . . 112

6 A study of global magnetic helicity in self-consistent spherical dynamos 115

6.1 Introduction . . . 115

6.2 Mathematical model . . . 119

6.2.1 Magnetic helicity . . . 119

6.3 Verification test for helicity equation implementation . . . 120

6.4 Results: Dynamo solutions . . . 124

6.4.1 Case 1: Steady dynamo . . . 124

6.4.2 Case 2: Quasi-periodically reversing dynamo . . . 129

6.5 Case 3: Aperiodically-reversing dynamo . . . 133

6.6 Concluding remarks . . . 138

7 Differential rotation in convecting spherical shells with non-uniform viscosity and entropy diffusivity 140

7.1 Introduction . . . 140

7.2 Mathematical model . . . 145

7.3 Results . . . 146

7.4 Discussion including further results . . . 155

7.4.1 Flow structure and thermal wind balance analysis . . . 155

7.4.2 Secondary aspects to consider . . . 158

7.5 Concluding remarks . . . 163

8 Conclusion 166

8.1 Summary of findings . . . 167

8.1.1 Effects of shell thickness on cross-helicity generation in convection-driven spherical dynamos (Chapter 5) . . . 167

8.1.2 A study of global magnetic helicity in self-consistent spherical dynamos (Chapter 6) . . . 170

8.1.3 Differential rotation in convecting spherical shells with non-uniform viscosity and entropy diffusivity (Chapter 7) . . . 172

8.2 Closing remarks . . . 174

List of Tables

6.1 The three dynamo solutions considered in the study. 124

6.2 The helicity and magnetic field reversal times for the other observed reversals. . . . 135

7.1 Model parameters and energy densities for six selected dynamo solutions. 149

List of Figures

2.1 Angular velocity distribution within the solar interior inferred from helioseismology. 12

2.2 Sunspot area as a function of latitude and time. 14

2.3 Solar Interior Rotation and Dynamics. 20

3.1 Geometrical Configuration of the Problem. 44

5.1 Illustration of shell thickness aspect ratio variation. 89

5.2 Power spectra of velocity and magnetic field. 92

5.3 Critical parameters and Rayleigh number variations. 95

5.4 Dynamo solutions with varying η. 98

5.5 Chaotic dynamo attractors at $\eta = 0.5$. 99

5.6 Dynamo solutions at $\eta = 0.5$. 101

5.7 Bistability with respect to η. 103

5.8 Phase portrait of dynamo energy densities 104

5.9 Effects of α, β, and γ with η. 109

5.10 Spatial structures of electromotive force components 110

6.1 Dynamo solution visualization. 121

6.2 Velocity field visualization for Case 1. 125

6.3 Magnetic field visualization for Case 1 125

6.4 Toroidal and poloidal field linkage representation 126

6.5 Velocity field structures for Case 2. 128

6.6 Magnetic helicity time series for Case 2. 128

6.7 Time series related to reversals. 130

6.8 Latitude vs time plot of surface magnetic helicity density for Case 2. 132

6.9 Velocity field structures in Case 3. 133
6.10 Time series during reversals for case 3. 133
6.11 Latitude vs time plot of surface magnetic helicity density for Case 3 137

7.1 Radial profiles of model parameters 148
7.2 Observed profile of solar differential rotation 151
7.3 Differential rotation of dynamo solutions 152
7.4 Flow structures of cases from figure 7.3 154
7.5 Azimuthally and time-averaged entropy. 155
7.6 Differential rotation vs. Rayleigh number and solar/antisolar transition. 158
7.7 Time series of energy densities for self-sustained dynamo case 160
7.8 Comparison of dynamo solution (E) and non-magnetic convection solution (E′) . . 161
7.9 Magnetic field components of dynamo solution (E) 162

Acknowledgements

I deeply appreciate all those who have contributed to this thesis. I am particularly thankful to the Institute for Computational Cosmology at Durham University, the Edinburgh Parallel Computing Centre, and the University of Edinburgh for providing access to their DiRAC systems. The computational simulations for the research outlined in this thesis, which include investigations into the generation of cross-helicity in convection-driven spherical dynamos, the distribution of global magnetic helicity in self-consistent spherical dynamos, and the dynamics of differential rotation in convection-driven spherical shells with varying viscosity and entropy diffusivity, were executed using the DiRAC Data Centric system and the DiRAC Extreme Scaling service. This project received support from a variety of grants, such as the BIS National E-infrastructure capital grant ST/K00042X/1, STFC capital grants ST/H008519/1 and ST/K00087X/1, STFC DiRAC Operations grant ST/K003267/1, BEIS capital funding through STFC capital grant ST/R00238X/1, and STFC DiRAC Operations grant ST/R001006/1. I also want to express my gratitude to the School of Mathematics and Statistics at the University of Glasgow for their support in providing PhD sponsorship. I am truly grateful to all those who have supported and guided me throughout this process. Their assistance and motivation were essential in the completion of this thesis.

Declaration

I declare that, except where explicit reference is made to the contribution of others, that this dissertation is the result of my own work and has not been submitted for any other degree at the University of Glasgow or any other institution

_____

Parag Gupta

Chapter 1

Introduction

1.1 Topic of thesis

The dynamics of convection-driven dynamos in rotating spherical shells are a captivating area of study in both geophysical and astrophysical contexts. These dynamos play a pivotal role in generating and sustaining the large-scale magnetic fields observed in various celestial bodies. Deciphering the complex interactions between convection, rotation, and magnetic fields is crucial for explaining a range of natural phenomena. For instance, Earth's geomagnetic field acts as a shield against solar radiation, while the solar magnetic field significantly impacts planetary atmospheres. Furthermore, research in this area is vital for forecasting and mitigating geomagnetic storms, which can disrupt satellite communications and power grids, thus protecting essential technological infrastructure. Dynamos also offer valuable insights into solar cycles, which affect Earth's climate and pose challenges to space missions and satellite operations. Investigations into phenomena such as Earth's magnetic field polarity reversals enhance our comprehension of these intricate systems and their implications for both terrestrial and extraterrestrial environments. Additionally, studying differential rotation in the Sun enriches our understanding of solar dynamics, which is essential for grasping variations in solar activity and their effects on space weather and Earth's climate.

To further our knowledge in this domain, my research centers on convection-driven dynamos in rotating spherical shells, utilizing comprehensive analysis and simulation of spherical dynamo models. This work, which has been published, encompasses three key studies that make contributions to the field:

- **Effects of shell thickness on cross-helicity generation in convection-driven spherical dynamos.** The primary objective of this research, detailed in the paper [189], is to investigate the relative importance of helicity and cross-helicity effects as influenced by the thickness of the convective shell in models of self-consistent dynamos driven by thermal convection in rotating spherical shells—a field that has not been extensively studied before.

  Intuitive reasoning indicates that the helicity α-effect plays a pivotal role in the geodynamo, whereas the cross-helicity effect is more significant in the context of the global solar dynamo. The geodynamo operates within Earth's thick outer fluid core, where vigorous convection facilitates the development of large-scale columnar structures. These coherent structures are characterized by substantial vorticity, which generates strong helicity α-effect, quantifying the degree of linkage between the fluid's velocity and vorticity. This helicity is crucial for the generation of large-scale magnetic fields in the geodynamo. In contrast, the global solar dynamo functions within a thinner convection zone, where maintaining organized columnar structures is more challenging. Consequently, this leads to a less coherent vorticity profile increasing the relative significance of the cross-helicity effect. This effect, which measures the correlation between velocity and magnetic fields, becomes essential for understanding the dynamics of solar magnetic field generation, emphasizing the complex interplay between turbulence, helicity, and magnetism in solar phenomena.

  Moreover, the geodynamo and solar global dynamo differ markedly: the former displays a dominant, rarely reversing dipole, while the latter exhibits a regular periodic cycle. To comprehensively capture these distinctions, our study was conducted using parameter values known to support two coexisting dynamo branches. These branches exhibit different

magnetic field properties—one non-reversing and the other cyclic—and show significant disparities in zonal flow intensity and profile. This variability suggests that each branch likely engages distinct mechanisms for helicity and cross-helicity generation, a central focus of our investigation.

Furthermore, our research explores bistability as a potential factor influencing aperiodic magnetic field polarity reversals in the geodynamo and contributing to the regular cycle observed in the solar dynamo. Building upon previous investigations that explored hysteretic transitions across varying Rayleigh, Prandtl, and Coriolis numbers, this research presents novel findings demonstrating that these distinct dynamo branches persist even as the shell thickness η varies. More information on this study and its results can be found in Chapter 5 of this thesis.

- **A study of global magnetic helicity in self-consistent spherical dynamos.** The primary objective of this research, detailed in the paper [91], is to explore global magnetic helicity in self-consistent convection-driven dynamos within spherical shells, a topic that has received limited attention. Magnetic helicity is an invariant of ideal magnetohydrodynamics (MHD) that describes field line topology weighted by magnetic flux and remains approximately conserved in weakly resistive conditions. This makes it crucial for both laboratory and astrophysical plasmas. While magnetic helicity has been extensively studied in mean field dynamo models, its role in self-consistent convection-driven dynamos in spherical shells is less understood. This study aims to fill this gap by analyzing typical solutions to a well-studied model for spherical dynamos, which are representative of various known dynamo regimes. The three solutions considered in this work increase in complexity, allowing the assessment of magnetic helicity as a tool for prediction and analysis in increasingly chaotic spatial and temporal flow and field structures.

  The relevance of this study is further supported by recent observational studies on the Sun, which show that helicity flux during solar minima is a good predictor of subsequent solar maxima, and measurements of magnetic helicity in other stars have identified scaling laws relating the surface helicity density to the toroidal field strength. These findings suggest that magnetic helicity density could be used to characterize different stages of

stellar and dynamo evolution. This study's general approach does not aim to model any specific star or planet but rather to analyze typical dynamo solutions to understand how global magnetic helicity can inform our understanding of dynamo mechanisms and field topology, particularly in observable outer surface variations. More information on this study and its results can be found in Chapter 6 of this thesis.

- **Differential rotation in convecting spherical shells with non-uniform viscosity and entropy diffusivity.** The primary objective of this research, detailed in the paper [90], is to unravel the intricate dynamics of magnetic phenomena driven by thermal convection within the solar interior. High-resolution numerical simulations based on fundamental physical laws have proven indispensable in studying these processes and interpreting observational data in solar physics. However, despite these advancements, significant discrepancies persist between simulated and observed solar dynamics, particularly concerning differential rotation patterns and the presence of convective "Busse" columns. These discrepancies are part of the so-called "convective conundrum," which challenges our understanding of solar dynamics.

  Accurately capturing differential rotation is crucial as it directly influences magnetic field generation and the cyclic behavior observed in solar activity. This research aims to address these challenges by investigating how radially varying viscosity and entropy diffusivity impact convective flow patterns and differential rotation in rotating spherical fluid shells. Through detailed simulations and comparisons with observational data, we aim to provide insights that refine our understanding of solar dynamics and enhance the fidelity of dynamo models. More information on this study and its results can be found in Chapter 7 of this thesis.

Each of these studies offers detailed insights into the functioning of convection-driven dynamos within rotating spherical shells and their broader implications for celestial magnetism. Together, they contribute to a deeper understanding of the mechanisms driving magnetic field generation, amplification, magnetic reversals, and differential rotation in celestial bodies, thereby advancing our theoretical understanding in geophysics and astrophysical research.

1.2 Structure of thesis

The thesis follows a structured format beginning with an introductory Chapter 2, which sets the stage by providing essential background on dynamo theory, setting the context for the research topics in the thesis without providing a comprehensive overview. Following this, Chapters 3 and 4, rigorously formulate the mathematical problems under consideration and describe the numerical methods employed for their solution, respectively. Chapter 5, delves into the dynamics of magnetic field generation in rotating thermal convection within spherical fluid shells, drawing upon the findings from the paper titled "Effects of shell thickness on cross-helicity generation in convection-driven spherical dynamos". This chapter particularly emphasizes the relative significance of helicity and cross-helicity effects in the process of magnetic field generation. Chapter 6, based on the paper titled "A study of global magnetic helicity in self-consistent spherical dynamos", investigates the behavior of magnetic helicity in convection-driven dynamos within rotating spherical shells. This chapter provides insights into the role of magnetic helicity as a predictive indicator for the onset of magnetic reversals, which could potentially be observed at the outer surface of celestial bodies. Chapter 7, grounded in the paper titled "Differential rotation in convecting spherical shells with non-uniform viscosity and entropy diffusivity", aims to explore the effects of non-uniform viscosity and entropy diffusivity on the generation of differential rotation by convection in rotating spherical shells. This chapter sheds light on the influence of non-uniform parameters on differential rotation profiles, with implications for understanding solar and geodynamo dynamics. The concluding chapter 8 synthesizes the key findings from the preceding chapters and offers an outlook to future research objectives. It discusses the implications of the research outcomes, addresses remaining open questions, and suggests potential directions for further investigation.

1.3 List of relevant publications

- Effects of shell thickness on cross-helicity generation in convection-driven spherical dynamos [189] discussed in the chapter 5.
- A study of global magnetic helicity in self-consistent spherical dynamos [91] discussed in the chapter 6.
- Differential rotation in convecting spherical shells with non-uniform viscosity and entropy diffusivity [90] discussed in the chapter 7.

Chapter 2

Dynamo theory: from celestial bodies to computational models

The study of magnetic fields within celestial bodies has emerged as a central theme in geophysics and astrophysics, with dynamo theory providing a crucial framework. This theory sheds light on the complex mechanisms behind the generation and evolution of magnetic fields, revealing the intricate interplay between fluid motion, electromagnetic induction, and magnetic field amplification. By deciphering these processes, scientists gain invaluable insights into magnetic phenomena observed across various scales, from planetary cores to the vast expanses of the cosmos.

In this chapter, we provide essential background information necessary to understand the research discussed in Chapters 5, 6, and 7. Each of these chapters offers a detailed literature review on their respective topics. Specifically, this chapter covers the dynamics of Earth and the Sun, emphasizing the significance of the magnetic field. Key processes such as magnetic polarity reversal and differential rotation are explored. Additionally, introductory discussions on dynamo models including kinematic, mean field, and MHD dynamos are provided. We review recent advancements in geodynamo and solar dynamo simulations, taking into account observational constraints. Finally, we discuss potential future research directions in this field.

2.1 Earths's interior and its magnetic field dynamics

The Earth's magnetic field is generated in the outer core, a region approximately 2,890 kilometers beneath the Earth's surface. The outer core consists of molten iron and nickel that are fluid due to high temperatures generated by the Earth's internal heat and pressure. Convection currents in the Earth's outer core, driven by both thermal and compositional gradients [128], along with the planet's rotation, generate electric currents. These currents are responsible for sustaining the Earth's magnetic field through a process known as the geodynamo, which operates via electromagnetic induction. This process is central to the generation and maintenance of the Earth's magnetic field [120, 139].

By monitoring changes in the magnetic field over time, scientists can explore Earth's history. For instance, magnetic stripes on the ocean floor serve as evidence of seafloor spreading and the movement of tectonic plates. Beyond its scientific importance, Earth's geomagnetic field is vital for life and technology. It shields the planet from harmful solar radiation and cosmic rays, protecting our atmosphere and enabling life to thrive. Moreover, it plays a crucial role in various technological applications such as navigation systems, which rely on accurate magnetic field data.

The Earth's magnetic field is often approximated as a dipole, similar to a bar magnet with north and south poles. In a dipolar magnetic field, field lines emerge from the south pole, curve around the Earth, and re-enter at the north pole. While the Earth's magnetic field is predominantly dipolar, it is not perfectly so. Small deviations and complexities exist due to interactions with the solar wind and variations in the Earth's interior and crust. These deviations can lead to

localized variations in field strength and direction, impacting magnetic phenomena observed on and near the Earth's surface. The Earth's magnetic field serves as a unique case study due to its dynamic interaction with the planet's internal processes and external influences like the solar wind.

Continued research into the Earth's geomagnetic field is essential. It remains a complex and dynamic system with significant implications for both scientific understanding and practical applications in our modern world. Studying the Earth's geomagnetic field involves a multi-faceted approach combining observational data, laboratory experiments, theoretical models, and an understanding of solar and space physics. Here's a breakdown of how each of these methods contributes to our knowledge:

Observational data. Scientists gather data from various sources such as ground-based observatories, satellites, airborne surveys, marine surveys, and the International Space Station. These observations provide maps of the magnetic field's strength and direction across the Earth's surface and help monitor its changes over time. Magnetic anomalies, where the field deviates from expected norms, are also studied to infer geological features like mineral deposits.

Laboratory experiments. Experiments are conducted to simulate conditions similar to those in the Earth's core, where the geomagnetic field is generated. Researchers study how materials like molten iron conduct electricity and behave under high pressures. These experiments help in understanding the geodynamo process, which is crucial for generating and sustaining the Earth's magnetic field.

Theoretical models. Mathematical models are used to simulate and predict the behavior of the geomagnetic field. These models incorporate data from observational studies and laboratory experiments. By adjusting these models to fit observed data, scientists can infer the processes occurring deep within the Earth, where direct observation is not feasible.

Solar and space physics. The Earth's magnetic field interacts with the solar wind, a flow of charged particles from the Sun. Studying these interactions helps scientists understand the structure of the magnetic field and its variations. This field of study, known as magnetospheric physics, contributes to our understanding of how the Earth's magnetic field responds to external influences.

Geomagnetic storms and space weather. Changes in the solar wind can cause disturbances in the Earth's magnetosphere, leading to geomagnetic storms. These storms can impact power grids, satellite communications, and navigation systems. Scientists study these phenomena to understand their causes and effects, aiming to improve predictions of space weather events.

Each of these approaches plays a crucial role in advancing our understanding of the geomagnetic field. By integrating data from multiple sources and using theoretical models to interpret them, scientists can uncover the complexities of Earth's magnetic field and its interactions with the broader solar system environment. This interdisciplinary field continues to evolve with ongoing research efforts aimed at unraveling the remaining mysteries of the geomagnetic field.

2.1.1 Secular variation and magnetic polarity reversal.

The Earth's magnetic field is dynamic, undergoing both gradual changes in strength and direction over time as well as dramatic reversals in polarity [120].

Secular Variation refers to the gradual changes in the Earth's magnetic field over time, driven by evolving conditions and flow patterns within the Earth's outer core. These changes influence the alignment of the magnetic poles, causing them to drift and be offset from the geographic poles. The impacts of geomagnetic secular variation (GSV) are wide-ranging. In navigation, GSV affects magnetic declination, the angle between magnetic north and true north, which is crucial for accurate compass readings and navigation. In technological systems, GSV influences geophysical surveys, satellite systems, and other technologies that rely on precise magnetic field data. In Earth sciences, GSV provides valuable insights into the Earth's interior dynamics, including processes related to plate tectonics. Scientists study GSV through various methods. Historical records involve analyzing long-term magnetic compass observations. Modern observations rely on data collected from magnetic observatories and satellites. Paleomagnetic records are examined by studying magnetic signals preserved in rocks and archaeological materials.

On much longer time scales, the Earth's magnetic field can undergo magnetic polarity reversals, where the magnetic north and south poles swap places. These geomagnetic reversals occur irregularly, with inter-event durations (the time between reversals) ranging from hundreds of thousands to millions of years. The reversal transition itself typically takes between a few thousand to tens of thousands of years. External factors like solar activity, tectonic plate movements, and human activities can also influence the Earth's magnetic field, causing temporary disturbances such as geomagnetic storms.

Understanding both secular variation and magnetic polarity reversals is essential for predicting changes in the Earth's magnetic field, assessing their impacts on navigation, communication, and technology, and gaining insights into the planet's geological history and interior processes.

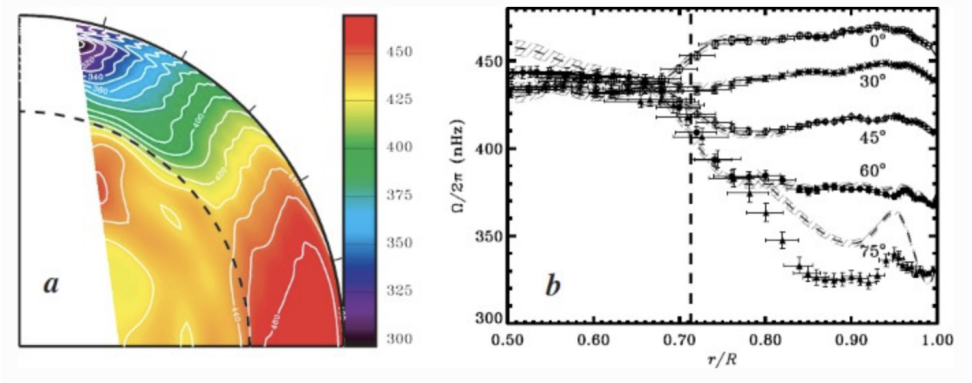

Figure 2.1: Angular velocity distribution within the solar interior inferred from helioseismology adapted from [212]. Panel (a) displays a 2D rotational inversion using the subtractive optimally localized averaging (SOLA) technique, illustrating the latitude-radius profile. In panel (b), the radial dependence of angular velocity is depicted for various latitudes, derived from both SOLA (marked symbols with 1 error bars) and regularized least squares (RLS; represented by dashed lines) inversion methods. The base of the convection zone is indicated by dashed lines. These inversions utilize data from the Michelson Doppler Imager (MDI) instrument aboard the SOHO spacecraft, averaged over a period of 144 days. It's important to note that inversions lose reliability near the rotation axis, denoted by white regions in panel (a). Additionally, global modes primarily capture the rotation component symmetric about the equator. This figure is taken from [141].

Thus, the Earth's magnetic field is a fascinating and ever-changing phenomenon that serves crucial roles: protecting our planet and aiding navigation. Scientists are deeply engaged in studying this intricate force, from its origins deep within the Earth to its expansive influence in space. This ongoing research not only enhances our ability to predict and manage geomagnetic storms but also enriches our comprehension of Earth and its complex systems. Despite significant progress, the study of the magnetic field poses enduring scientific puzzles that will captivate and motivate future generations of geophysicists. In the next section, we'll explore the dynamics of the sun and its magnetic field.

2.2 Sun's interior and its magnetic field dynamics

The Sun's dynamo, which generates its magnetic field, is a complex interplay of turbulent interactions in velocity and magnetic fields, significantly influenced by its rotation. Turbulence in the Sun's plasma, driven by nearly inviscid thermal convection from core fusion heat and rapid cooling at the photosphere, plays a crucial role. Despite its chaotic nature, this turbulence enables the Sun to maintain large-scale magnetic fields, differential rotation, and meridional circulation. Local turbulent vortices alone cannot sustain these structures due to their short coherency time; hence, correlations induced by rotation are essential.

For a long time, turbulent phenomena on the Sun's surface were well-known, but their role in its interior remained mysterious until helioseismology emerged. This field revealed two zones of strong rotational shear within the Sun. Global inversions of rotational profiles showed conical isorotational contours (Figure 2.1), contrasting with earlier cylindrical predictions by the Proudman-Taylor theorem or early global-scale simulations. Angular velocity decreases uniformly towards the poles by approximately 30% across the convective envelope, with mid-latitudes showing nearly radial contours. A significant shear zone occurs at the tachocline, the boundary between the convection zone and the radiative interior, initially proposed by Spiegel [202] and confirmed by Brown's helioseismic detection [20].

Another distinct layer near the top of the convection zone displays significant changes in rotation speed across different latitudes. Below the photosphere, rotation speed increases at low and mid-latitudes until approximately 95% of the Sun's radius, with a 3% change in rotation rate [52]. Deeper within the convection zone, rotation speed decreases, although higher latitude variations remain unclear and potentially opposite. Helioseismic studies indicate rotation speed decreases towards the poles [182], with unexpectedly slower rotation than smooth extrapolations predict, challenging angular momentum conservation.

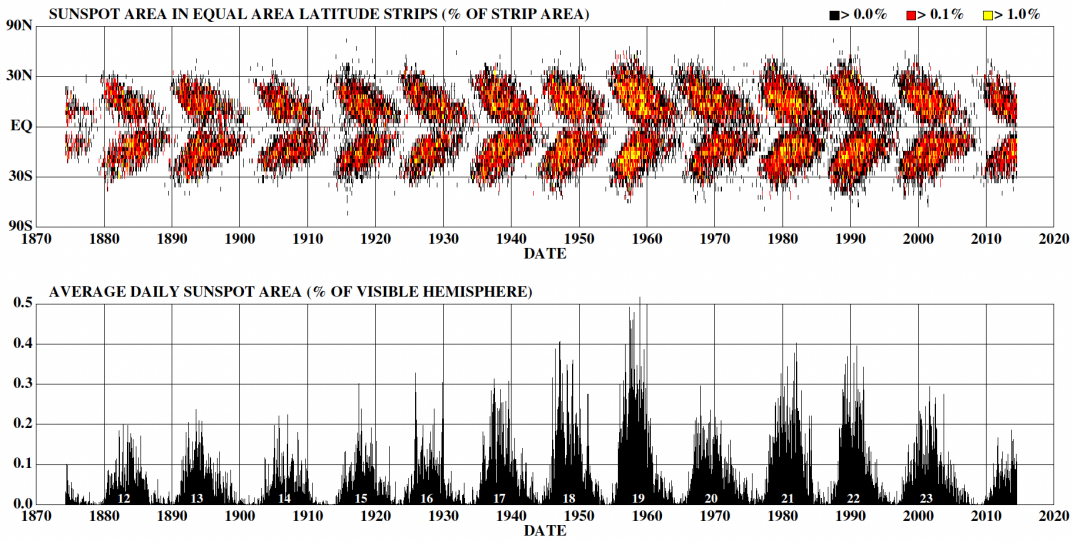

Figure 2.2: The figure shows the variation of sunspot area with latitude and time. The lower panel depicts the average daily sunspot area for each solar rotation since May 1874 as a function of time. In the upper panel, a color-coded scale illustrates the relative sunspot area within latitude strips of equal area. Sunspots emerge in two bands, one in each hemisphere, starting around 25° from the equator at the beginning of each solar cycle and migrating towards the equator as the cycle advances. This figure is taken from [95].

The Sun exhibits detailed rotational features such as torsional oscillations and zonal jets, where local prograde or retrograde flows occur. Studies hint at a prograde polar jet near the Sun's poles [182], though consensus is lacking. Global helioseismic inversions [92, 7, 236] depict symmetric rotation, while local studies reveal temporal changes. Meridional circulation, conveying heat and momentum from equator to poles and back, is influenced by anisotropic heat transport and the Sun's magnetic field [75, 222].

The Sun's dynamo, driven by turbulent motion, rotation, and magnetic fields, generates its large-scale magnetic fields, differential rotation, and meridional circulation. Observational patterns, such as the sunspot cycle and butterfly diagram, illustrate the latitude-dependent nature of magnetic activity. The sunspot cycle refers to an approximately 11-year cycle during which sunspots and other magnetic phenomena appear in specific latitude bands, migrating towards the equator.

As these bands converge at the equator, the overall magnetic field undergoes a polarity reversal, resulting in a 22-year cycle. The butterfly diagram graphically represents this migration, showing how sunspots start at higher latitudes and move toward the equator over the cycle (see Figure 2.2).

Sunspot groups typically exhibit areas of magnetic polarity that alternate between facing outward and inward, often tilting in an east-west orientation. According to Hale's laws, the leading polarity of these groups changes every 11 years, and their tilt increases with latitude, a phenomenon known as Joy's law. This behavior suggests that active regions consist of twisted magnetic loops emerging from below the Sun's surface while remaining anchored there [65]. These loops often exhibit specific twisting directions, characterized by magnetic or current helicity. Observations indicate that magnetic helicity is generally positive in the northern hemisphere and negative in the southern hemisphere, particularly in larger structures like coronal loops. For deeper insights, refer to studies by [65, 44, 184, 157].

Rotation induces anisotropic momentum and heat transport in the convective plasma, shaping global flows like differential rotation and meridional circulations. Differential rotation, where the equator spins faster than the poles, results from angular momentum transport. Meridional circulation transports heat and momentum, influenced by the Sun's rotation and magnetic fields. Understanding the dynamics and dynamo processes in the deep solar convection zone is crucial for comprehending solar and stellar magnetism, structure, evolution, and variability. This knowledge is essential for understanding how the Sun impacts life on Earth through various processes collectively known as space weather, linked to cyclic magnetic activity [184]. Next, we will explore the maintenance of differential rotation.

2.2.1 Maintenance of differential rotation

In this section, we delve into the maintenance of differential rotation in the Sun, closely following the insights and structure presented in [141].

The Sun's rotation is fundamental to its dynamics, and we learn much about it through helioseismology, the study of its internal vibrations. To understand this, we define the angular momentum per unit mass ($\mathscr{L}$), which indicates the rotational energy each part of the Sun possesses. It's calculated using the Sun's distance from its center (r), its constant rotation speed (Ω_0), and a factor called the moment arm (λ), defined as $\lambda = r\sin\theta$. The equation for angular momentum per unit mass ($\mathscr{L}$) can be expressed as:

$$\mathscr{L} = r\sin\theta(\Omega_0 r\sin\theta + \langle v_\phi \rangle) = \lambda^2\Omega_0, \tag{2.1}$$

where $\langle v_\phi \rangle$ represents the average azimuthal velocity at a given latitude, which can contribute to the total angular momentum, and This equation shows how the angular momentum depends on the Sun's rotation and structure. Next, we consider how this angular momentum changes over time, described by the following equation:

$$\bar{\rho}\frac{\partial \mathscr{L}}{\partial t} = -\nabla\cdot\left(\mathbf{F}^{\mathrm{MC}} + \mathbf{F}^{\mathrm{RS}} + \mathbf{F}^{\mathrm{MS}} + \mathbf{F}^{\mathrm{MT}} + \mathbf{F}^{\mathrm{VD}}\right). \tag{2.2}$$

Here, $\bar{\rho}$ represents the average density of the Sun, and the terms on the right-hand side represent different factors affecting the Sun's rotation, such as meridional circulation, Reynolds stress, Maxwell stress, mean magnetic fields, and viscous diffusion. Each of these factors contributes to how the Sun's rotation evolves over time.

The first term, $\mathbf{F}^{\mathrm{MC}} = \bar{\rho}\,\langle \mathbf{v}_{\mathrm{M}} \rangle\,\mathscr{L}$, deals with how angular momentum is transported by the mean meridional circulation. Here, $\langle \mathbf{v}_{\mathrm{M}} \rangle$ represents the mean meridional velocity, which is the average flow of material in the meridional (north-south) direction within the Sun. This term indicates how the movement of plasma in this direction contributes to the transport of angular momentum. The part involving the Sun's uniform rotation, $\bar{\rho}\,\langle \mathbf{v}_{\mathrm{M}} \rangle\,\lambda^2\Omega_0$, shows how the Coriolis force influences this circulation, redirecting it into rotational movements. Using the anelastic approximation (refer to chapter 3), we can understand this circulation further:

$$\boldsymbol{\nabla} \cdot \mathbf{F}^{\mathrm{MC}} = -\bar{\rho}\,\langle \mathbf{v}_{\mathrm{M}} \rangle \cdot \boldsymbol{\nabla}\mathscr{L}. \tag{2.3}$$

This explains how the circulation spreads out angular momentum, trying to keep it evenly distributed along its paths. The total amount of angular momentum transported through any closed surface must balance out, meaning any movement of angular momentum towards or away from the Sun's axis of rotation by the circulation must come from changes in how the Sun's rotation varies with latitude. Meridional circulation alone cannot create localized peaks or troughs in the angular momentum ($\mathscr{L}$) since the gradient of $\mathscr{L}$ (written as $\boldsymbol{\nabla}\mathscr{L}$) is zero at these points. Distinct features in the Sun's rotation pattern, like jets, must arise from other processes.

The primary force maintaining the Sun's rotation pattern is believed to be the Reynolds stress ($\mathbf{F}^{\mathrm{RS}}$). This term accounts for how non-uniform movements, especially from convection, redistribute angular momentum. Factors such as rotation, density differences, magnetic fields, and the Sun's spherical shape all contribute to uneven flow, leading to correlations between different velocity components. For instance, the correlation between horizontal velocities $\left\langle v'_\theta v'_\phi \right\rangle$, where v'_θ represents the latitudinal velocity fluctuation and v'_ϕ represents the azimuthal velocity fluctuation, causes angular momentum to move sideways. In contrast, the correlation involving radial velocity $\left\langle v'_r v'_\phi \right\rangle$, where v'_r indicates the radial velocity, results in vertical transport of angular momentum. This redistribution plays a crucial role in maintaining the Sun's rotation dynamics.

In the Sun's outer layers, turbulent convection dominates the Reynolds stress. However, in deeper regions like the tachocline and radiative interior, other movements may also contribute. When convective currents extend beyond their normal boundaries, they create internal wave patterns, particularly gravity waves, which travel through the Sun. While these waves can't move angular momentum without dissipation, dissipation caused by heat diffusion or wave breaking can lead to a net transport of angular momentum through the Reynolds stress. This transport tends to be long-range and difficult to predict accurately. Creating a reliable model for wave transport involves understanding how waves are created, move, and eventually dissipate, which is tough due to the wide range of sizes involved. Other factors like shear instabilities can also contribute to the Reynolds and Maxwell stresses.

Magnetism can influence the Sun's rotation by altering the Reynolds stress or directly moving angular momentum with the Lorentz force, which is the force exerted on a charged particle moving through a magnetic field. Let's break down the part of angular momentum moved by the Lorentz force into two components: one from wobbly (non-axisymmetric) magnetic fields, called the Maxwell stress $\mathbf{F}^{\mathrm{MS}}$, and another from steady (axisymmetric) magnetic fields, known as the mean-field $\mathbf{F}^{\mathrm{MT}}$.

The Maxwell stress involves some complicated math with terms like $\left\langle B'_\theta B'_\phi \right\rangle$ and $\left\langle B'_r B'_\phi \right\rangle$, which represent how magnetic fields interact in turbulent areas or with certain kinds of waves. Specifically, $\left\langle B'_\theta B'_\phi \right\rangle$ refers to the correlation between the azimuthal and polar components of the magnetic field, while $\left\langle B'_r B'_\phi \right\rangle$ represents the correlation between the radial and azimuthal components. These interactions are challenging to understand due to the inherent nonlinearity and turbulence of the magnetic fields involved. On the other hand, the mean-field contribution is simpler and can be written as:

$$-\nabla \cdot \mathbf{F}^{\mathrm{MT}} = \frac{1}{4\pi} \langle \mathbf{B}_{\mathrm{M}} \rangle \cdot \boldsymbol{\nabla} \left(\lambda \left\langle B_\phi \right\rangle \right). \tag{2.4}$$

This equation suggests that a steady poloidal magnetic field $\langle \mathbf{B}_{\mathrm{M}} \rangle$ resists changes in the Sun's rotation speed in the direction it points. It's like a rubber band that pulls back when you try to stretch it. This effect tends to make the Sun's rotation more uniform. The Maxwell stress can also have a similar effect due to its own version of magnetic tension.

While the viscous contribution ($\mathbf{F}^{\mathrm{VD}}$) doesn't significantly impact the Sun, it's important in models as it opposes changes in rotation speed, promoting uniform rotation.

Overall, the main players in determining the Sun's rotation are the Reynolds stress and meridional circulation, with the Lorentz force playing a smaller role. In a stable situation where rotation doesn't change much over time, we'd expect:

$$\boldsymbol{\nabla} \cdot \mathbf{F}^{\mathrm{RS}} = -\boldsymbol{\nabla} \cdot \mathbf{F}^{\mathrm{MC}}. \tag{2.5}$$

For years, scientists have believed that the Sun's outer layer, the solar envelope, maintains a delicate balance in its rotation ([207, 233], and references therein). This idea has been around since the late 1970s, but recent advances in helioseismology and computer simulations have shed new light on this balance.

Today, we have a good understanding of how specific angular momentum ($\mathscr{L}$) varies across the Sun's envelope, thanks to data from helioseismic inversions. This $\mathscr{L}$ profile is like a fingerprint of the Sun's rotation. By understanding meridional circulation near the Sun's surface, we can hypothesize how it might extend deeper into the Sun, allowing us to estimate the Reynolds stress despite limited direct observations. Equation 2.5 helps us understand how the Reynolds stress behaves in response to the Sun's rotation pattern determined by helioseismology. It tells us how the Reynolds stress must work to maintain the observed rotation pattern against the effects of the assumed meridional circulation. This relationship is illustrated in Figure 2.3. Although the Sun's rotation speed varies significantly from the equator to the poles, the specific angular

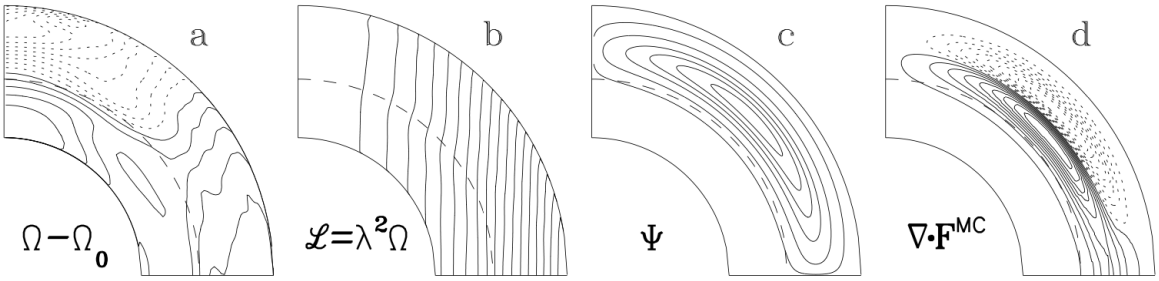

Figure 2.3: (a) The figure illustrates the angular velocity profile of the Sun based on helioseismic inversions. The solid and dotted lines indicate areas of prograde rotation (in the same direction as the Sun's overall spin) and retrograde rotation (in the opposite direction). (b) This profile provides insight into the specific angular momentum distribution within the Sun. (c) A hypothetical meridional circulation pattern is represented by the mass-flux streamfunction, with circulation in the northern hemisphere moving in a counter-clockwise direction. (d) The figure also depicts the divergence of the angular momentum flux $\mathbf{F}^{\mathrm{MC}}$ associated with this meridional circulation. Solid lines represent regions where the movement adds to the Sun's overall spin, while dotted lines denote regions where it subtracts from the spin. If Equation 2.5 were satisfied, this divergence would equal the convergence of angular momentum transport by the Reynolds stress, $\mathbf{F}^{\mathrm{RS}}$. This figure is adapted from [141].

momentum ($\mathscr{L}$) remains roughly the same, especially in the middle latitudes. This means that while rotation speed changes, the total rotational energy per unit mass stays consistent. If we imagine a hypothetical circulation pattern redistributing angular momentum across the Sun, the Reynolds stress would need to speed up the lower parts of the Sun's convection zone and equatorial regions while slowing down the upper convection zone to counteract the angular momentum redistribution caused by the assumed circulation. Any model aiming to replicate the Sun's rotation pattern and circulation must include a parameterization for Reynolds stress to account for this redistribution unless other forces, like the Lorentz force, are significant.

The findings displayed in Figure 2.3 can be applied to more complex circulation patterns as well. To maintain a balance in angular momentum transport caused by Reynolds stress, it needs to converge where circulation moves away from the rotation axis and diverge where it moves towards it. This is illustrated by expressing the flux divergence of meridional circulation as shown in Equation 2.3, noting its direction away from the rotation axis. Another approach is using helioseismic rotation profiles to figure out the meridional circulation needed for equilibrium based on a given model of Reynolds stress, as demonstrated by [60].

When solving the anelastic equations in a spherical shell with impenetrable, stress-free boundaries, assuming the magnetic field is radial at the boundaries, the system conserves the total angular momentum of the shell, symbolized by $\mathscr{J}$. However, this is just an approximation. In reality, interactions between the convective envelope and the radiative interior may affect the global angular momentum balance. Angular momentum exchange between the convection zone and the solar atmosphere is likely less significant on short timescales, although it's believed that the Sun has lost a substantial amount of its original angular momentum over its lifetime through phenomena like the solar wind.

Having gained a foundational understanding of solar and Earth dynamics and the significance of magnetic fields, our next focus will be on dynamo modelling. This section will cover various types such as kinematic mean field and magnetohydrodynamic (MHD) models. We will then explore geodynamo and solar dynamo models, considering observational constraints and future prospects in this field.

2.3 Introduction to dynamo modelling

The origins of Dynamo theory can be traced back to the field of geophysics, where scientists attempted to explain the Earth's magnetic pole migration, a phenomenon that had been observed for over four centuries through compass measurements and calibrations. The journey began with William Gilbert, who, in 1600, wrote the treatise "The Magnet and Magnetic Bodies, and on That Great Magnet the Earth." Gilbert was the first to attempt to describe Earth's magnetism, proposing that our planet was a permanent magnet. Carl Gauss later expanded on this idea, developing a more comprehensive theory of Earth's magnetism, introducing the idea of flowing currents. Gauss suggested that the magnetic field was likely due to galvanic currents within the Earth's volume, considering it as a potential field. Despite Gauss's theory, the origins of the magnetic field remained a hot topic of debate within the scientific community for almost a century [73].

In 1911, Arthur Schuster made a significant contribution. He presented a theory that included an idea that later became known as the dynamo theory. Interestingly, Schuster himself dismissed his theory as impossible. Yet, he and his contemporaries speculated that Earth's magnetic field was closely tied to its rotation, given the alignment of Earth's magnetic moment and its rotation axis [186]. According to this theory, Earth's rotation had a direct impact on atomic and electronic motions, resulting in polarization.

Various hypotheses emerged to explain geomagnetism, including the idea of independently rotating magnetized iron spheres within the Earth's interior. Some scientists even believed that the fundamental equations of electromagnetism required obscure relativistic modifications. However, many researchers challenged and dismissed these theories. Despite this, Joseph Larmor is widely recognized for laying the foundation for modern dynamo theory. Larmor [126] proposed an explanation for the strong magnetic fields in sunspots.

Meanwhile, Cowling [53] introduced his famous theorem stating that a dynamo cannot sustain an axisymmetric field. An axisymmetric field is one in which the vertical and horizontal components (B_r, B_θ, B_ϕ) do not depend on longitude. According to Cowling's theorem, such fields cannot be maintained by a dynamo. In simpler terms, if the magnetic field and fluid velocity are both axisymmetric (independent of longitude), then the zonal motion will shear the lines of force to create a component in the longitudinal direction. This process is known as the omega effect and generates a zonal field from the meridional component of the magnetic field. However, to create a successful dynamo, there needs to be a process that creates the meridional component from the zonal field, and this process cannot exist if the system is entirely axisymmetric.

Despite Cowling's theorem, researchers such as Elsasser [63] and Bullard [28] remained optimistic and continued to explore dynamo mechanisms in various contexts. Their perseverance led to refinements in dynamo theory, laying the groundwork for understanding magnetic field generation not only on Earth but also in astronomical contexts.

2.3.1 Kinematic dynamo

In response to the challenges posed by Cowling's theorem, researchers focused on kinematic dynamo models. These models explore the generation of magnetic fields by fluid motion without considering the magnetic field's feedback on the fluid motion itself. The goal was to define fluid motion and search for a self-sustaining magnetic field—one that does not decay or increase in amplitude over time for a given motion.

Early efforts, such as those by Bullard and Gellman [29] employed a spectral decomposition to investigate kinematic dynamo, but was unsuccessful in demonstrating dynamo action for their chosen fluid motion. Subsequent advancements by researchers like Herzenberg [98] and Backus [5] selected better velocity fields, proving the existence of homogeneous dynamos in principle, although the velocity fields they used were artificial.

Further progress came with studies by Roberts [175], Pekeris [163], and Kumar [123], who successfully constructed kinematic dynamos models using more realistic fluid motions. Notably, Roberts showed that Cowling's theorem does not forbid kinematic dynamos with axisymmetric fluid motions, which can sustain asymmetric magnetic fields. These advancements in understanding kinematic dynamos set the stage for further developments in dynamo theory.

2.3.2 Mean-field dynamo

In 1955, Parker [160] made an important contribution to the understanding of kinematic dynamos. He suggested that eddies in a rotating fluid experiencing turbulent convection may resemble atmospheric cyclones and anticyclones. These eddies could deform and potentially amplify the magnetic field in a conducting fluid. Building on Parker's ideas, Steenbeck [203] developed a mathematical framework for this concept and named it mean-field electrodynamics. This framework has since been extensively studied by notable scientists Moffatt [149] and Krause [122].

To grasp this concept, imagine a system with two scales where all variables split into large- scale and small-scale parts. To generate a large-scale magnetic field $\langle \mathbf{B} \rangle$, the small-scale motion $\mathbf{v}'$ and the small-scale magnetic field $\mathbf{b}'$ interact to create an electromotive force (emf) $\mathcal{E} = \mathbf{v}' \times \mathbf{b}'$ that has a large-scale component,

$$\langle \mathcal{E} \rangle \equiv \langle \mathbf{v}' \times \mathbf{b}' \rangle, \tag{2.6}$$

where an average of a quantity over small scales is denoted by angle brackets. Parker [160] and Steenbeck [203] suggested that if the statistical distribution of small-scale motions lacks mirror symmetry, the emf $\mathcal{E}$ does not disappear and can be expressed as

$$\langle \mathcal{E} \rangle = \alpha \langle \mathbf{B} \rangle, \tag{2.7}$$

where α is usually a tensor. This relationship has come to be known as the α effect, owing to the incidental use of the symbol in equation 2.7.

In mean-field dynamos, the large-scale magnetic field, $\langle \mathbf{B} \rangle$, is not only created by the mean emf, $\langle \mathbf{V} \rangle \times \langle \mathbf{B} \rangle$, but also by the effect of small-scale motions, $\mathcal{E}$. Cowling's theorem is no longer applicable in this case as the regenerative loop can be closed by the emf $\mathcal{E}$, particularly by $\alpha \langle B_\phi \rangle$, which produces a large-scale meridional field, $\langle \mathbf{B}_M \rangle$. This implies that axisymmetric large-scale fields, $\langle \mathbf{B} \rangle$ can potentially be self-sustained through a simple feedback loop: in the $\alpha\omega$ dynamo, the α creates $\langle \mathbf{B}_M \rangle$ from $\langle B_\phi \rangle$, and the ω effect produces $\langle B_\phi \rangle$from $\langle \mathbf{B}_M \rangle$. However, this is not the only possibility, α^2 dynamo also exists, where the α effect is influential in creating $\langle \mathbf{B}_M \rangle$from $\langle B_\phi \rangle$and producing $\langle B_\phi \rangle$from $\langle \mathbf{B}_M \rangle$, as allowed by the meridional components of equation 2.7. The type of mean-field dynamo depends on which effect, the ω-effect or the α-effect, is more potent in creating $\langle B_\phi \rangle$, and sometimes the term $\alpha^2\omega$ dynamo is used when both effects play a significant role.

It is important to emphasize that meanfield electrodynamics is primarily used in astrophysics, where the turbulent movements $\mathbf{v}'$ (representing small-scale turbulent velocities) are extremely vigorous, causing ε to be significant and even potentially dominating the mean emf $\langle \mathbf{V} \rangle \times \langle \mathbf{B} \rangle$ produced by the larger scales. The effects of small-scale flows in the Earth's core are primarily negligible. However, it is still possible to imagine a scenario in which a non-axisymmetric flow $\mathbf{V}'$ (representing large-scale flows) creates a non-axisymmetric field $\mathbf{B}'$ from the axisymmetric part $\overline{\mathbf{B}}$ of the large-scale field $\mathbf{B}$. In this case, the emf $\mathbf{V}' \times \mathbf{B}'$ has an axisymmetric component,

$$\overline{\varepsilon} \equiv \overline{\mathbf{V}' \times \mathbf{B}'}, \tag{2.8}$$

where the overbar denotes the average over longitude, ϕ. The ϕ component of $\overline{\varepsilon}$ that is crucial in overcoming Cowling's theorem is the one that generates $\overline{\mathbf{B}}_M$ from $\overline{B}_\phi$. Without $\overline{\varepsilon}_\phi$, $\overline{\mathbf{B}}$ cannot be maintained.

Reviews by Petrovay [164] and Charbonneau [45] have demonstrated that solar models based on mean-field theory are capable of reproducing numerous magnetic phenomena observed in the sun, including the distribution of sunspots over time and latitude. Until around 1995, the deeper layers of the solar convection zone, which were previously inaccessible to observations, could to some extent be evaluated for the solar angular velocity profile using mean-field theory [45]. Although the original assumptions made in the theory were in conflict with helioseismology, the coefficients of the α tensor were adjusted to align with some solar phenomena. Moreover, mean-field theory has also been effectively employed in modelling the terrestrial dynamo, with 3D direct numerical simulations yielding satisfactory results, as shown by Schrinner [185].

2.3.3 MHD dynamo

The late 1970s and early 1980s witnessed a revolutionary leap in computational power, enabling the first direct solutions to the magnetohydrodynamics (MHD) equations within spherical shells [77, 80, 76, 84]. Prior to these advancements, assumptions about the Sun's internal rotation profile were based on limited observations, leading to the belief that angular velocity remained constant in cylindrical surfaces and decreased with radius. Under these assumptions, dynamo wave propagation from a mean-field α dynamo was expected to be equatorward, influenced by the Coriolis force acting on convective eddies [160, 204, 230, 173]. However, this perspective definitively shifted with helioseismology's discovery that the angular velocity actually increases with radius in the majority of the solar convection zone [61, 183], leading to the "dynamo dilemma" [161]. Early 3D simulations mirrored this dilemma, successfully reproducing solar-like differential rotation with a fast equator and slow poles, yet exhibiting dynamo waves propagating toward the poles, contrary to solar behavior [76, 84].

Today, 3D numerical simulations remain the cornerstone for dynamo theorists, primarily due to the inherent nonlinearity of the problem. Despite advances in turbulence theory, analytical or semi-analytical solutions to the fully nonlinear compressible MHD system remain out of reach. Direct numerical simulations (DNS) aim to capture turbulent processes comprehensively, from the driving scale to relatively large scales, although representing the dissipation scale remains a challenge. While these simulations often fall short of the length scales crucial to astrophysical processes, they significantly illuminate the small-scale dynamics that influence larger-scale system transport properties. The aim of these simulations is usually to establish contact with theoretical predictions of turbulent spectra, such as the Kolmogorov scaling. However, similar to large-eddy simulations (LES) that parameterize small-scale physics, they face limitations in computational resources for obtaining increasingly higher resolutions and running large suites of simulations that accurately explore vast parameter space.

The early 2000s saw further advancements with the development of the ASH (Anelastic Spherical Harmonic) code [144, 62, 24]. Initial studies using this code focused on the Sun [23, 22, 143], but the 2010s brought a surge in diverse models using various codes. Notably, simulations of more rapidly rotating Suns began to regularly yield cycles and equatorward migration [74, 113, 19, 114, 153, 3, 131, 194]. This period also saw the emergence of simulations of main-sequence stars beyond the Sun, spanning a mass spectrum from fully convective M dwarfs to F stars with thin surface convection zones, and exploring core convection, dynamos, and interactions with fossil fields in more massive A, B, and O stars [68, 4]. Additionally, models investigating stellar magnetism beyond the main sequence emerged, including those for pre-main sequence stars, red giants, and newly formed neutron stars [64, 57, 27, 170, 134].

Alongside these simulation advancements, there has been a remarkable expansion in observational data and understanding of stellar magnetism. Long-term observing campaigns have identified cycles in dozens of stars through monitoring chromospheric emission [6]. However, the specifics of these cycles in relation to stellar rotation remain debated [17, 14, 156, 12]. Zeeman-Doppler imaging has revealed polarity reversals and large-scale non-axisymmetric magnetic fields in rapidly rotating late-type stars [119, 13, 118]. Moreover, magnetic activity reaches saturation when the stellar Rossby number falls below about 0.1, resulting in relatively constant activity and magnetic field strength for lower Rossby values [223, 171]. These fundamental observations serve as critical constraints for numerical simulations.

Despite its proximity and the insights provided by helioseismology, the Sun presents the most stringent challenges to simulations. Current 3D simulations struggle not only to replicate the solar dynamo but also the convective amplitudes and differential rotation, often yielding anti-solar solutions despite aiming for solar-like conditions [138, 112, 102, 26]. This "convective

conundrum" is a significant challenge in the field of stellar dynamo simulations today [154]. Furthermore, there are suggestions that the Sun may be approaching a transition point where its dynamo efficiency diminishes, possibly due to a shift from solar-like to anti-solar differential rotation, complicating its replication in simulations [178, 112, 25].

In the next section, we will explore geodynamo models, the challenges in interpreting numerical simulation outcomes, and future directions in this research area.

2.4 Geodynamo models

The study of Earth's geodynamo, the mechanism responsible for generating and sustaining the planet's magnetic field, has undergone significant evolution since its early numerical modelling efforts. The foundational work of Kageyama [110] and Glatzmaier [82, 83] marked pivotal milestones in this field. These pioneering studies were among the first to employ fully three-dimensional, nonlinear simulations to explore dynamo processes within Earth's outer core.

Kageyama's research focused on elucidating the fundamental processes underlying magnetic field generation. His simulations provided valuable insights into the dynamics of magnetic field evolution in a planetary context. Meanwhile, Glatzmaier's contributions were instrumental in replicating features of Earth's magnetic field, including its slow secular variations and periodic polarity reversals. These early models were groundbreaking, successfully capturing aspects of Earth's magnetic behavior and establishing a new direction for dynamo research.

The advancements in geodynamo modelling have been substantially driven by increasing computational power, which has enabled researchers to explore more realistic parameter regimes and incorporate complex physical effects. One significant development has been the integration of new factors such as heat flux patterns imposed by Earth's mantle. This incorporation has refined simulations, allowing for more accurate representations of core dynamics and thermal interactions [174, 49].

Despite these advancements, a critical aspect of modern geodynamo simulations is the challenge of operating within the correct regime. This term refers to achieving the appropriate force balance in the Navier-Stokes equations where Coriolis forces, pressure gradients, buoyancy, and Lorentz forces dominate, while viscous and inertial forces are relatively minor. Recent simulations have achieved extremely low Ekman numbers ($E = 10^{-8}$), pushing the boundaries of what can be simulated. However, the large Ekman numbers in some simulations necessitate counteracting effects such as stronger convective driving, which can introduce excessively large inertial effects. This underscores the ongoing need to verify whether these simulations accurately represent the correct force balance and can be reliably extrapolated to realistic planetary conditions.

In parallel with these numerical advancements, there has been a notable shift towards increased collaboration between researchers focused on dynamo theory and those specializing in geomagnetic observations. Historically, these groups worked in relative isolation, but recent years have seen a surge in interdisciplinary efforts. Publications by experts from both fields, such as those by [88, 214, 86, 51, 2], reflect this collaborative approach. These works emphasize the theoretical and numerical progress in dynamo models, revealing features that align with Earth's current and historical magnetic field configurations, including dominant axial dipolar components, minor nondipolar structures, and occasional polarity reversals.

Another significant development is the application of data assimilation techniques to geodynamo research [43]. By integrating dynamo simulations with geomagnetic observations, researchers hope to enhance the accuracy of simulations, improve the interpretation of geomagnetic data, and even predict future changes in Earth's magnetic field. This approach mirrors the successful application of data assimilation in weather forecasting and represents a promising direction for future research.

Several review articles have covered the theoretical and modelling aspects of the geodynamo and other planetary dynamos, including works by [107, 220, 120]. These reviews provide comprehensive insights into the current state of knowledge and ongoing research challenges in the field.

In the next section, we will discuss the challenges in geodynamo modelling, focusing on issues such as scaling simulations to realistic conditions and addressing the discrepancies between model predictions and observational data.

2.4.1 Challenges in geodynamo modelling

Despite significant progress, several challenges persist in accurately modelling geodynamo processes:

Scaling and parameter differences. One of the primary challenges in dynamo modelling is scaling numerical models to reflect Earth's actual core conditions. Numerical simulations often employ non-dimensional formulations to simplify computations and manage a broad range of parameters. However, this approach introduces significant discrepancies when compared to geophysical values. The Ekman number (E), which measures the ratio of viscous forces to Cori-

olis forces, is a critical parameter in dynamo models. For Earth's core, the Ekman number is estimated around 10^{-15} [169, 54]. Achieving such low values in simulations is currently infeasible due to computational constraints, which means that simulations often use higher values, around $10^{-4} - 10^{-6}$. This results in exaggerated viscous effects and impacts the accuracy of flow dynamics in the simulations [82, 83]. The magnetic Prandtl number P_m, representing the ratio of magnetic diffusion to viscous diffusion, is another critical parameter. Earth's core is thought to have a magnetic Prandtl number around 10^{-6} [169, 15]. Simulations often use P_m values greater than unity to sustain dynamo activity, which influences the scale and characteristics of the magnetic field modeled, especially near the core-mantle boundary [180, 116]. The discrepancy between model parameters and real-world values affects the fidelity of simulations in replicating Earth's magnetic field behavior.

Timescale challenges. Timescale considerations are crucial for accurate dynamo modelling. Numerical simulations typically express results in terms of "magnetic years," which are derived from the dipole decay time or magnetic diffusion timescale [86, 109]. However, accurately matching these timescales with observational data is challenging due to the following issues: the ratio of characteristic timescales in simulations must be carefully managed. Discrepancies in these ratios can lead to differences in observed magnetic field behaviors, such as the frequency of geomagnetic reversals or the duration of magnetic excursions [117]. Ensuring that simulated timescales align with those observed in Earth's magnetic geological history remains a significant challenge.

Observational constraints and model discrepancies. Comparing numerical models with observational data presents numerous difficulties due to constraints in data availability and resolution:

Reversal frequency and dipole moments. Simulated models that replicate geomagnetic reversals or fluctuations in dipole moments often exhibit discrepancies when compared to observational data. Some models show high-frequency oscillations or inaccurate dipole moment values compared to Earth's observations [86, 179]. This misalignment underscores the need for continuous refinement of models to accurately reflect the observed geomagnetic behaviors.

Impulses and excursions. Numerical models have yet to fully replicate observed geomagnetic impulses or jerks. Recent models have provided insights into these phenomena, but discrepancies persist in terms of reversal frequencies and dipole moment fluctuations [109, 86]. Achieving a model that consistently aligns with observed data remains an ongoing challenge.

Discrepancies in energy spectrum and model coefficients. The energy spectrum of the magnetic field in numerical models often shows significant discrepancies compared to the actual geomagnetic field. Some models exhibit energy levels that exceed those of the observed geomagnetic field, while others are closer to actual observations. These discrepancies in the energy spectrum and model coefficients can affect the overall accuracy of simulations [70].

In the next section, we will explore recommendations for future research to address the ongoing challenges and advance our understanding of geodynamo processes

2.4.2 Recommendations for Future Research

To provide a clear direction for future research and work in this field, the following steps and recommendations can be considered based on the review by Wicht and Sanchez [220]:

- **Resolve high thermal conductivity values.** Conduct comprehensive laboratory experiments to verify or refute the high thermal conductivity values indicated by ab initio simulations. Explore alternative theoretical models to address the challenges posed by these high thermal conductivity values, potentially leading to new understandings of the geodynamo process.
- **Enhance numerical simulations.** Develop more advanced numerical simulations with lower Ekman numbers. The most advanced simulations currently run at $E = 10^{-7}$, or even $E = 10^{-8}$ when employing hyperdiffusion techniques. Hyperdiffusion refers to the use of enhanced diffusion mechanisms that selectively smooth out small-scale turbulent features without excessively damping larger-scale dynamics, allowing simulations to achieve lower Ekman numbers while maintaining accuracy.
- **Investigate newly observed phenomena.** Perform in-depth studies on recently observed phenomena such as fast quasi-geostrophic Alfvén waves and spontaneous large gyres. Assess their relevance to the primary dynamo mechanism and geomagnetic field dynamics.
- **Facilitate comparisons with observational data.** Ensure future models include features that facilitate effective comparisons with observational constraints. Enhanced validation against observational data, refined model parameters, and extended integration times are critical for improving the accuracy and predictive power of geodynamo simulations.
- **Leverage practical applications.** Integrate numerical dynamo simulations into data assimilation frameworks. This can provide valuable insights into geomagnetic field dynamics and improve predictions of future magnetic field evolution.
- **Expand research on wave dynamics.** Investigate various types of waves beyond torsional oscillations that may play a role in Earth's core dynamics. Refer to foundational and recent studies to understand their impact on the overall behavior of the geodynamo.

- **Address thermal and compositional convection properties.** Explore methods that account for the distinct properties of thermal and compositional convection in dynamo simulations. Implement advanced approaches like the diffusion-free particle-in-cell method to study the evolution of the compositional field more accurately. Investigate the potential formation of a stably stratified layer beneath the core-mantle boundary and its implications for seismic studies.
- **Study heat flux configurations.** Conduct research on how variations in heat flux configurations at the core-mantle boundary influence reversal frequency and morphology. This can provide insights into the dynamic interplay between mantle convection and core processes.
- **Focus on magnetic field polarity reversals.** Continue to study magnetic field polarity reversals, which remain a frontier of geomagnetic research. modelling and paleomagnetic observations should aim to unravel the intricate mechanisms governing these phenomena, enriching our understanding of Earth's magnetic history.
- **Promote interdisciplinary collaboration.** Foster collaborations between computational scientists, experimentalists, and theorists. Sharing data and methodologies across disciplines can accelerate progress and validate findings through multiple approaches.
- **Advances in computational and observational techniques.** Invest in improving computational capabilities and observational techniques. As these technologies advance, they will provide deeper insights into the processes driving remarkable geomagnetic events and contribute to the broader understanding of the geodynamic evolution of our planet.

By focusing on these recommendations, researchers can address the current challenges in geodynamo modelling and contribute to a deeper understanding of Earth's magnetic field dynamics.

2.5 Recent solar dynamo models

Observational constraints on solar dynamo models primarily stem from observations of the solar magnetic field in its various manifestations. These observations aid in simulating the induction of electric currents and, consequently, the observed solar magnetic fields. While some progress has been achieved in replicating certain features of solar magnetism, especially those exhibiting an axisymmetric signature, fully comprehending the solar dynamo remains a daunting task. A crucial constraint arises from the "butterfly diagram," depicting the migration of sunspots over time and latitude. This migration pattern implies the existence of an underlying toroidal field in the Sun, likely situated near the bottom of the convection zone. Polarity laws and the reversal of polar fields during the sunspot cycle offer additional constraints. Recent investigations have also unveiled the prevalent "chirality" or twist of the solar magnetic field, differing between the northern and southern hemispheres [237]. However, while these observations provide valuable insights, they alone cannot offer a comprehensive understanding of the entire dynamo mechanism.

Advancements in computational heliophysics have significantly enhanced our understanding of the Sun's magnetic field and the dynamo mechanisms responsible for its generation. These mechanisms involve intricate physical processes such as differential rotation, meridional circulation, and magnetic field generation through dynamo action. High-resolution simulations, particularly those incorporating subgrid-scale turbulence models like Large-Eddy Simulation (LES) methods, have shown promise in elucidating global solar dynamics and dynamo mechanisms [74, 145, 194, 72, 25, 69, 200]. Despite significant progress, current 3D magnetohydrodynamic (MHD) simulations still face challenges in accurately reproducing helioseismic observations and surface phenomena due to the immense range of scales involved in solar dynamics, which surpass the capabilities of existing computational resources.

The Sun's rotation rates play a crucial role in shaping its differential rotation, with faster rotation rates leading to a fast equator and slower rates leading to a fast pole [72]. This phenomenon is governed by the Rossby number (Ro), defined as $Ro = \frac{U}{\Omega L}$, where U is the characteristic convection velocity, Ω is the angular rotation rate of the system, and L is the typical spatial scale of convection [147, 70]. Numerical methods have been employed to simulate solar-like differential rotation, each aimed at reducing the Rossby number, a key parameter in characterizing the solar angular velocity and convection velocity relationship. These methods include adjusting the rotation rate, modifying the luminosity, and manipulating viscosity and thermal conductivity. A low Rossby number signifies rotationally constrained convection, essential for accurately modelling a fast equator. While earlier low-resolution calculations successfully replicated solar-like differential rotation by focusing solely on large-scale convection, higher-resolution calculations have faced challenges in reproducing this phenomenon. The introduction of small-scale turbulence and a decrease in the effective convection scale (L) in high-resolution calculations have posed hurdles, particularly in replicating the fast equator [99]. This discrepancy becomes significant as the actual Sun exhibits much smaller turbulence levels extending down to the centimeter scale, highlighting the need for further refinement in modelling approaches.

Flux transport dynamos utilize real data on solar surface movements to predict aspects like cycle duration and magnetic field shapes [56]. Despite their success, challenges remain in creating models that fully capture solar complexity. A significant obstacle is accurately modeling the tachocline, a critical solar layer. The subadiabatic nature of the tachocline—where the temperature gradient is shallower than the adiabatic gradient—poses difficulties for numerical simulations. This is because the subtle balance between thermal stratification and rotational forces must be captured with high precision to reflect the region's dynamics. Small inaccuracies can lead to incorrect representations of energy transport and angular momentum, ultimately oversimplifying the tachocline's behavior. Additionally, generating correct radial angular velocity gradients, especially at the convection zone's base, further complicates efforts to achieve a comprehensive solution to the 3D global solar dynamo puzzle.

Recent advances with hybrid dynamos, which blend axisymmetric models with new insights, have shown promise. These hybrids leverage expectations surrounding the dominant symmetry of magnetic field patterns around the equator, largely influenced by global processes within the tachocline. Furthermore, recent studies revealing temporal variations in the longitudinal wave number of subsurface magnetic fields offer crucial cues for refining predictive models, especially concerning solar activity patterns throughout different phases of the sunspot cycle. Delving deeper, global magnetohydrodynamics (MHD) within the solar tachocline emerges as a focal point, unveiling its profound impact on dynamo models. Instabilities in differential rotation and toroidal magnetic fields within the tachocline trigger significant disturbances, serving as pivotal sources for dynamo action. Moreover, the nonlinear behavior of these instabilities can induce radical alterations in toroidal field profiles, influencing the orientation and latitudinal spread of sunspot groups. Looking ahead, the evolution towards fully three-dimensional global MHD models for the tachocline is anticipated, although the subadiabatic stratification of the tachocline suggests that quasi-2D behavior will persist as a crucial component. The non-axisymmetric properties of the solar tachocline present observable consequences, necessitating the design of helioseismic techniques tailored to detect $m = 1$ structures and velocities at tachocline depths. Additionally, variations in density and thermodynamic signatures within the tachocline offer tantalizing avenues for exploration, potentially shedding further light on its enigmatic nature [78].

Therefore, to understand the Sun's rotation and circulation, scientists employ various techniques, including helioseismology. These methods elucidate how the Sun's surface rotates differently across latitudes and depths and reveal the consistent material flow toward the poles known as meridional circulation. Despite these advancements, uncertainties and variations persist, necessitating ongoing investigation. In terms of modelling the Sun's magnetic field, scientists utilize equations that consider factors such as solar rotation and material movement. These models, known as solar dynamos, have evolved over time to better comprehend the behavior of the Sun's magnetic field. While certain models, like flux transport dynamos, have shown suc-

cess in simulating aspects of the solar cycle, challenges remain in aligning theoretical predictions with real observations. Achieving a comprehensive solution to the solar dynamo problem necessitates high-resolution 3D calculations that account for interactions between different layers of the Sun. Although progress has been made, the complexity of incorporating all relevant physical processes poses ongoing challenges for solar dynamo modelling.

2.5.1 Challenges in solar dynamo modelling

Despite significant progress, several challenges persist in accurately modelling solar dynamo processes:

Convective conundrum. One of the main issues is the "convective conundrum," which involves the difficulty of accurately capturing the convective energy spectrum [154]. Observational estimates suggest a much slower spectrum than numerical simulations indicate [94, 148]. This discrepancy extends to modelling supergranulation, a prominent flow pattern on the solar surface, and its energy spectrum peak [96]. Realistic simulations emphasize the importance of suppressing large-scale convective motion to reproduce observed features accurately [127, 70]. In terms of differential rotation, replicating the observed fast equator remains a critical aspect of the convective conundrum . While observational evidence supports its existence, numerical simulations struggle to match the actual solar differential rotation, primarily due to fast convection flow resulting in a high Rossby number. Recent studies propose potential solutions to aspects of the convective conundrum, showing promising results [101].

Representation of the solar tachocline. Another critical challenge is the accurate representation of the solar tachocline, a thin shear layer between the radiative interior and the convective zone. The difficulty lies in capturing both its small vertical scale and the complex interaction between the rotational shear and the underlying radiative zone. The transition from the radiative interior to the turbulent convection zone introduces intricate dynamics that are hard to model accurately, especially when accounting for the flow of energy and angular momentum. Failures in properly simulating these features often lead to oversimplified models that inadequately capture the role of the tachocline in magnetic field generation and the solar dynamo process.

Flux transport dynamos. While flux transport dynamos have shown success, they often rely on unrealistically high thermal conductivity values to achieve solar-like differential rotation. This discrepancy highlights the limitations of current models and the need for further refinement in simulating the interaction between different layers of the Sun.

Temporal variations in solar rotation. Understanding the temporal variations in solar rotation, such as torsional oscillations, adds another layer of complexity to the modelling efforts.

2.5.2 Recommendations for future research

Future research in solar dynamo modelling must address the aforementioned challenges to achieve a more comprehensive understanding of the Sun's magnetic field generation and behavior.

Development of hybrid dynamo models. One promising direction is the development of hybrid dynamo models that blend aspects of axisymmetric models with new insights from three-dimensional simulations. These hybrids leverage expectations surrounding the dominant symmetry of magnetic field patterns around the equator, influenced by global processes within the tachocline.

Advancements in helioseismology. Advancements in helioseismology can also provide valuable constraints for dynamo models by offering detailed insights into the solar tachocline's structure, velocities, and magnetic fields. Improved helioseismic techniques designed to detect non-axisymmetric structures and velocities at tachocline depths could help refine models and enhance our understanding of the solar dynamo.

Integration of observational data with numerical models. Integrating observational data with numerical models remains crucial for refining model accuracy. This integration involves resolving discrepancies between observational data and model predictions and accounting for uncertainties in physical parameters and boundary conditions. High-resolution 3D magneto-hydrodynamic (MHD) simulations that consider interactions between different solar layers are essential for advancing our understanding of solar dynamo processes.

In conclusion, while significant strides have been made in solar dynamo modelling, ongoing efforts are necessary to address the remaining challenges and refine our understanding of the Sun's magnetic field generation. By leveraging advancements in observational techniques and computational resources, researchers can continue to improve dynamo models, ultimately enhancing our ability to predict solar activity and its impacts on space weather and terrestrial climate.

2.6 Concluding remarks

In conclusion, this chapter has provided essential background information necessary to understand the challenges addressed in this thesis. It has outlined the theoretical foundations, observational constraints, and recent advances in convection-driven dynamos within rotating spherical shells. While Chapter 1 briefly introduced these challenges, this chapter has expanded on them, paving the way for deeper investigations in the following chapters. Chapter 3 will focus on the mathematical formulation of the problems at hand, detailing the specific models and equations used to explore magnetic field generation dynamics. The comprehensive understanding gained from this chapter highlights the importance of the challenges addressed in this thesis. Subsequent chapters will build upon this groundwork to further explore and refine our understanding of convection-driven dynamos, ultimately contributing to advancements in both astrophysics and geophysics.

Chapter 3

A mathematical approach: self-consistent dynamos in rotating spherical fluid shells

Understanding the complexities of magnetic field generation in celestial bodies such as the Earth and Sun presents a significant challenge due to the diverse array of contributing factors. Despite this complexity, we can elucidate the fundamental physical principles governing the primary magnetic field's generation. This understanding is achieved by applying basic principles of mass, momentum, and energy conservation, alongside a simplified form of Maxwell's equations, to a confined region of conducting fluid. This chapter outlines the fundamental assumptions and equations that underpin the research in this thesis, focusing on the dynamic interactions within solar and geodynamo systems.

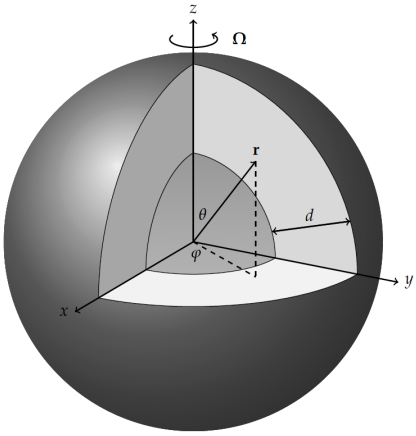

Figure 3.1: Geometrical configuration of the problem. A part of the outer spherical surface is removed to expose the interior of the shell to which the conducting fluid is confined. This figure is taken from [189].

3.1 Setting of the problem

To approximate the structure of planetary cores, we establish a spherical polar coordinate system (r, θ, φ) and consider an idealized setup shown in the Figure 3.1. It comprises two concentric spherical surfaces with centers at the coordinate system's origin and radii r_i and r_o, respectively. These surfaces form a spherical shell, defined alternatively by its thickness d and the ratio of inner to outer radii, η. The relationships between these parameters are given by:

$$\begin{aligned} d &= r_o - r_i, \quad \eta = \frac{r_i}{r_o}, \\ r_i &= \frac{\eta d}{1-\eta}, \quad r_o = \frac{d}{1-\eta}. \end{aligned} \tag{3.1}$$

The spherical shell rotates with a constant angular velocity $\mathbf{\Omega}$ about the z-axis. The region inside the shell ($r_i < r < r_o$) is filled with fluid, representing the planetary core and stellar convection zones, assumed to be a binary mixture of heavy and light elements. We assume the fluid obeys the continuum hypothesis and moves at non-relativistic velocities, meaning its speed is much slower than the speed of light. This assumption is made because it simplifies the governing equations of Magnetohydrodynamics (MHD), allowing us to ignore relativistic effects such as time dilation and Lorentz contraction, and to apply the classical form of Maxwell's equations,

which are sufficient for describing the interaction between the fluid and the magnetic field in planetary cores and stellar convection zones. Under these conditions, Magnetohydrodynamics (MHD) laws apply, supporting the possibility of a self-sustained magnetic field. The regions external to the shell ($r < r_i$ and $r > r_o$) are assumed impervious to fluid. They may be electrically insulating or the inner one may conduct while the outer remains insulating. In our simulations, both the inner and outer regions interact passively with magnetic field lines, playing no active role in magnetic field generation. While studies like Hollerbach and Jones [100] have shown that a conducting inner core can, under certain conditions, actively influence the dynamo process, such effects are not included in our model, where the inner core remains passive.

3.2 MHD dynamo equations

The equations governing magnetohydrodynamic (MHD) dynamos are derived from the conservation laws of fluid mechanics, Maxwell's equations, and Ohm's law of electromagnetism. Detailed explanations of the fundamental governing equations, methods of dimensionalisation, and scalar equations can be found in several comprehensive texts on fluid dynamics and MHD, such as those by [140].

In the field of geophysical and astrophysical fluid dynamics, particularly in studies involving MHD, two important types of approximations are often used: the anelastic approximation and the Boussinesq approximation. In the next section, we will focus specifically on these approximation models utilized in our research, discussing the assumptions made and the non-dimensional parameters involved. For an in-depth discussion, readers are encouraged to refer to [199], which provides a thorough exploration of these models.

3.2.1 Anelastic approximation

The anelastic approximation is particularly advantageous for numerical simulations of stellar and solar convection zones. This approximation simplifies the governing equations by filtering out sound waves, which allows for a more efficient computational focus on the slow-moving convective processes. This makes it highly suitable for studying large-scale fluid flows in astrophysical contexts [120, 125, 87, 194, 90, 181].

3.2.1.1 Hydrostatic polytropic reference state

In our system, the electrically conductive gas is confined within a spherical shell rotating about a vertical axis with a constant angular velocity ($\Omega\mathbf{k}$). An entropy difference (ΔS) is imposed between the inner and outer boundaries of the shell, and the gravitational field varies inversely with the square of the radial distance (r^{-2}). To describe the state variables within the shell, we define the average density , average temperature , and average pressure using the following relationships:

$$\bar{\rho} = \rho_c \zeta^n, \bar{T} = T_c \zeta, \bar{P} = P_c \zeta^{n+1}, \tag{3.2}$$

where $\zeta = c_0 + c_1 d/r$ denotes a radial profile defined by parameters $c_0 = (2\zeta_o - \eta - 1)/(1-\eta)$, $c_1 = (1+\eta)(1-\zeta_o)/(1-\eta)^2$, and $\zeta_o = (\eta+1)/(\eta \exp(N_\rho/n)+1)$. Here, ρ_c, P_c, and T_c represent reference values of density, pressure, and temperature, respectively, at the mid-shell. The gas polytropic index (n), the density scale height number (N_ρ), and the shell thickness ratio (η) are fundamental parameters characterizing this setup.

3.2.1.2 Mathematical formulation

The dynamics involving convection and magnetic field generation are described by a set of evolution equations governing continuity, momentum, energy, and magnetic flux. These equations are formulated based on the anelastic approximation by Lantz, Braginsky, and Roberts [105]. They are non-dimensionalized using the shell thickness ($d = r_o - r_i$) as a unit of length, d^2/ν_c as a unit of time, ΔS as a unit of entropy, $\nu_c\sqrt{\mu_0\rho_c}/d$ as a unit of magnetic induction, ρ_c as a unit of density, and T_c as a unit of temperature. Here, ν_c is the kinematic viscosity, μ_0 is the magnetic permeability, and λ is the magnetic diffusivity. The equations are structured as follows:

Continuity equation. The general form of the continuity equation, which describes the conservation of mass in a fluid, is given by:

$$\frac{\partial \rho}{\partial t} + \nabla \cdot (\rho \mathbf{u}) = 0, \tag{3.3}$$

where ρ is the fluid density, which may vary in space and time, and $\mathbf{u}$ is the fluid velocity vector, representing the velocity of the fluid at any point in space. Assuming a constant density $\bar{\rho}$ that does not change over time, we have:

$$\frac{\partial \bar{\rho}}{\partial t} = 0. \tag{3.4}$$

Substituting this into the continuity equation yields:

$$0 + \nabla \cdot (\bar{\rho} \mathbf{u}) = 0. \tag{3.5}$$

This leads us to the condition:

$$\nabla \cdot \bar{\rho} \mathbf{u} = 0. \tag{3.6}$$

This condition indicates that when the density is uniform over time, the divergence of the mass flux (density times velocity) is zero, implying that the mass flowing into a volume equals the mass flowing out, in accordance with the principle of conservation of mass.

Gauss's law for magnetism. Maxwell's equations encapsulate the fundamental principles governing electromagnetic fields. In scenarios where the electric field is negligible, one of Maxwell's equations simplifies to ensure the continuity of magnetic flux density (**B**):

$$\nabla \cdot \mathbf{B} = 0. \tag{3.7}$$

This equation asserts that the divergence of the magnetic field vector **B** is zero everywhere in space. Physically, this implies that magnetic monopoles do not exist, and the magnetic field lines form closed loops or do not diverge or converge within any region.

Momentum equation. The conservation of momentum in a rotating frame of reference is governed by the Navier-Stokes equation, expressed as:

$$\partial_t \mathbf{u} + (\nabla \times \mathbf{u}) \times \mathbf{u} = -\nabla \Pi - \tau(\hat{\mathbf{k}} \times \mathbf{u}) + \frac{\mathrm{R}}{P_r} \frac{S}{r^2} \hat{\mathbf{r}} + \frac{\rho_c}{\bar{\rho}} \nabla \cdot \hat{\boldsymbol{\sigma}} + \frac{1}{\bar{\rho}} (\nabla \times \mathbf{B}) \times \mathbf{B}. \tag{3.8}$$

This equation governs the momentum balance within the fluid in a rotating frame of reference. The momentum equation is derived from Newton's second law, which states that the rate of change of momentum of a fluid element is equal to the sum of the forces acting on it. In a rotating frame, this law must account for various forces acting on the fluid, including inertial, pressure, Coriolis, buoyancy, viscous, and magnetic forces.

The first term, $\partial_t \mathbf{u}$, represents the time derivative of the velocity field $\mathbf{u}$, capturing changes in velocity over time. The second term, $(\nabla \times \mathbf{u}) \times \mathbf{u}$, describes the nonlinear advective acceleration of the fluid, illustrating how the velocity field advects fluid parcels and enhances flow features. The third term, $-\nabla\Pi$, corresponds to the pressure gradient within the fluid, exerting forces that can accelerate or decelerate fluid motion in response to spatial variations in pressure. The fourth term, $-\tau(\hat{\mathbf{k}} \times \mathbf{u})$, represents the Coriolis force induced by the rotation of the reference frame, influencing the direction of fluid motion relative to the rotating system, where τ is the angular velocity of rotation and $\hat{\mathbf{k}}$ is the unit vector in the vertical direction. The fifth term, $\frac{\mathrm{R}}{P_r}\frac{S}{r^2}\hat{\mathbf{r}}$, denotes the buoyancy force arising from entropy gradients (S), which drives fluid movement due to temperature variations; here, R is a constant related to buoyancy, P_r is the Prandtl number, and r is the radial distance from the axis of rotation. The sixth term, $\frac{\rho_c}{\bar{\rho}}\nabla \cdot \hat{\boldsymbol{\sigma}}$, accounts for viscous stresses ($\hat{\boldsymbol{\sigma}}$) within the fluid, reflecting internal friction that dissipates kinetic energy into heat, where ρ_c is a characteristic density and $\bar{\rho}$ is the mean density of the fluid. The seventh term, $\frac{1}{\bar{\rho}}(\nabla \times \mathbf{B}) \times \mathbf{B}$, represents the Lorentz force resulting from interactions between magnetic field gradients and the magnetic field itself, thereby influencing fluid dynamics in magnetized environments.

In summary, these terms collectively reflect the balance between inertial forces, pressure gradients, Coriolis forces, buoyancy, viscous stresses, and magnetic forces in the fluid. The deviatoric stress tensor $\hat{\boldsymbol{\sigma}}$ is given by:

$$\sigma_{ij} = 2\nu\bar{\rho}\left(e_{ij} - \frac{e_{kk}}{3}\delta_{ij}\right), \quad e_{ij} = \frac{\partial_i u_j + \partial_j u_i}{2}, \tag{3.9}$$

where, ν is the kinematic viscosity, e_{ij} is the strain rate tensor, and δ_{ij} is the Kronecker delta. Thus, the momentum equation encapsulates the dynamics of fluid motion in a rotating frame, integrating various physical phenomena and providing a comprehensive understanding of fluid behavior in complex environments. The derivation reflects how each term contributes to the overall momentum balance within the fluid, emphasizing the significance of the defined parameters in characterizing the system's dynamics.

Entropy equation. The entropy equation is derived from the fundamental principles of conservation of mass and energy. It captures how changes in the entropy of a fluid are influenced by both advective transport and diffusive processes. The evolution of specific entropy S within a fluid is described by the entropy equation:

$$\partial_t S + \mathbf{u} \cdot \nabla S = \frac{1}{P_r \bar{\rho} \bar{T}} \nabla \cdot (\bar{\kappa} \bar{\rho} \bar{T} \nabla S) + \frac{c_1 P_r}{\mathrm{R} \bar{T}} \left(\hat{\boldsymbol{\sigma}} : \mathbf{e} + \frac{1}{P_m \bar{\rho}} (\nabla \times \mathbf{B})^2 \right). \tag{3.10}$$

Here, the double-dot symbol (**:**) denotes a component-wise inner product. In this equation, the term $\partial_t S + \mathbf{u} \cdot \nabla S$ represents the temporal change and advective transport of entropy by the fluid velocity $\mathbf{u}$. The third term, $\frac{1}{P_r \bar{\rho} \bar{T}} \nabla \cdot (\bar{\kappa} \bar{\rho} \bar{T} \nabla S)$, accounts for the diffusive flux of entropy, where $\bar{\kappa}$ is the thermal diffusivity, P_r is the Prandtl number, $\bar{\rho}$ is the density, and $\bar{T}$ is the temperature. This term quantifies how entropy diffuses due to temperature gradients in the fluid. The fourth term, $\frac{c_1 P_r}{\mathrm{R} \bar{T}} \left(\hat{\boldsymbol{\sigma}} : \mathbf{e} + \frac{1}{P_m \bar{\rho}} (\nabla \times \mathbf{B})^2 \right)$, combines contributions from viscous dissipation and magnetic dissipation. Here, c_1 is a constant, R is the gas constant, $\hat{\boldsymbol{\sigma}}$ represents the stress tensor, $\mathbf{e}$ is the strain rate tensor, and P_m is the magnetic Prandtl number. This term captures the effects of both viscous and magnetic dissipation on the evolution of entropy in the fluid.

Together, these terms describe how entropy is transported, diffused, and dissipated within the fluid, incorporating both thermal and magnetic effects. The entropy equation thus provides a comprehensive framework for understanding the thermodynamic behavior of fluid systems in the presence of flow and magnetic fields.

Magnetic induction equation. The induction equation arises from a combination of Maxwell's equations—specifically Faraday's law of induction and Ampère's law—as well as Ohm's law for conductive fluids. These equations describe how electric and magnetic fields interact with moving conductive fluids. The magnetic induction equation can initially be expressed in a dimensional form as:

$$\partial_t \mathbf{B} = \nabla \times (\mathbf{u} \times \mathbf{B}) + \frac{1}{\mu_0 \sigma} \nabla^2 \mathbf{B}. \tag{3.11}$$

Here, μ_0 is the permeability of free space, and σ is the electrical conductivity.

To simplify analysis, the equation can be non-dimensionalized by introducing characteristic scales for magnetic field strength, fluid velocity, length, and time. This process involves scaling each variable by these characteristic values, resulting in a dimensionless form of the equation:

$$\partial_t \mathbf{B} = \nabla \times (\mathbf{u} \times \mathbf{B}) + P_m^{-1} \nabla^2 \mathbf{B}. \tag{3.12}$$

In this equation, the first term represents the temporal change of the magnetic field, indicating how the magnetic flux density varies with time. The second term $\nabla \times (\mathbf{u} \times \mathbf{B})$ describes the advection of the magnetic field by the fluid velocity $\mathbf{u}$. This term accounts for the transport of magnetic field lines by the fluid flow, influencing the spatial distribution and configuration of the magnetic field. The third term $P_m^{-1} \nabla^2 \mathbf{B}$ represents the diffusion of the magnetic field. Here, P_m is the magnetic Prandtl number, which quantifies the ratio of viscosity to magnetic diffusivity in the medium. This term indicates how the magnetic field diffuses over space due to internal friction within the conducting medium, smoothing out variations over time. The induction equation thus encapsulates the interplay between fluid advection and magnetic diffusion, providing a comprehensive framework for understanding the dynamic evolution of magnetic fields within physical systems.

3.2.1.3 Non-dimensional parameters

The key non-dimensional parameters governing the anelastic approximation in spherical shell include:

Radius ratio (η). The radius ratio η quantifies the relative sizes of the inner (r_i) and outer (r_o) radii of a spherical shell. It is expressed as:

$$\eta = \frac{r_i}{r_o}. \tag{3.13}$$

Polytropic Index (n). The polytropic index n characterizes the relationship between pressure and density in a polytropic gas, which follows the polytropic equation of state:

$$P = K\bar{\rho}^{\frac{n+1}{n}}, \tag{3.14}$$

where P is the pressure, $\bar{\rho}$ is the density, and K is a constant related to the specific entropy of the system. The polytropic index n describes how the pressure and density scale with each other in the reference state, and it helps model various astrophysical and geophysical processes, such as stellar interiors or planetary cores, where the equation of state deviates from an ideal gas law. For example, a low value of n represents a stiff equation of state (e.g., incompressible fluid), while a high value of n indicates a more compressible system.

Density scale number (N_ρ). The density scale number N_ρ indicates the logarithmic ratio of the density at the inner ($\bar{\rho}(r_i)$) and outer ($\bar{\rho}(r_o)$) boundaries, given by:

$$N_\rho = \ln\left(\frac{\bar{\rho}(r_i)}{\bar{\rho}(r_o)}\right). \tag{3.15}$$

Rayleigh number (R). The Rayleigh number R represents the intensity of buoyancy-driven flow. It is defined as:

$$\mathrm{R} = \frac{c_1 T_c d^2 \Delta S}{\nu_c \kappa_c}, \tag{3.16}$$

where c_1 is a constant $c_1 = ((1+\eta)(1-\zeta_o))/((1-\eta)^2)$, T_c is a characteristic temperature, d is the depth of the fluid layer, ΔS is the entropy difference, ν_c is the kinematic viscosity, and κ_c is the thermal diffusivity.

Prandtl number (P_r). The Prandtl number P_r measures the ratio of momentum diffusivity to thermal diffusivity, defined as:

$$P_r = \frac{\nu_c}{\kappa_c}, \tag{3.17}$$

where ν_c is the constant kinematic viscosity and κ_c is the constant thermal diffusivity.

Magnetic Prandtl number (P_m). The magnetic Prandtl number P_m indicates the ratio of kinematic viscosity to magnetic diffusivity, defined as:

$$P_m = \frac{\nu_c}{\lambda}, \tag{3.18}$$

where ν_c is the kinematic viscosity and λ is the magnetic diffusivity.

Coriolis number (τ). The Coriolis number τ quantifies the rotational effects on the fluid motion, defined as:

$$\tau = \frac{2\Omega_0 d^2}{\nu_c}, \tag{3.19}$$

where Ω is the angular velocity of rotation, d is the characteristic length scale, and ν_c is the kinematic viscosity.

These non-dimensional parameters provide insight into the relative importance of various physical processes, including rotation, buoyancy, diffusion, and magnetic field effects, thereby governing the system's overall behavior and stability.

3.2.1.4 Poloidal and Toroidal Decomposition

To solve the governing equations presented above, the velocity and magnetic field are first split into their poloidal and toroidal components. This decomposition is expressed as follows:

$$\bar{\rho}\mathbf{u} = \nabla \times (\mathbf{r}w) + \nabla \times (\nabla \times (\mathbf{r}v)), \tag{3.20}$$

$$\mathbf{B} = \nabla \times (\mathbf{r}g) + \nabla \times (\nabla \times (\mathbf{r}h)). \tag{3.21}$$

Here, $\bar{\rho}\mathbf{u}$ represents the mass flux, where $\bar{\rho}$ is the reference density and $\mathbf{u}$ is the velocity vector. The vector $\mathbf{B}$ denotes the magnetic flux density. Both fields are solenoidal (divergence-free), which is a key property utilized in their decomposition. The position vector in spherical coordinates is denoted by $\mathbf{r}$, while v and w are the poloidal and toroidal scalar potentials for the velocity field, and h and g are the poloidal and toroidal scalar potentials for the magnetic field. This method simplifies the complexity of the equations by breaking down the vector fields into components that can be more easily managed and solved, leveraging the solenoidal nature of the fields.

3.2.1.5 Boundary conditions

This section discusses the boundary conditions using poloidal and toroidal scalars for the velocity and magnetic fields.

Velocity field. In fluid dynamics, boundary conditions are essential for characterizing the behavior of velocity fields in a fluid. Two common boundary conditions are the "no-slip" condition and the "stress-free" condition.

The no-slip condition states that the velocity of the fluid at a boundary is equal to the velocity of that boundary itself. For stationary boundaries, this results in the following equations:

$$v = 0, \quad \partial_r v = 0, \quad w = 0, \quad \text{at} \quad r = r_i, r_o, \tag{3.22}$$

where v denotes the axial velocity, ∂_r represents the radial derivative, and w indicates the azimuthal velocity component. The equation $v = 0$ indicates that the axial velocity is zero at the boundaries. The condition $\partial_r v = 0$ signifies that the radial derivative of the axial velocity is also zero, implying no velocity gradient at the boundaries. Additionally, $w = 0$ denotes that the azimuthal velocity component is zero at the boundaries.

The "stress-free" condition is applied when there is no shear stress acting at the boundaries, leading to a different set of equations:

$$v = 0, \quad \partial_r^2 v - \frac{\bar{\rho}'}{\bar{\rho} r} \partial_r (rv) = 0, \quad \partial_r w - \frac{\bar{\rho}'}{\bar{\rho}} w = 0 \quad \text{at} \quad r = r_i, r_o. \tag{3.23}$$

The first equation, $v = 0$, reaffirms that the axial velocity is zero at the boundaries, consistent with the no-slip condition. The second equation, $\partial_r^2 v - \frac{\bar{\rho}'}{\bar{\rho} r} \partial_r (rv) = 0$, is derived from the momentum equations for incompressible flow and ensures the balance of forces in the radial direction by relating the second radial derivative of the axial velocity to the density gradient. The term $\frac{\bar{\rho}'}{\bar{\rho} r}$ accounts for the effect of density variation on the radial flow dynamics. The third equation, $\partial_r w - \frac{\bar{\rho}'}{\bar{\rho}} w = 0$, describes how the tangential velocity varies with the radius. This relationship ensures that the change in tangential velocity is proportional to the density variation, thereby maintaining the stress-free condition.

Entropy. For the entropy, a fixed contrast is imposed between the inner and outer surfaces, leading to the following boundary conditions:

$$S = 1 \quad \text{at} \quad r = r_i, \quad S = 0 \quad \text{at} \quad r = r_o. \tag{3.24}$$

The boundary condition $S = 1$ at $r = r_i$ implies that the inner surface is characterized by a maximum entropy state, often associated with the presence of a heat source or a higher temperature region. Conversely, the condition $S = 0$ at $r = r_o$ indicates that the outer surface represents a minimum entropy state, typically found in cooler regions or boundaries that dissipate heat.

These conditions can be derived from physical principles such as the second law of thermodynamics, which dictates that heat flows from regions of higher temperature (and thus higher entropy) to regions of lower temperature (and lower entropy). In this context, the entropy profile $S(r)$ is defined to reflect the thermal gradient established by the temperature difference between the inner and outer surfaces.

By imposing these specific values of entropy at the boundaries, one can ensure that the entropy gradient within the fluid is consistent with the thermal conditions of the system, leading to a well-defined entropy distribution as a function of the radial position r. This helps facilitate further analysis of the thermodynamic properties and behavior of the fluid within the defined domain.

Magnetic fields. The vacuum boundary conditions for the magnetic field are derived from the assumption of an electrically insulating external region. The gradients of g and h (which are related to the magnetic field components) are zero. Furthermore, the function g is equal to $h - h_e$, where h_e represents the potential field outside the spherical shell. This potential field h_e arises from the requirement that, in the electrically insulating regions outside the shell (at $r = r_i$ and $r = r_o$), the magnetic field must be described by a potential function, as no currents exist

in these regions. The magnetic field inside the shell must smoothly match the external potential field h_e at these boundaries. These conditions are represented by:

$$g = h - h^{(e)} = \frac{\partial}{\partial r}(h - h^{(e)}) = 0. \tag{3.25}$$

We applied the anelastic model and specific boundary conditions in our paper titled "Differential rotation in convecting spherical shells with non-uniform viscosity and entropy diffusivity [90]." The results of this study are discussed further in Chapter 7.

3.2.2 Reduction to Boussinesq approximation

In a significant portion of the findings presented in this thesis, we rely on the widely used Boussinesq approximation. This approximation simplifies the modelling of fluid dynamics by assuming that the density variations are small and can be neglected except in buoyancy terms. In the static state, the density is treated as uniform and constant, represented mathematically as $\tilde{\rho}_0(r) \longrightarrow \rho_0 = \text{const.}$, which significantly simplifies the equations. While this assumption disregards minor variations in density with distance from the center of the shell, it remains physically accurate under the conditions of weak stratification and small temperature differences, as outlined below [32, 195, 196, 189, 91].

3.2.2.1 Basic state and assumptions

The Boussinesq approximation assumes that density ρ varies only in the buoyancy term and is otherwise constant:

$$\rho = \rho_0(1 - \alpha\vartheta), \tag{3.26}$$

where α is the thermal expansion coefficient, ρ_0 is the reference density, and ϑ represents the temperature deviation from the static state.

The static temperature distribution within the spherical shell is derived from the energy equation in spherical coordinates, specifically under the condition of no fluid motion. By applying the steady-state assumption and considering internal heat sources and boundary conditions, we simplify the energy equation to:

$$0 = \bar{\kappa}\nabla^2 T_s + \frac{q}{c_p}. \tag{3.27}$$

Here, $\bar{\kappa} = \frac{\kappa T}{\rho_c c_p}$ is the coefficient of thermal diffusivity, where κ is the thermal conductivity, T is the temperature, ρ_c is the reference density, and c_p is the specific heat capacity at constant pressure. Solving this equation yields the static temperature distribution, expressed as:

$$\begin{gathered} T_S = T_0 - \beta d^2 r^2/2 + \Delta T \eta r^{-1}(1-\eta)^{-2} \\ \beta = q/(3\kappa c_p) \\ T_0 = T_1 - \Delta T/(1-\eta), \quad T_S(r_i) = T_1, \quad T_S(r_o) = T_2, \quad \Delta T = T_2 - T_1 \end{gathered} \tag{3.28}$$

where T_1 and T_2 are constant temperatures at the inner and outer spherical boundaries, $\eta = r_i/r_o$ is the ratio of the inner radius r_i to the outer radius r_o, q is a uniform heat source density, κ is the thermal diffusivity, d is the shell thickness, and r is the radial position vector within the spherical shell.

For the polytropic reference state used in the anelastic approximation (section 3.2.1), the parameters c_0 and c_1 are defined as follows:

$$c_0 = \frac{2\zeta_o - \eta - 1}{1-\eta}, \quad c_1 = \frac{(1+\eta)(1-\zeta_o)}{(1-\eta)^2}, \quad \zeta_o = \frac{\eta+1}{\eta\exp(N_\rho/n)+1} \tag{3.29}$$

Under the Boussinesq approximation, these parameters simplify significantly due to the nearly constant density and temperature assumptions, where N_ρ, representing the number of density scale heights, is assumed to be close to zero, indicating weak stratification:

$$c_0 = 1, \quad c_1 = 0, \quad \zeta_o = 1. \tag{3.30}$$

Thus, the radial profile ζ simplifies to:

$$\zeta = c_0 + c_1 \frac{d}{r} = 1. \tag{3.31}$$

These simplifications reflect the Boussinesq assumption of a nearly isothermal reference state and weak density stratification.

3.2.2.2 Mathematical formulation

We have simplified the equations (3.6) - (3.12) from the anelastic approximation to the Boussinesq approximation. The governing equations are non-dimensionalized using the shell thickness ($d = r_o - r_i$) as a unit of length, d^2/ν as a unit of time, $\nu^2/(\gamma\alpha d^4)$ as a unit of temperature, $(\nu(\mu_0\rho)^{1/2})/d$ as a unit of magnetic flux density, ρ_c as a unit of density and T_c as a unit of temperature. Here, r_i and r_o are the inner and the outer radius, respectively; ν denotes the kinematic viscosity of the fluid, κ its thermal diffusivity, ρ its density and μ_0 its magnetic permeability. Thus, the governing equations of magnetohydrodynamics (MHD) under the Boussinesq approximation are as follows:

Continuity equations. In the Boussinesq approximation, the continuity equation (3.6) simplifies by assuming incompressible flow. This assumption states that the fluid density variations are negligible except where they influence buoyancy forces. Consequently, the continuity equation becomes:

$$\nabla \cdot \mathbf{u} = 0. \tag{3.32}$$

This form emphasizes that the velocity field $\mathbf{u}$ is divergence-free, reflecting the incompressible nature of the flow.

Gauss law for magnetism. The magnetic field is divergence-free, a condition that remains valid under the anelastic approximation. As expressed in equation (3.7), the condition for the magnetic flux density $\mathbf{B}$ is:

$$\nabla \cdot \mathbf{B} = 0. \tag{3.33}$$

This condition ensures the continuity of magnetic field lines and implies the absence of magnetic monopoles within the system.

Momentum equation. To derive the momentum equation under the Boussinesq approximation, several simplifications and substitutions are necessary in the equation (3.8). The Boussinesq approximation assumes that density variations are negligible except in the buoyancy term, simplifying or removing terms involving ρ_c, $\bar{\rho}$, and density gradients. Entropy perturbation S is approximated linearly by the temperature perturbation ϑ:

$$S = \frac{c_p}{\bar{T}} \vartheta, \tag{3.34}$$

where c_p denotes the specific heat at constant pressure and $\bar{T}$ represents the reference temperature. By using the basic vector identities alongside the incompressibility assumptions $\nabla \cdot \mathbf{u} = 0$ and $\nabla \cdot \mathbf{B} = 0$, lead to the simplified momentum equation in the Boussinesq approximation:

$$\left(\frac{\partial}{\partial t} + \mathbf{u} \cdot \nabla\right) \mathbf{u} = -\nabla \pi - \tau \mathbf{k} \times \mathbf{u} + \vartheta \mathbf{r} + \nabla^2 \mathbf{u} + \mathbf{B} \cdot \nabla \mathbf{B}. \tag{3.35}$$

Here, π represents a reduced pressure (ratio of the thermodynamic pressure to the constant density), $\tau = \frac{2\Omega d^2}{\nu}$ is the Coriolis number accounting for rotation effects, $\mathbf{k}$ denotes the unit vector in the vertical direction, and ϑ signifies the temperature deviation from the static state. This equation governs the momentum balance in the Boussinesq approximation, encompassing buoyancy, Coriolis forces, temperature effects, viscous diffusion, and magnetic interactions.

Temperature equation. To derive the temperature equation under the Boussinesq approximation, several simplifications and substitutions are applied in the equation (3.10). We assume a linear relationship between entropy perturbation S and temperature perturbation ϑ as given in the equation (3.34). By setting $c_1 = 0$ and substituting S with $\frac{c_p}{\bar{T}}\vartheta$ in the equation (3.10), and adding source term, we obtain:

$$P_r \left(\frac{\partial \vartheta}{\partial t} + \mathbf{u} \cdot \nabla \vartheta\right) = \nabla^2 \vartheta + \left(R_i + R_e \eta \frac{r^{-3}}{(1-\eta)^2}\right) (\mathbf{r} \cdot \mathbf{u}), \tag{3.36}$$

where $P_r = \frac{\nu}{\kappa}$ represents the Prandtl number, κ is the thermal diffusivity, ν is the kinematic viscosity, R_i and R_e are the internal and external thermal Rayleigh numbers, respectively, η is the radius ratio, $\mathbf{r}$ is the radial unit vector, and $\mathbf{u}$ is the velocity field.

Magnetic induction equation. For the magnetic induction equation, we start by applying the vector identity for the curl of a cross product on equation (3.12):

$$\nabla \times (\mathbf{u} \times \mathbf{B}) = (\mathbf{B} \cdot \nabla)\mathbf{u} - (\mathbf{u} \cdot \nabla)\mathbf{B} + \mathbf{u}(\nabla \cdot \mathbf{B}) - \mathbf{B}(\nabla \cdot \mathbf{u}). \tag{3.37}$$

In the Boussinesq approximation, which assumes incompressible flow ($\nabla \cdot \mathbf{u} = 0$) and a divergence-free magnetic field ($\nabla \cdot \mathbf{B} = 0$), the term $\mathbf{u}(\nabla \cdot \mathbf{B})$ and $\mathbf{B}(\nabla \cdot \mathbf{u})$ simplifies to zero. Thus, the Boussinesq magnetic induction equation simplifies to:

$$P_m \left(\frac{\partial \mathbf{B}}{\partial t} + \mathbf{u} \cdot \nabla \mathbf{B} \right) = P_m (\mathbf{B} \cdot \nabla)\mathbf{u} + \nabla^2 \mathbf{B}, \tag{3.38}$$

where $P_m = \frac{\nu}{\lambda}$ is the magnetic Prandtl number, representing the ratio of kinematic viscosity to magnetic diffusivity. This equation describes the evolution of the magnetic field under the Boussinesq approximation, accounting for advection by the velocity field and diffusion of the magnetic field.

3.2.2.3 Non-dimensional parameters

The key non-dimensional parameters governing the Boussinesq approximation in spherical shell include:

Internal thermal Rayleigh number (R_i). The internal thermal Rayleigh number, defined as

$$R_i = \frac{\alpha \gamma \beta d^6}{\nu \kappa}, \tag{3.39}$$

where α is the thermal expansion coefficient, γ is the gravitational acceleration, β is the heat source density, ν is viscosity, and κ is thermal diffusivity. The internal Rayleigh number quantifies the stability and intensity of buoyancy-driven convection within a fluid system. It is particularly relevant in scenarios where heat is generated or dissipated internally, such as in geophysical or astrophysical contexts, and it indicates how effectively buoyancy forces can overcome viscous and thermal diffusion effects. A higher R_i typically indicates a greater potential for convective instabilities within the fluid.

External thermal Rayleigh number (R_e). The external thermal Rayleigh number is given by

$$R_e = \frac{\alpha\gamma\Delta T d^4}{\nu\kappa}, \tag{3.40}$$

where $\Delta T = T_2 - T_1$ represents the temperature difference between outer and inner boundaries. The external Rayleigh number characterizes the convection processes that occur in the surrounding fluid due to thermal gradients at the boundaries of a system. It is significant in assessing the influence of external temperature variations on fluid motion. The R_e value helps determine whether the external thermal effects lead to stable or unstable convection patterns. A high R_e implies that external thermal forces may induce significant convective flows, potentially impacting the overall thermal behavior of the system.

Coriolis Number (τ): The Coriolis number is defined as

$$\tau = \frac{2\Omega d^2}{\nu}, \tag{3.41}$$

where Ω denotes the angular velocity of rotation.

Prandtl and magnetic Prandtl numbers (P_r) and (P_m). The Prandtl and Magnetic Prandtl numbers are defined as

$$P_r = \frac{\nu}{\kappa}, \quad P_m = \frac{\nu}{\lambda}, \tag{3.42}$$

where ν is viscosity, κ is thermal diffusivity, and λ is magnetic diffusivity.

These parameters collectively characterize the behavior of convection-driven dynamo phenomena within the context of astrophysical and geophysical applications.

3.2.2.4 Poloidal and Toroidal Decomposition

To solve the governing equations presented above under the Boussinesq Approximation, the velocity and magnetic field are first split into their poloidal and toroidal components. This decomposition is expressed as follows [213].:

$$\mathbf{u} = \nabla \times (\mathbf{r}w) + \nabla \times (\nabla \times (\mathbf{r}v)), \tag{3.43}$$

$$\mathbf{B} = \nabla \times (\mathbf{r}g) + \nabla \times (\nabla \times (\mathbf{r}h)). \tag{3.44}$$

Here, $\mathbf{u}$ is the velocity vector, and the vector $\mathbf{B}$ denotes the magnetic flux density. Both fields are solenoidal (divergence-free), which is a key property utilized in their decomposition. The position vector in spherical coordinates is denoted by $\mathbf{r}$, while v and w are the poloidal and toroidal scalar potentials for the velocity field, and h and g are the poloidal and toroidal scalar potentials for the magnetic field.

The scalar fields v, w, g, and h are subsequently expanded using orthogonal polynomials, a topic to be explored in Chapter 4. The focus will be on solving equations under the Boussinesq Approximation. The same procedural approach can be applied to equations under the anelastic Approximation, with necessary modifications as required.

3.2.2.5 Boundary conditions

This section describes the boundary conditions imposed on the velocity field and related variables in a specific physical scenario. The boundary conditions vary depending on whether the system has an insulating inner core, a finitely conducting inner core, or a perfectly conducting inner core.

Velocity field. When no-slip boundary conditions applied at the inner and outer boundaries (denoted by $r = r_i$ and $r = r_o$ respectively), the radial velocity component (v) and the azimuthal velocity component (w) are both zero, and there's no change in the radial velocity ($\partial_r v$). These conditions are represented by:

$$v = \partial_r v = w = 0, \quad \text{at} \quad r = r_i, r_o. \tag{3.45}$$

Stress-free boundary conditions involve zero tangential stress at the boundaries. They specify that the second radial derivative of v is zero, and there's no change in the tangential velocity ($\partial_r w$). These conditions are represented by:

$$v = \frac{\partial^2 v}{\partial r^2} = \frac{\partial}{\partial r}\left(\frac{w}{r}\right) = 0, \quad \text{at} \quad r = r_i, r_o. \tag{3.46}$$

Insulating inner core. In this scenario, additional conditions apply at the inner and outer boundaries. The gradients of g and h (which are related to the magnetic field components) are zero. Furthermore, the function g is equal to $h - h_e$, where h_e represents the potential field outside the spherical shell. This potential field h_e arises from the requirement that, in the electrically insulating regions outside the shell (at $r = r_i$ and $r = r_o$), the magnetic field must be described by a potential function, as no currents exist in these regions. The magnetic field inside the shell must smoothly match the external potential field h_e at these boundaries. These conditions are represented by:

$$g = h - h^{(e)} = \frac{\partial}{\partial r}(h - h^{(e)}) = 0. \tag{3.47}$$

We applied the Boussinesq approximation and specific boundary conditions in our papers titled "Effects of shell thickness on cross-helicity generation in convection-driven spherical dynamos [189]" and "A study of global magnetic helicity in self-consistent spherical dynamos [91]." The results of these studies are discussed further in Chapters 5 and 6.

3.3 Taylor's constraint and Taylor-Proudman theorem

In the context of fluid dynamics within rotating spherical systems, the anelastic and Boussinesq approximations play a crucial role in simplifying the governing equations of magnetohydrodynamics (MHD). These approximations provide foundational insights into fluid behavior under specific conditions. Building upon these foundational concepts, we now explore two fundamental theorems governing MHD in rotating systems: Taylor's constraint and the Taylor-Proudman theorem [209].

The Taylor-Proudman theorem applies when the magnetic field's influence is negligible, describing a scenario of rapid rotation, inviscid flow, and steadiness. Under these assumptions, the relevant MHD equations simplify significantly. One of the key equations that emerges from this simplification is the momentum equation, given by:

$$2\Omega \boldsymbol{k} \times \boldsymbol{u} = -\frac{1}{\rho}\nabla p, \tag{3.48}$$

where Ω is the angular velocity of the fluid, $\boldsymbol{k}$ is the unit vector along the rotation axis, $\boldsymbol{u}$ is the fluid velocity vector, ρ is the fluid density, and p is the pressure. This theorem dictates that under these conditions, the only permissible solution is a steady azimuthal flow given by:

$$u(s) = \frac{\hat{\phi}}{2\Omega\rho}\frac{\partial p}{\partial s}, \tag{3.49}$$

where s denotes the cylindrical polar coordinate and $\hat{\phi}$ represents the azimuthal unit vector. However, direct application of this theorem to convection problems in spherical geometry faces challenges due to singularities.

In scenarios where convection processes are dominant and involve the magnetic field significantly (known as the magnetostrophic approximation), the MHD equation modifies to:

$$2\Omega \boldsymbol{k} \times \boldsymbol{u} = -\frac{1}{\rho}\nabla p - \alpha \Theta \boldsymbol{g} + \frac{1}{\rho \mu}(\nabla \times \boldsymbol{B}) \times \boldsymbol{B}, \tag{3.50}$$

where α is the thermal expansion coefficient, Θ is the temperature, $\boldsymbol{g}$ is the gravitational acceleration, and μ is the magnetic permeability.

To derive Taylor's constraint, we integrate the azimuthal (ϕ) component of the Lorentz force over a geostrophic cylinder. A geostrophic cylinder is a cylindrical volume aligned with the axis of rotation and spanning the region within the rotating fluid. The integration is performed over the surface $C(s)$ of the cylinder with radius s, where s is the cylindrical radial coordinate.

The key condition leading to Taylor's constraint is that, for the system to remain in equilibrium in a rapidly rotating, magnetized spherical fluid, the azimuthal component of the Lorentz force must average to zero over the geostrophic cylinder. Mathematically, this is expressed as:

$$\int_{C(s)} \frac{1}{\rho \mu} [(\nabla \times \boldsymbol{B}) \times \boldsymbol{B}]_{\phi} \, dS = 0, \tag{3.51}$$

where $[(\nabla \times \boldsymbol{B}) \times \boldsymbol{B}]_{\phi}$ represents the azimuthal (ϕ) component of the Lorentz force, and dS is an infinitesimal area element on the surface of the geostrophic cylinder $C(s)$.

The derivation assumes axisymmetry, meaning the system is symmetric around the rotation axis, which simplifies the equations. The velocity field and magnetic field satisfy specific boundary conditions at the inner and outer boundaries of the fluid shell (i.e., at $r = r_i$ and $r = r_o$). Additionally, the steady-state approximation is used, where time derivatives are neglected under the assumption that the system evolves slowly compared to the rotation period, leading to a quasi-

steady state. Taylor's constraint plays a fundamental role in MHD dynamo theory for rapidly rotating spherical systems, such as planetary or stellar interiors. However, finding solutions for convection-driven dynamos that satisfy this constraint remains a long-standing challenge in the field.

To conclude this chapter, we have discussed key concepts in fluid dynamics within rotating spherical systems, focusing on the anelastic and Boussinesq approximations. These approximations are pivotal in simplifying the equations governing magnetohydrodynamics (MHD) under specific conditions. Building upon these insights, our next focus will be on numerical methods for solving equations under the Boussinesq approximation. The same procedural approach applies to equations under the anelastic approximation, with some necessary adjustments.

Chapter 4

Discretization and numerical method

Understanding the intricate dynamics of convection-driven dynamos within rotating spherical shells presents significant challenges in both geophysical and astrophysical research. Traditional analytical methods often simplify this complex interplay of nonlinearities and geometric complexities, thereby limiting their accuracy and real-world applicability. This constraint is particularly notable when modeling the geomagnetic field and solar dynamics, where linearized approaches fall short in capturing crucial nonlinear behaviors.

To overcome these limitations, numerical simulations serve as invaluable tools, offering the capability to approximate self-consistent solutions of dynamo equations with higher fidelity. In this context, the choice of numerical method becomes crucial, guided by considerations of accuracy, stability, computational efficiency, and the ability to handle the inherent spherical geometry of the problem.

Among spatial discretization methods, finite-difference and finite-element approaches are widely used but encounter challenges in maintaining accuracy, especially near the poles of a spherical surface. Spectral methods, however, emerge as particularly suitable due to their ability to achieve high accuracy using orthogonal basis functions such as spherical harmonics and Chebyshev polynomials. These methods facilitate the exact computation of spatial derivatives in spectral space, significantly reducing computational overhead compared to conventional methods by requiring lower resolution to achieve comparable accuracy.

The Pseudo-Spectral method, in particular, effectively combines these advantages with efficient temporal discretization, making it well-suited for the governing equations under the anelastic and Boussinesq approximations discussed in Chapter 3. Based on these considerations, we have chosen to simulate the scalar equations of the anelastic or Boussinesq approximations using a Pseudo-Spectral method. This approach was first successfully applied to the geodynamo problem by Glatzmaier and Roberts, demonstrating its efficacy in capturing the complex dynamics of convection-driven dynamos within spherical shells [85, 213].

This chapter delves into the implementation and implications of the Pseudo-Spectral method in simulating convection-driven dynamos within rotating spherical shells. By leveraging its capabilities, we aim to deepen our understanding of the dynamics governing such complex systems and contribute to advancements in geophysical and astrophysical research. The focus will be on solving equations under the Boussinesq approximation; the same procedural approach can be applied to equations under the anelastic approximation, with necessary modifications as required.

4.1 Pseudo-Spectral method

The Pseudo-Spectral method is a sophisticated numerical technique designed for the analysis of convection-driven dynamos within rotating spherical shells. This approach effectively integrates spectral spatial discretization with finite-difference temporal discretization, optimizing both accuracy and computational efficiency [85, 213].

In the Pseudo-Spectral method, orthogonal basis functions, such as spherical harmonics, are employed for angular decomposition, while Chebyshev polynomials facilitate radial decomposition. This dual approach allows for a precise representation of spatial variations in the unknown functions v, w, h, g across the spherical domain, which is essential for resolving the complex interactions and boundary conditions inherent in these systems.

A distinctive feature of the Pseudo-Spectral method is its mixed use of spectral and physical spaces through collocation points. This hybrid strategy enables exact computation of spatial derivatives in spectral space while utilizing collocation points in the physical domain for evaluating nonlinear radial functions. Specifically, the transformation to collocation points allows for more straightforward computation of these nonlinearities, significantly enhancing computational efficiency and reducing numerical artifacts, particularly in regions near the poles of the spherical surface.

For temporal evolution, the Pseudo-Spectral method integrates the Crank-Nicholson implicit method with the Adams-Bashforth explicit method. This combination ensures numerical stability while accurately capturing the time-dependent dynamics of dynamos. The overall computational efficiency of the Pseudo-Spectral method lies in its requirement for fewer grid points compared to traditional methods, rendering it particularly effective for simulating large-scale, three-dimensional, and highly coupled dynamo systems.

4.1.1 Spectral decomposition

Spectral decomposition is a key aspect of this method, involving the breakdown of functions into simpler components. Specifically, these functions are expressed using spherical harmonics in the angular directions and Chebyshev polynomials in the radial direction.

Angular decomposition. The equations for the spherical harmonics expansions of the poloidal and toroidal scalars for velocity ($\boldsymbol{V}$), magnetic field ($\boldsymbol{B}$), and temperature (ϑ) are:

$$
\begin{aligned}
v &= \sum_{l=0}^{\infty}\sum_{m=-l}^{l} V_l^m(r,t)P_l^m(\cos\Theta)e^{im\varphi}, \quad w = r\sum_{l=0}^{\infty}\sum_{m=-l}^{l} W_l^m(r,t)P_l^m(\cos\Theta)e^{im\varphi} \\
g &= \frac{1}{r}\sum_{l=0}^{\infty}\sum_{m=-l}^{l} G_l^m(r,t)P_l^m(\cos\Theta)e^{im\varphi}, \quad h = \frac{1}{r}\sum_{l=0}^{\infty}\sum_{m=-l}^{l} H_l^m(r,t)P_l^m(\cos\Theta)e^{im\varphi}, \\
\vartheta &= \sum_{l=0}^{\infty}\sum_{m=-l}^{l} \vartheta_l^m(r,t)P_l^m(\cos\Theta)e^{im\varphi}.
\end{aligned}
\tag{4.1}
$$

The factors r and r^{-1} in the above equations are not essential but contribute to the numerical stability of the method. These equations express the quantities in terms of their angular components, capturing the variation of each physical quantity with respect to the angles Θ (colatitude) and φ (longitude), while also depending on radial distance (r) and time t. The velocity poloidal scalar (v) is represented as a summation of terms involving V_l^m, where l and m represent angular

modes. A convenient simplification is that $F_{-m} = (-1)^m (F_m)^*$, where F_m is the coefficient in any of the above expansions. The symmetry holds because all fields must be real (for example, $v = v^*$, where v^* denotes the complex conjugate of v). Thus, only the coefficients with $m \geq 0$ need to be stored, which reduces the memory requirements of the method.

In these equations, P_l^m represents associated Legendre functions, describing the angular part of the functions. These functions illustrate how quantities vary with direction in a spherical coordinate system. The radial functions V_l^m, W_l^m, G_l^m, H_l^m, and ϑ_l^m signify the contributions of each angular mode (l,m) to the overall behavior of the quantities, offering insights into the system's complex dynamics. This spatial discretization method simplifies intricate functions into manageable components, facilitating their numerical solution. Through representation in terms of spherical harmonics, we can effectively simulate the system dynamics under study.

Angular transformations. In general, a function $f(r,\theta,\varphi)$ can be transformed into its coefficients $F_l^m(r)$ and vice versa through specific transformation methods. The function can be expressed as:

$$f(r,\theta,\varphi) = \sum_{m=-l}^{l} e^{im\varphi} \sum_{l=0}^{\infty} P_l^m(\cos\theta) F_l^m(r), \tag{4.2}$$

where P_l^m denotes the associated Legendre functions, which capture the angular dependencies.

To compute the coefficients, an integral involving the associated Legendre functions and the original function evaluated at specific angles is employed:

$$F_l^m(r) = (-1)^m \frac{2l+1}{4\pi} \int_{-1}^{1} P_l^{-m}(x) \int_0^{2\pi} e^{-im\varphi} f(r, \arccos x, \varphi)\, d\varphi \quad \text{with} \quad x = \cos\theta. \tag{4.3}$$

This process typically consists of two parts: the forward transformation, which relates the coefficients to the function, and the inverse transformation, which reconstructs the function from its coefficients. The inverse transformation begins with the FFT and requires the calculation of a projection integral, approximated using Gauss quadrature methods:

$$\int_{-1}^{1} g(x)\,dx = \sum_{i=0}^{L} w_i g(x_i), \tag{4.4}$$

where w_i are the Gauss-Legendre weights, and x_i are the abscissas computed through established procedures.

The transformation from the indices l and m to the angles θ and φ involves a weighted sum of associated Legendre functions and requires a matrix-vector multiplication followed by an FFT over the index m. The latitudinal transformation presents unique challenges, as no fast algorithm for the Legendre transform currently exists. Nevertheless, it is possible to enhance the computational efficiency of the matrix-vector multiplication by exploiting the symmetry properties of the Legendre functions.

Associated Legendre functions and orthogonality relation. Associated Legendre functions $P_l^m(x)$ are crucial for the angular decomposition of functions in spherical geometries. These functions are defined in terms of Legendre polynomials and are essential for expressing angular dependencies in both physical and mathematical contexts. Below, we outline their key properties and the orthogonality relation that underpins their use in spherical harmonic expansions.

- **Associated Legendre Functions $P_l^m(x)$.** The recurrence relation for $P_l^m(x)$ over l is given by:

$$(l-m)P_l^m(x) = x(2l-1)P_{l-1}^m(x) - (l+m-1)P_{l-2}^m(x). \tag{4.5}$$

This relation allows the computation of $P_l^m(x)$ in terms of the polynomials of lower orders. To start the recursion, we need initial conditions. The initial condition for $P_m^m(x)$ is given by:

$$P_m^m(x) = (-1)^m \cdot 1 \cdot 3 \cdot 5 \cdot \ldots \cdot (2m-1)(1-x^2)^{m/2}. \tag{4.6}$$

And the polynomial for $P_{m+1}^m(x)$ is:

$$P_{m+1}^m(x) = x(2m+1)P_m^m(x). \tag{4.7}$$

The derivative of $P_l^m(x)$ with respect to x is given by:

$$(1-x^2)\frac{d}{dx}P_l^m(x) = -lxP_l^m(x) + (l+m)P_{l-1}^m(x). \tag{4.8}$$

This derivative equation is crucial for computing gradients involving associated Legendre functions. The functions with negative m is given by:

$$P_l^{-m}(x) = (-1)^m \frac{(l-m)!}{(l+m)!}P_l^m(x). \tag{4.9}$$

These functions allow for the computation of associated Legendre functions for negative m indices using known values for positive m.

- **Orthogonality Relation.** The orthogonality relation states that the integral of the product of two associated Legendre functions $P_{l'}^{m'}(x)$ and $P_l^m(x)$ over x is non-zero only when $l = l'$ and $m = m'$:

$$\int_{-1}^{1} P_{l'}^{-m'}(x)P_l^m(x)\,dx = (-1)^m \frac{2}{2l+1}\delta_{ll'}\delta_{mm'}. \tag{4.10}$$

It simplifies the computation of coefficients in spherical harmonic expansions and ensures the accuracy of such decompositions.

Radial decomposition using Chebyshev polynomials

Radial decomposition using Chebyshev polynomials is an effective method for analyzing and approximating functions, particularly in contexts involving spherical symmetry or radial dependencies. Chebyshev polynomials, denoted as $T_n(x)$, are a sequence of orthogonal polynomials defined over the interval $[-1,1]$. They minimize interpolation errors and are defined by:

$$T_n(x) = \cos(n \arccos(x)), \quad x \in [-1,1]. \tag{4.11}$$

The orthogonality of these polynomials makes them ideal for approximating functions in radial decomposition, allowing for systematic representation of functions as a series and facilitating efficient numerical solutions.

Chebyshev polynomial expansion of radial functions

The radial functions of interest, denoted as V_l^m and W_l^m, can be expanded in N_r Chebyshev polynomials as follows:

$$V_l^m(r,t) = \sum_{n=0}^{N_r-1} v_{l,n}^m(t) T_n(x(r)), \quad W_l^m(r,t) = \sum_{n=0}^{N_r-1} w_{l,n}^m(t) T_n(x(r)), \tag{4.12}$$

where x is transformed to fit collocation points situated within the spherical shell defined between $r_i = 0$ and $r_o = 1$ by $x = 2(r - r_i) - 1$. This transformation is crucial for ensuring that the Chebyshev polynomials can effectively represent the radial behavior of the functions.

An important aspect of this computational scheme is the transformation between the physical coordinates (r, θ, φ) and the spectral coordinates (n, l, m). Such conversions are necessary for efficiently treating nonlinear terms and computing derivatives, which are most conveniently handled in spectral space.

The collocation points, which serve as discrete evaluation points for the functions in direct space, are positioned as follows:

$$r_j = r_i + \frac{1}{2}\left(1 + \cos\left(\pi \frac{j-1}{N_r - 1}\right)\right), \quad j = 1, 2, \ldots, N_r. \tag{4.13}$$

Here, N_r represents the total number of Chebyshev polynomials used in the expansion. It determines the resolution of the approximation; a larger N_r enables a more accurate representation of functions, particularly those exhibiting rapid changes. Therefore, the expansion for V_l^m at the collocation points can be expressed as:

$$V_l^m(r_j, t) = \sum_{n=0}^{N_r - 1} v_{l,n}^m(t) \cos\left(n\pi \frac{j-1}{N_r - 1}\right), \quad j = 1, 2, \ldots, N_r. \tag{4.14}$$

This representation illustrates that the sum effectively becomes a cosine transform, enabling efficient calculations of the radial components of the functions being analyzed. The cosine transform aligns well with the Fast Fourier Transform (FFT) algorithms, providing significant computational advantages for converting between radial and Chebyshev spaces.

Appropriateness for radial symmetry. The Chebyshev polynomials are particularly well-suited for functions exhibiting radial symmetry because they effectively capture variations in radial distance while preserving their orthogonality properties. This characteristic minimizes numerical errors and enhances the stability of computations involving radial functions.

In conclusion, radial decomposition using Chebyshev polynomials offers a systematic approach for analyzing functions, especially those that exhibit radial symmetry or significant variation with respect to the radial distance r from a central point. This method not only supports theoretical investigations but also enhances computational efficiency by decomposing complex functions into manageable components. As a result, it facilitates accurate modeling and analysis across various scientific and engineering disciplines.

4.1.2 Temporal discretization

Temporal discretization is essential in numerical simulations for approximating the time evolution of dynamic systems governed by partial differential equations (PDEs). For convection-driven dynamos in rotating spherical shells [213, 42, 199], we employ a combination of the Crank-Nicolson method and the Adams-Bashforth method. This combined approach is chosen for its accuracy, stability, and computational efficiency.

We need to solve a system of reaction-diffusion parabolic equations, which in abstract form can be written as:

$$\partial_t y = \Lambda y + N(y) \tag{4.15}$$

where y represents all unknowns, Λ represents diffusion-like terms, $N(y)$ represents the reaction terms and is a nonlinear function that also includes coupling terms, and terms that may be linear but difficult to compute in some sense. While there are boundary conditions that close the problem, they do not influence the choice of numerical methods for temporal discretization. We will use an IMEX (implicit-explicit time-stepping) method. IMEX is a standard time-stepping approach for nonlinear reaction-diffusion equations. It aims to inherit the unconditional stability characteristic of implicit time-stepping schemes, such as the Crank-Nicholson method for diffusion equations, while combining it with a convenient explicit computation of difficult and nonlinear terms for which stability results are not well established.

To split the problem, we express it as:

$$[\partial_t y]_\Lambda + [\partial_t y]_N = \Lambda y + N(y), \tag{4.16}$$

where $[\partial_t y]_\Lambda$ and $[\partial_t y]_N$ represent the contribution to the time derivative due to the Λ terms and to the $N(y)$ respectively, so that the equation is a sum of two equations

$$\begin{aligned} [\partial_t y]_N &= N(y), \\ [\partial_t y]_\Lambda &= \Lambda y. \end{aligned} \tag{4.17}$$

Crank-Nicolson method. The Crank-Nicholson method is an implicit time integration scheme commonly used to solve diffusion-dominated problems due to its unconditional stability. This characteristic allows it to maintain stability even with larger time steps, making it ideal for addressing the linear diffusion term Λy in our system. By incorporating function values from both the current and subsequent time steps, the Crank-Nicholson method not only achieves stability but also enhances accuracy. This approach ensures that the numerical solution converges correctly over time, making the method particularly effective for simulating phenomena where diffusion plays a significant role.

Time-stepping process for Crank-Nicolson. The time discretization for the diffusion term Λy using the Crank-Nicolson method is as follows:

1. Solve the first equation explicitly, i.e. evaluate the RHS using known values from the previous time steps. For instance, an Euler step is,

$$\left[y^{k+1} - y^k\right]_N = hN\left(y^k\right). \tag{4.18}$$

2. Solve the equation implicitly, e.g by a Crank-Nicolson scheme, which is derived as follows. Take a forward Euler step:

$$\left[y^{k+1} - y^k\right]_\Lambda = h\Lambda y^k. \tag{4.19}$$

3. Take a backward Euler step

$$\left[y^{k+1}-y^{k}\right]_{\Lambda}=h\Lambda y^{k+1}. \tag{4.20}$$

4. Add the two steps:

$$\left[y^{k+1}-y^{k}\right]_{\Lambda}=\frac{h}{2}\left(\Lambda y^{k}+\Lambda y^{k+1}\right). \tag{4.21}$$

5. Add the two contributions back together to obtain an implicit-explicit time step

$$y^{k+1}-y^{k}=\left[y^{k+1}-y^{k}\right]_{N}+\left[y^{k+1}-y^{k}\right]_{\Lambda}=\frac{h}{2}\left(\Lambda y^{k}+\Lambda y^{k+1}\right)+hN\left(y^{k}\right). \tag{4.22}$$

6. Formulate the linear system for the implicit time step:

$$\left(1-\frac{h}{2}\Lambda\right)y^{k+1}=\left(1+\frac{h}{2}\Lambda\right)y^{k}+hN\left(y^{k}\right), \tag{4.23}$$

and the formal solution is given by:

$$y^{k+1}=\left(1-\frac{h}{2}\Lambda\right)^{-1}\left[\left(1+\frac{h}{2}\Lambda\right)y^{k}+hN\left(y^{k}\right)\right]. \tag{4.24}$$

Adams-Bashforth method. The Adams-Bashforth method is an explicit integration technique that computes the function value at the next time step based on known values from previous steps, allowing for efficient numerical simulations without the need to solve a system of equations. This characteristic enhances its computational efficiency, particularly when addressing the nonlinear reaction terms $N(y)$ in the governing equations. By employing the second-order Adams-Bashforth method, we gain increased accuracy compared to first-order methods like Euler. This method utilizes information from two previous time steps, resulting in a more precise approximation of the solution.

Time-stepping process for Adams-Bashforth method. The Adams-Bashforth step for the nonlinear term $N(y)$ is as follows:

$$\left[y^{k+1}-y^{k}\right]_{N}=\frac{h}{2}\left(3N\left(y^{k}\right)-N\left(y^{k-1}\right)\right), \tag{4.25}$$

This formulation ensures that the contribution from the nonlinear terms is second-order accurate in time. Since this method only relies on previous time step values, it is efficient and avoids the computational cost of solving implicit equations.

Combined iterative solution (IMEX approach). To solve the full system of reaction-diffusion equations, we adopt a combined iterative approach, where the Crank-Nicolson method is used to handle the diffusion term Λy, and the Adams-Bashforth method handles the nonlinear reaction term $N(y)$.

The resulting implicit-explicit (IMEX) scheme ensures stability for the diffusion term while maintaining computational efficiency for the nonlinear terms. The explicit nature of the Adams-Bashforth method means that we can avoid the costly computation of nonlinear terms in an implicit scheme while ensuring that the solution remains accurate and stable over time.

The combined solution, obtained by merging equations (4.24) and (4.25), is given by:

$$y^{k+1}=\left(1-\frac{h}{2}\Lambda\right)^{-1}\left[\left(1+\frac{h}{2}\Lambda\right)y^{k}+\frac{h}{2}\left(3N\left(y^{k}\right)-N\left(y^{k-1}\right)\right)\right]. \tag{4.26}$$

This equation is formed by applying the Crank-Nicolson method to the linear term Λy, which is treated implicitly for stability. In the Crank-Nicolson scheme, the nonlinear term $N(y^{k})$ is originally treated explicitly as $hN(y^{k})$.

However, instead of using $hN(y^k)$, we improve the approximation of the nonlinear term by replacing it with the Adams-Bashforth method, which is a higher-order explicit scheme. The Adams-Bashforth formula provides a more accurate approximation for the nonlinear term using information from the current and previous time steps, $N(y^k)$ and $N(y^{k-1})$, resulting in the term $\frac{h}{2}\left(3N(y^k) - N(y^{k-1})\right)$. Thus, the final equation combines the implicit treatment of the linear term from Crank-Nicolson with the explicit treatment of the nonlinear term from Adams-Bashforth, leading to a stable and efficient IMEX (implicit-explicit) scheme.

Temporal discretization, thus, plays a crucial role in accurately capturing the time evolution of convection-driven dynamos, ensuring the numerical solution aligns closely with the underlying physical phenomena.

4.2 Implementation procedure

This section outlines the procedural steps involved in implementing the numerical method for simulating convection-driven dynamos within rotating spherical shells. The methodological procedures are structured as follows:

4.2.1 Initialization

- **Read Parameters and Allocate Memory:**
    1. Read parameters, which include resolution defined in terms of:
        - **Number of spherical harmonic modes:**
            * L: Maximum degree of the spherical harmonic representation.

        * M: Maximum azimuthal mode.
        * N: Number of radial modes.
    - **Number of collocation points:**
        * n_r: Number of points in the radial direction.
        * n_θ: Number of points in the polar direction.
        * n_ϕ: Number of points in the azimuthal direction.
2. Allocate memory for storing spectral components and intermediate results. The storage requirement is approximately $20 \times N \times L \times 2M$ real numbers, accounting for both real and imaginary parts stored alternately.
3. Proper resolution is critical for ensuring accurate simulation results. Higher values of L and M allow for a more detailed representation of flow and magnetic field structures. To prevent aliasing in nonlinear terms, we apply the dealiasing rule, utilizing modes up to $L_d = \frac{2}{3}L$ and $M_d = \frac{2}{3}M$. Here, L_d and M_d represent the maximum retained modes in the radial and azimuthal directions, respectively, ensuring sufficient resolution during nonlinear interactions. The transformation between physical space, represented by coordinates (r, θ, φ), and spectral space, characterized by modal indices (L, M, N), facilitates efficient numerical computations. This approach allows nonlinear terms to be handled in the spectral domain while preserving accuracy through well-defined relationships such as $n_r = N$, $n_\theta = L+1$, and $n_\phi = 2M+1$.

Pre-computation:

- Compute and invert matrices required for the implicit time step.
- Compute associated Legendre functions $P_l^m(x)$, their derivatives, and functions with negative m indices:
    - Use recursion formulas to compute $P_l^m(x)$.
    - Evaluate derivatives and negative m functions using specified relations.
- Precompute these functions as they are needed for calculating magnetic field components and their transformations between spherical and Cartesian coordinates.

Initialization of Fields:

- Load initial $f_{l,n}^{m}$-fields in spectral space.
- Compute their first and second derivatives to prepare for time integration.

4.2.2 Time Stepping Loop:

1. **Time Integration**:
    - Perform the following steps iteratively for each time step:
        (a) **Compute Explicit Terms**: Evaluate the explicit terms in the right-hand sides of the equations using the specified formulas. This computation can be parallelized over the radial index n, meaning the terms for different values of n can be computed simultaneously, significantly speeding up the overall process. Parallelization allows the workload to be distributed across multiple processors or cores, with each core computing the terms for different values of n at the same time, drastically reducing the total computation time.
        (b) **Implicit Crank-Nicolson Method**: Use the implicit Crank-Nicolson method for temporal discretization.
        (c) **Adams-Bashforth Step**: For non-linear terms, employ an explicit Adams-Bashforth step, substituting the first step with an Euler formula.
        (d) **Matrix-Vector Multiplications**: Perform matrix-vector multiplications required for the implicit step. This step is parallelized over the azimuthal index m, although load balancing can be challenging due to varying computational requirements across different m.
        (e) **Compute Radial Derivatives**: At the end of each time step, compute radial derivatives of $f_{l,n}^{m}$ and save the right-hand sides of the equations.
2. **Save Intermediate States**:

- Periodically save various quantities of interest, such as kinetic and magnetic energies of the flow, for analysis and visualization.

3. **End of Time Stepping Loop**:
   - Save the final state of the simulation after completing all time steps.
   - End the program execution.

This section provides a structured overview of the procedural steps involved in implementing the numerical method for studying convection-driven dynamos. It combines spectral decomposition methods (using spherical harmonics and associated Legendre functions) with efficient temporal integration techniques (Crank-Nicolson and Adams-Bashforth methods). Each step contributes to the overall methodology aimed at simulating the complex dynamics within rotating spherical shells, highlighting the systematic approach to handling both spatial and temporal discretization challenges.

4.3 Concluding remarks

This Chapter has outlined the numerical methodology used for simulating convection-driven dynamos in rotating spherical shells. The results of these simulations will be discussed in detail in Chapters 5, 6, and 7, providing insights into the dynamics and implications of our findings.

Chapter 5

Effects of shell thickness on cross-helicity generation in convection-driven spherical dynamos

The results presented in this chapter have been published in [189]. This chapter follows the published paper and includes figures from the paper with the agreement of all authors.

5.1 Introduction

This chapter investigates the relative significance of helicity and cross-helicity electromotive dynamo effects in generating self-sustained magnetic fields through chaotic thermal convection within rotating spherical shells, with a focus on how these effects vary with shell thickness. Direct numerical simulations reveal the coexistence of two distinct regimes of dynamo solutions across shell aspect ratios ranging from 0.25 to 0.6: a mean-field dipolar regime and a fluctuating dipolar regime. In-depth analysis of these coexisting dynamo attractors involves a comparison of their properties, including differences in temporal behavior and spatial structures of both

magnetic fields and rotating thermal convection. The helicity α -effect and the cross-helicity γ-effect are found to be comparable in intensity within the fluctuating dipolar dynamo regime, where their ratio does not vary significantly with the shell thickness. In contrast, within the mean-field dipolar dynamo regime the helicity α-effect dominates by approximately two orders of magnitude and becomes stronger with decreasing shell thickness.

In cosmic objects, thermal flows play a pivotal role in shaping their distinct large-scale features, notably their self-sustained magnetic fields [159, 26]. Noteworthy examples include the Sun and several planets within the Solar System, all of which exhibit considerable magnetic fields [238, 30]. The solar magnetic field, for instance, drives solar activity and exerts significant influence on planetary atmospheres [216, 158], crucially shielding Earth from solar radiation [177]. Moreover, gas giants, ice giants, and even the moons of Jupiter boast substantial magnetic fields [36].

As discussed in the background chapter, thermal flows within cosmic objects, such as the Sun and planets, drive dynamo processes responsible for generating their large-scale magnetic fields. These magnetic fields arise from convective motions of electrically conductive fluids, driven by thermal buoyancy forces within their interiors. Consequently, thermal convection within celestial bodies manifests as highly turbulent, profoundly influenced by both rotation and the self-generated magnetic fields. Consequently, considerable attention has been dedicated to unraveling the complexities of this intriguing and consequential phenomenon. For comprehensive insights, readers are directed to topical reviews by [35, 107, 220], along with their respective references.

The conceptual understanding of large-scale magnetic field generation through dynamos is rooted in mean-field dynamo theory [122, 16, 151], a well-established framework within magnetohydrodynamic turbulence. Central to this theory is the modelling of turbulence in the mean electromotive force—a critical term in the Reynolds-averaged magnetic induction equation governing the evolution of large-scale magnetic fields, as discussed in detail in Section 5.6 below. This electromotive force is typically represented through an expansion in terms of the mean field and its spatial derivatives, with the expansion coefficients colloquially termed "mean-field effects."

The turbulent helicity effect, often referred to as the α-effect, has been extensively explored in the literature on mean-field dynamo theory [16, 18], contrasting with the relatively limited attention given to the cross-helicity effect, also known as the γ-effect [232, 226, 167]. This disparity arises from the prevalent treatment of turbulence, where the influence of large-scale velocity is often neglected due to the Galilean invariance of the momentum equation. However, such neglect overlooks significant large-scale shear effects, which are particularly pronounced in systems featuring substantial large-scale rotation, such as the Solar internal differential rotation—a well-measured phenomenon [211, 183]. Numerical simulations further suggest that such rotation plays a pivotal role in the dynamo process, potentially accounting for the periodic oscillations observed in convection-driven spherical dynamos [32, 196].

Studies of plane-parallel flows corroborate the non-negligible contribution of cross-helicity effects relative to helicity effects [93, 229]. Beyond its relevance to dynamo generation, cross-helicity assumes significance as an observable in solar studies. For instance, measurements of the cross-helicity component $\langle u_z b_z \rangle$ at the Solar surface are attainable through instruments like the Swedish 1-m Solar Telescope, facilitating calculations of the magnetic eddy diffusivity of the quiet Sun via quasilinear mean-field theory [176].

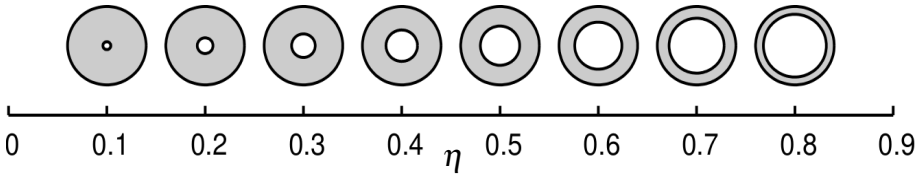

Figure 5.1: Illustration of shell thickness aspect ratio variation.

Cross-helicity remains largely unexplored in models of self-consistent dynamos driven by thermal convection in rotating spherical shells, prompting the aim of this chapter is to contribute to this understudied domain. The primary objective of this study is to investigate the relative significance of helicity and cross-helicity effects concerning the thickness of the convective shell. Intuitive reasoning suggests that the α-effect holds importance in geodynamo scenarios, whereas the cross-helicity effect assumes prominence in the global solar dynamo. Specifically, the geodynamo operates within the relatively thick fluid outer core of the Earth, where the development of large-scale columnar structures is anticipated. These coherent structures, exhibiting significant vorticity, enhance the helicity α-effect by promoting organized flow patterns that effectively twist and link magnetic field lines, thereby facilitating the generation of strong mean electromotive forces. In contrast, the global solar dynamo operates within the thinner solar convection zone, where the maintenance of columnar structures is challenging. Consequently, the vorticity within this zone may exhibit a less regular structure, potentially elevating the relative importance of the cross-helicity effect.

To test this hypothesis, we conduct a series of dynamo simulations, varying primarily in their shell thickness aspect ratio $\eta = r_i/r_o$, as illustrated in Figure 5.1, while maintaining other governing parameters constant. In addition to assessing the relative strength of helicity and cross-helicity effects, we analyze the mechanisms underlying electromotive force generation and its spatial distribution. The variation in shell thickness is pertinent not only to the geodynamo scenario but also to the geological evolution of the Earth. Notably, the inner core of the Earth did not exist at the planet's formation but rather nucleated later in its geological history, continuing to expand over time [59, 124].

The distinction between the geodynamo and the solar global dynamo extends beyond their respective operational environments, encompassing the nature of their magnetic field behavior. While the geodynamo typically exhibits a dominant and infrequently reversing dipole, the solar global dynamo displays a regular periodic cycle. To elucidate this fundamental contrast and facilitate a comparative analysis, we conducted this study at parameter values known to support the coexistence of two distinct dynamo regimes for shell aspect ratios between 0.25 and 0.6 [195, 39, 198]. These branches differ significantly in their magnetic field properties, with one branch maintaining a non-reversing nature while the other follows a cyclic pattern. Furthermore, notable distinctions exist in the intensity and profile of zonal flows between these branches.

In parameter space, the non-reversing branch is generally found in regions characterized by strong magnetic field intensities and stable zonal flows, often corresponding to conditions where the Lorentz force is dominant. Conversely, the cyclic branch appears in regions with slightly weaker magnetic fields, where fluctuations in magnetic energy and changes in flow patterns become more pronounced. This regime can be related to the known weak-field and strong-field regimes; while the weak-field regime is characterized by multipolar field configurations, the strong-field regime tends to exhibit predominantly dipolar behavior. The transition between these regimes is marked by complex interactions between flow dynamics and magnetic field generation, leading to varying magnetic field profiles and intensities.

Given the anticipated divergence in the mechanisms underlying helicity and cross-helicity generation between the two branches, our study aims to investigate both branches comprehensively. The phenomenon of bistability inherent in the coexistence of these dynamo branches may play a crucial role in aperiodic magnetic field polarity reversals, a characteristic trait of the geodynamo [37], as well as in the regular cycle observed in the solar dynamo [136]. In earlier research

[195], Simitev and Busse have explored the hysteretic transitions between these coexisting dynamo branches, examining the effects of varying the Rayleigh, Prandtl, and Coriolis numbers. In addition to these efforts, this chapter demonstrates the distinct dynamo branches persist even when varying the shell thickness parameter η.

The structure of this thesis chapter mirrors that of the paper, outlined as follows: In section 5.2, we provide a comprehensive overview of the mathematical model employed and the numerical methods utilized for solution, laying the groundwork for subsequent analyses. Sections 5.3, 5.4 and 5.5 delve into the core of our investigation, detailing the array of dynamo simulations conducted with in the scope of this study. Particular emphasis is placed on elucidating the characteristics of the two coexisting dynamo branches, a novel exploration undertaken here, with a keen focus on their evolution in response to variations in the thickness of the convective shell. Additionally, we offer insights into the typical morphology and time-dependent behavior of thermal convection flows observed during these simulations. In Section 5.6, we provide a succinct summary of mean field arguments pertinent to the helicity and cross-helicity mechanisms governing the generation of large-scale magnetic fields, setting the stage for a deeper understanding of our findings. Subsequently, Section 5.7 serves as the focal point for assessing the cross-helicity properties inherent in our dynamo solutions, alongside a detailed examination of the relative contributions of the α- and γ-effects, shedding light on their respective roles in shaping the observed magnetic field behavior. Finally, in Section 5.8, we draw upon our findings to offer concluding remarks, synthesizing key insights gleaned from our investigation and highlighting avenues for future research.

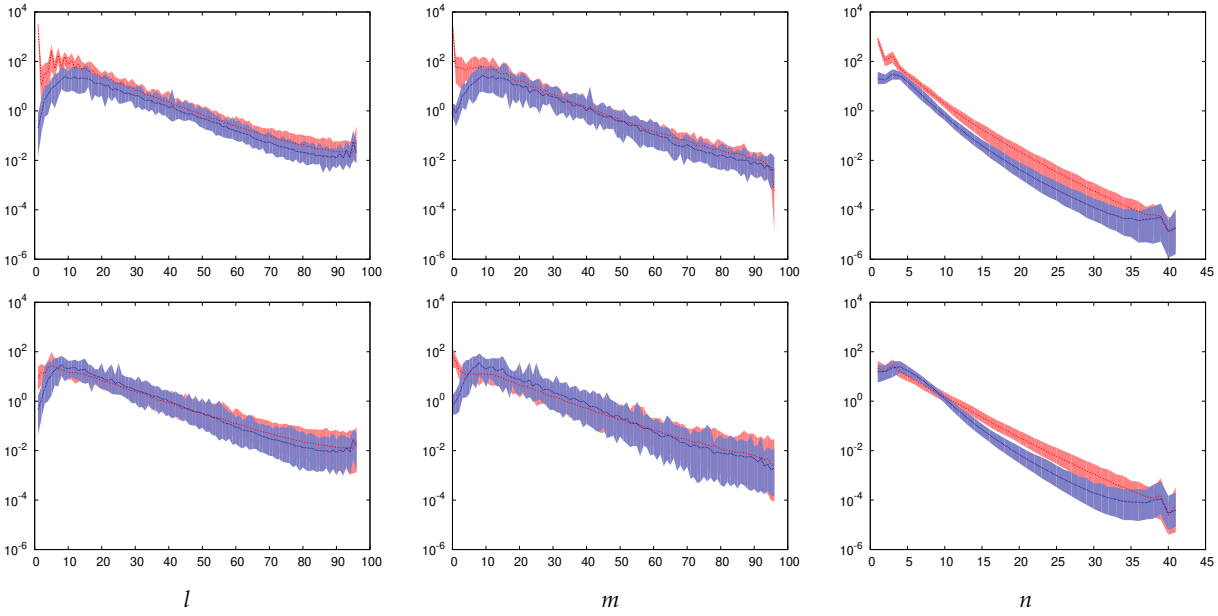

Figure 5.2: Typical power spectra of velocity (blue) and magnetic field (red). The top row shows a **MD** dynamo solution whereas the bottom row shows a **FD** dynamo solution both at $\eta = 0.4$, $R = 1500000$, $\tau = 2 \times 10^4$, $P_r = 0.75$ and $P_m = 1.5$. From left to right, power spectra as a function of the spherical harmonic degree l, order m, and Chebyshev polynomial degree n are shown respectively. Lines represent the average spectra and shaded areas go from the minimum to the maximum values for each mode in the averaging period. A period of one viscous-diffusion time unit is used for the time-averaging period in both cases.

5.2 Mathematical model

We consider a spherical shell filled with electrically conducting fluid. The shell rotates with a constant angular velocity $\mathbf{\Omega}$ about the vertical coordinate axis. We assume that a static state exists with the temperature distribution:

$$T_S = T_0 - \beta d^2 r^2/2, \tag{5.1a}$$

$$\beta = q/3\kappa c_p, \tag{5.1b}$$

$$T_0 = T_1 - (T_2 - T_1)/(1-\eta). \tag{5.1c}$$

The evolution of the system is governed by the equations of momentum, heat, and magnetic induction, along with solenoidality conditions for the velocity and magnetic fields under the Boussinesq approximation. Internal heating is considered in this study, modifying the temperature distribution within the spherical shell. Five dimensionless parameters are involved in the governing equations: the shell radius ratio η, the Rayleigh number R (here $R = R_i$, as defined in Chapter 3), the Coriolis number τ, the Prandtl number P_r, and the magnetic Prandtl number P_m. For the flow, we assume stress-free boundaries with fixed temperatures. For the magnetic field, we assume electrically insulating boundaries. Detailed descriptions of these equations can be found in Chapter 3 of the study. Refer to Chapter 4 for a discussion on the numerical methods used for their solution. We consider the simulations to be adequately resolved when the spectral powers of both kinetic and magnetic energies decrease by more than three orders of magnitude from their spectral peak to the cut-off wavelength [47]. In all cases presented here, the simulations were run with a resolution of $(n_r, n_\theta, n_\phi) = (41, 96, 193)$, where 41 collocation points were used in the radial direction, and spherical harmonics were included up to degree and order 96. This level of resolution is sufficient, as illustrated in Figure 5.2 for two representative dynamo solutions.

It is convenient to characterise the non-magnetic convection and the convection-driven dynamo solutions using their energy densities. To understand the interactions between various components of the flow, we decompose the kinetic energy density into mean poloidal, mean toroidal, fluctuating poloidal and fluctuating toroidal parts as follows

$$\overline{E}_p = \frac{1}{2}\langle |\, \nabla \times (\nabla \overline{v} \times \mathbf{r})\, |^2 \rangle, \quad \overline{E}_t = \frac{1}{2}\langle |\, \nabla \overline{w} \times \mathbf{r}\, |^2 \rangle, \tag{5.2a}$$

$$\widetilde{E}_p = \frac{1}{2}\langle |\, \nabla \times (\nabla \widetilde{v} \times \mathbf{r})\, |^2 \rangle, \quad \widetilde{E}_t = \frac{1}{2}\langle |\, \nabla \widetilde{w} \times \mathbf{r}\, |^2 \rangle, \tag{5.2b}$$

where $\langle \cdot \rangle$ indicates the average over the fluid shell and time as described in section 5.6 and $\overline{v}$ refers to the axisymmetric component of the poloidal scalar field v, while $\widetilde{v}$ is defined as $\widetilde{v} = v - \overline{v}$. The corresponding magnetic energy densities $\overline{M}_p$, $\overline{M}_t$, $\widetilde{M}_p$ and $\widetilde{M}_t$ are defined analogously with the scalar fields h and g for the magnetic field replacing v and w.

To assess the predominant configuration of the magnetic field, we define the dipolarity ratio

$$\mathscr{D} = \overline{M}_p / \widetilde{M}_p. \tag{5.3}$$

When $\overline{M}_p > \widetilde{M}_p$ then $\mathscr{D} > 1$ and the corresponding solutions will be referred to as "Mean Dipolar", for reasons to be explained below, and denoted by **MD** following [197]. When $\overline{M}_p < \widetilde{M}_p$ then $\mathscr{D} < 1$ and the corresponding solutions will be referred to as "Fluctuating Dipolar" and denoted by **FD**.

To quantify heat transport by convection the Nusselt numbers at the inner and outer spherical boundaries Nu_i and Nu_o are used. These are defined by

$$Nu_i = 1 - \frac{P}{r_i R} \left. \frac{\mathrm{d}\overline{\overline{\Theta}}}{\mathrm{d}r} \right|_{r=r_i}, \qquad Nu_o = 1 - \frac{P}{r_o R} \left. \frac{\mathrm{d}\overline{\overline{\Theta}}}{\mathrm{d}r} \right|_{r=r_o}, \tag{5.4}$$

where the double bar indicates the average over the spherical surface.

Other quantities are defined in the text as required.

Parameter values used. To explore how shell thickness influences non-magnetic convection properties and dynamo outcomes, we conducted a series of numerical simulations, adjusting the shell aspect ratio from $\eta = 0.1$ to $\eta = 0.7$. To ensure fair comparisons among simulations and to maintain a manageable workload, we kept all parameters constant except those dependent on the aspect ratio. The Prandtl number was set at $P_r = 0.75$, enabling us to employ a relatively low magnetic Prandtl number of $P_m = 1.5$ was used for the simulations. The Coriolis number was held constant at $\tau = 2 \times 10^4$, striking a balance between the rapid rotation rate observed in the geodynamo and the slower rotation rate characteristic of the solar dynamo. We ensured consistent dynamo driving by maintaining the Rayleigh number at a fixed ratio of $\frac{R}{R_c} = 3.8$, where

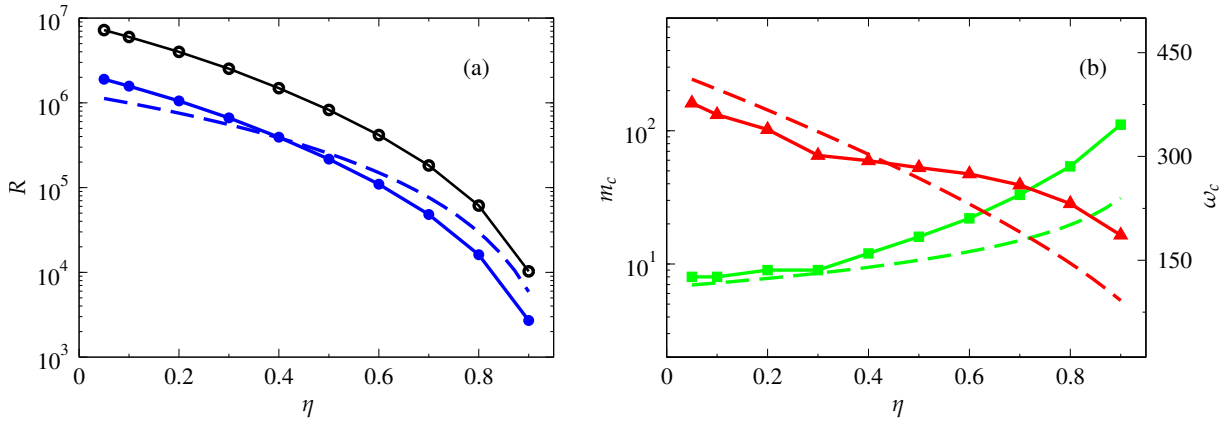

Figure 5.3: Critical parameter values for the onset of convection and values of the Rayleigh number used in this work as a function of the shell thickness aspect ratio η in the case $P_r = 0.75$, and $\tau = 2 \times 10^4$. (a) The critical Rayleigh number R_c for the linear onset of convection is plotted in solid blue curve marked by full circles. The values used in the simulations are given by $R = 3.8R_c$; they are plotted in solid black curve marked by empty circles. (b) The critical wave number m_c (left y-axis) and the critical frequency ω_c (right y-axis) for the onset of convection are denoted by green squares and red triangles, respectively. Local asymptotic approximations (5.6) are shown by correspondingly colored dashed curves in all panels.

R_c is the critical Rayleigh number for convection onset, recalculated for each shell thickness as depicted in Figure 5.3. The critical Rayleigh number values necessary for this adjustment were determined as elaborated in the subsequent section, where we delve into the general characteristics of thermal convection onset.

5.3 Onset of thermal convection: linear analysis

The initiation of thermal convection within rapidly rotating spherical shells has been extensively explored, including recent investigations as part of thermo-compositional convection studies [187]. Typically, two primary regimes emerge at the onset: columnar convection and equatorially-attached convection. Equatorially-attached convection occurs at lower Prandtl number (P_r) values, characterized by non-spiraling rolls confined near the equator with a substantial azimuthal

length scale, resembling inertial oscillations [33]. Conversely, the columnar regime manifests at moderate to high P_r values, showcasing elongated rolls parallel to the axis of rotation with strong spiraling and a shorter azimuthal length scale. At the chosen Prandtl and Coriolis numbers, our simulations align with the columnar regime of rapidly rotating convection.

For the precise determination of critical parameters at the onset of convection, we utilized our open-source numerical code [188], which employs a Galerkin spectral projection method based on Zhang and Busse work [235] to solve linearized versions of the governing equations. This approach leads to a generalized eigenvalue problem, where for a given set of parameters (e.g., Rayleigh number R, Prandtl number P_r, Coriolis number τ, and azimuthal wave number m), we compute various eigenvalues representing the complex growth rates of different convection modes. The real part of the eigenvalue corresponds to the growth rate of the mode, while the imaginary part corresponds to the oscillation frequency. To determine the critical values—specifically the critical Rayleigh number R_c, the associated frequency ω_c, and the critical azimuthal wave number m_c—we find the marginal state where all convective modes decay except for the fastest growing mode, which has zero real growth rate. In this state, the real part of the complex growth rate is zero, and the imaginary part corresponds to the frequency ω_c of the mode. Additionally, the Rayleigh number is minimized over all possible m values to ensure that we capture the critical mode corresponding to the onset of convection. Subsequent numerical extremization and continuation procedures track the marginally stable curve in parameter space, as explained in [187]. The resulting critical values, showcased in Figure 5.3, reveal that R_c and ω_c decrease with decreasing shell thickness, while the critical azimuthal wave number m_c increases.

It's intriguing to juxtapose and validate these findings against theoretical insights into the onset of convection in rapidly rotating systems. The asymptotic analysis of this problem boasts a rich history of local and global linear stability analyses [172, 34, 201, 108, 58, 187]. Converting results of [225] to our dimensionless parameters and scales, we obtain

$$\begin{aligned} R_c &= 7.252 \left(\frac{P_r \tau}{1+P_r} \right)^{4/3} (1-\eta)^{7/3}, \\ m_c &= 0.328 \left(\frac{P_r \tau}{1+P_r} \right)^{1/3} (1-\eta)^{-2/3}, \\ \omega_c &= 0.762 \left(\frac{\tau^2}{P_r (1+P_r)^2} \right)^{1/3} (1-\eta)^{2/3}, \end{aligned} \tag{5.5}$$

for critical parameters of viscous columnar convection in an internally heated spherical shell. While these expressions are derived under assumptions that may not fully align with the specific conditions of our spherical shell setup, such as boundary conditions and flow dynamics, they nonetheless offer insights that are qualitatively consistent with the numerical results depicted in Figure 5.3, highlighting the general trends and behaviors observed in our simulations. In Figure 5.3(b), a slight kink in the critical frequency ω_c is observed around $\eta = 0.3$. While this feature may suggest a subtle change in the system's behavior, it has not been explored further, as it is outside the scope of the current study, which focuses on the general trends of the critical parameters for convection onset.

5.4 Finite-amplitude convection and dynamo dynamics

As the Rayleigh number is elevated beyond the onset point, rotating columnar convection experiences a series of transitions from steady flow patterns drifting with constant angular velocity to increasingly chaotic states, as extensively described in previous work [190]. When the amplitude of convection reaches a critical threshold, characterized by a magnetic Reynolds number ($R_m = P_m \sqrt{2E}$) on the order of 10^2, the onset of dynamo action typically occurs [193].

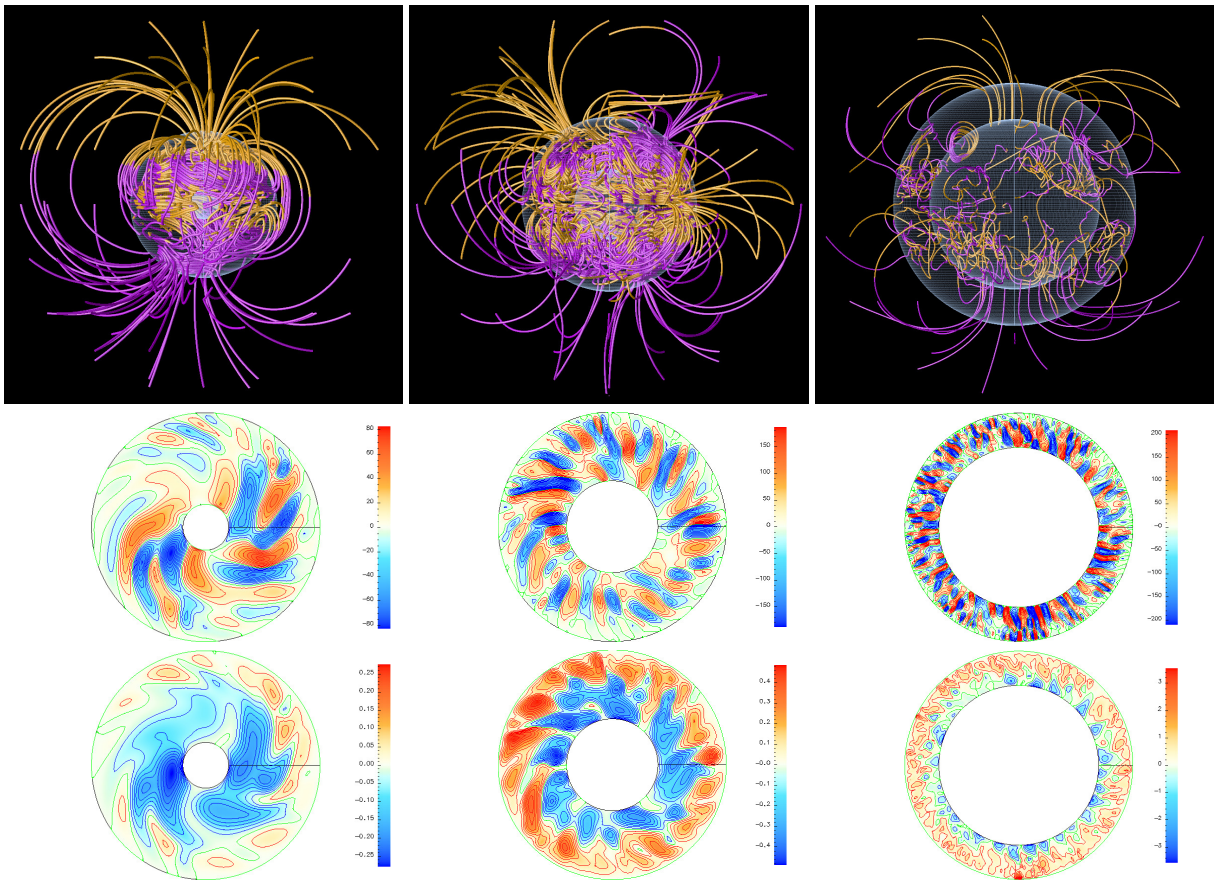

Figure 5.4: Snapshots of spatial structures of dynamo solutions with increasing shell thickness aspect ratio η and with $R = 3.8 \times R_c$, $\tau = 2 \times 10^4$, $P_r = 0.75$ and $P_m = 1.5$. Three cases are shown as follows: $\eta = 0.2$, $R = 4000000$ (left column); $\eta = 0.4$, $R = 1500000$ (middle column); and $\eta = 0.7$, $R = 180000$ (right column). Magnetic poloidal fieldlines are plotted in the top row, contours of the radial velocity u_r in the equatorial plane are plotted in the middle row, and contours of the temperature perturbation Θ in the equatorial plane are plotted in the bottom row.

Three examples of dynamo solutions, depicted in Figure 5.4, serve two purposes: (i) illustrating typical spatial features of chaotic thermal convection within rotating shells and the associated magnetic field morphology, and (ii) demonstrating how these features evolve with decreasing shell thickness. Outside the tangent cylinder, the flow comprises pairs of adjacent spiraling convection columns, as observed in the second row of Figure 5.4. Within these columns, fluid particles traverse clockwise and counterclockwise directions parallel to the equatorial plane, either ascending towards the poles or descending towards the equatorial plane as columns span

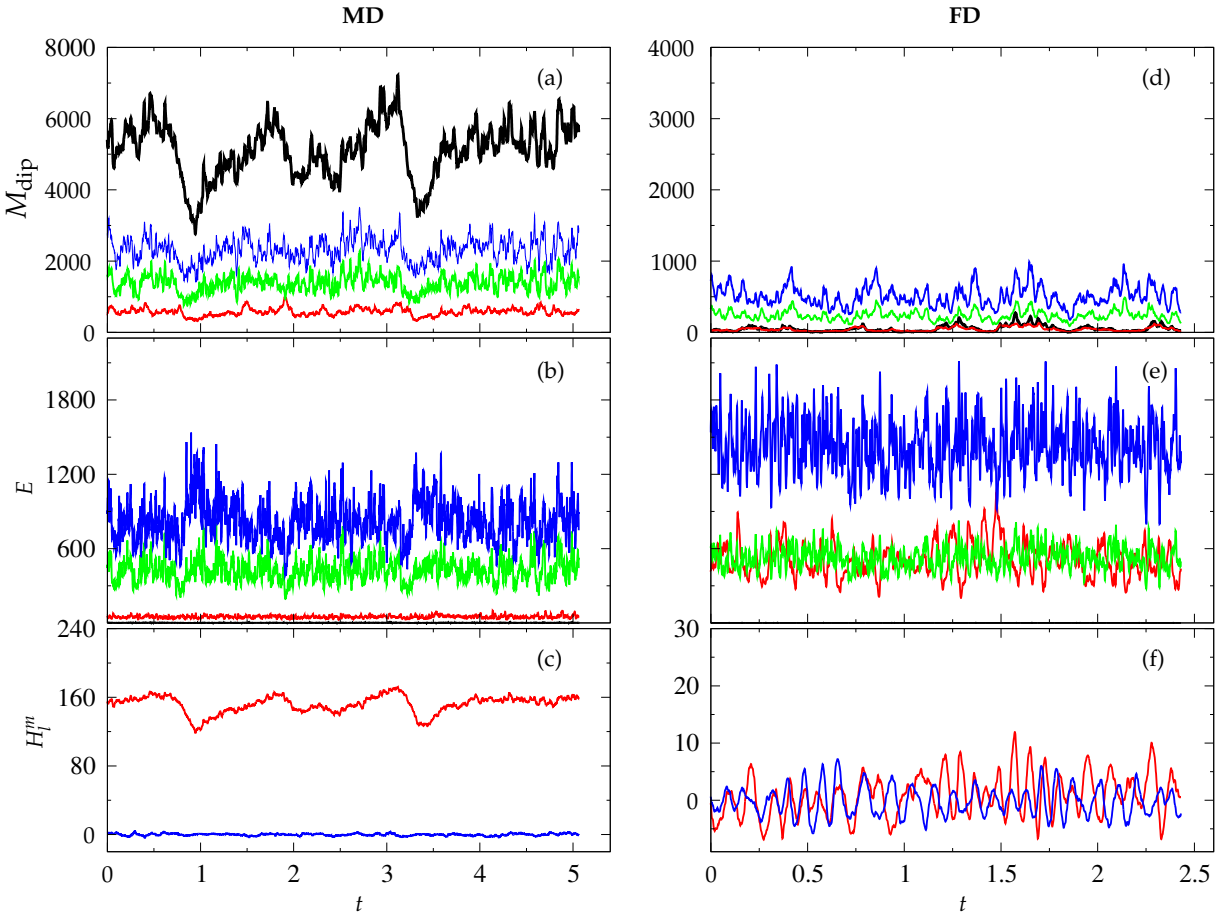

Figure 5.5: Chaotic dynamo attractors at identical parameter values – a MD dynamo (left column (a,b,c)) and a FD dynamo (right column (d,e,f)) both at $\eta = 0.5$, $R = 8.2 \times 10^5$, $\tau = 2 \times 10^4$, $P_r = 0.75$ and $P_m = 1.5$. Panels (a,d) show time series of magnetic dipolar energy densities, where M_{dip} represents magnetic dipolar energy density. Panels (b,e) show kinetic energy densities with E representing kinetic energy density. The component $\overline{X}_p$ is shown by solid black line, while $\overline{X}_t$, $\widetilde{X}_p$, and $\widetilde{X}_t$ are shown by red, green and blue lines, respectively. X stands for either M_{dip} or E. Panels (c,f) show the axial dipolar H_1^0 and the axial quadrupolar H_2^0 coefficients at midshell $r = (r_i + r_o)/2$ by red and blue lines, respectively. Note the very different ordinate scales between panels (a) and (d) and (c) and (f). The ordinate scales of panels (b) and (e) are identical.

the height of the convective shell. Consistent with linear analysis, decreasing shell thickness leads to a rapid increase in azimuthal wave number. In the case of thin shell solution ($\eta = 0.7$), fine-scale columns closely adjoin each other, exhibiting weaker spiraling and slower drift compared to thicker shell cases.

These convective patterns exert a profound influence on the structure and morphology of magnetic fields, as depicted in the first row of Figure 5.4. The magnetic field lines exhibit intricate knots and display a complex structure within the convective domain across all three cases. In the thicker shell instances ($\eta = 0.2$ and $\eta = 0.4$), magnetic field lines coil around convective columnar structures, indicative of toroidal field and poloidal field feedback and amplification processes. Beyond the convective domain, the magnetic field in the thickest shell case ($\eta = 0.2$) displays organized behavior, emanating from the polar regions as large bundles of opposite polarities. These field lines then close to form extensive overarching loops, characteristic of a strong dipolar field symmetry. A similar pattern is observed in the mid-thickness case ($\eta = 0.4$), albeit with multiple magnetic "poles" where strong bundles of vertical field lines emerge at the spherical domain's surface. In contrast, the thin shell case ($\eta = 0.7$) exhibits much less organized magnetic field behavior, with numerous field line coils within the convective domain and a barely visible but still dominant dipolar structure outside.

While the spatial structures described in relation to Figure 5.4 offer snapshots of the three dynamo solutions at fixed moments in time, an illustration of the temporal behavior exhibited in our dynamo simulations is provided in Figure 5.5. This figure plots the main magnetic and kinetic energy density components of two distinct dynamo cases as functions of time, highlighting the chaotic nature of the solutions. The time series exhibit continual oscillations around the mean values of the respective densities, with periods significantly shorter than the viscous diffusion time.

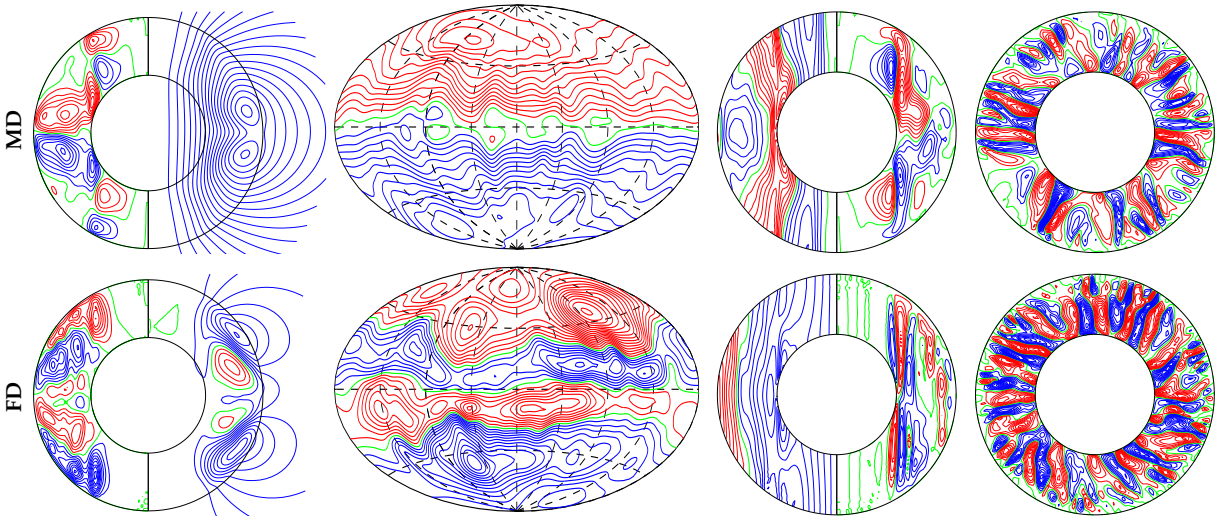

Figure 5.6: A **MD** (top row) and a **FD** (bottom row) dynamo solutions at $\eta = 0.5$, $R = 8.2 \times 10^5$, $\tau = 2 \times 10^4$, $P_r = 0.75$ and $P_m = 1.5$ corresponding to the cases shown in Figure 5.5. The first column shows meridional lines of constant $\overline{B_\varphi}$ in the left half and of $r \sin\theta \partial_\theta \overline{h} = const.$ in the right half. The second column shows lines of constant B_r at $r = 1.675 r_o$. The third column shows meridional lines of constant $\overline{u}_\varphi$ in the left half and of $r \sin\theta \partial_\theta \overline{v}$ in the right half. The fourth column shows contours of the radial flow u_r on the equatorial plane. Positive values are shown in red; negative values are shown in blue, and the zeroth contour line is shown in green.

The kinetic energy densities displayed in the second row of the figure reveal that the fluctuating components of motion dominate the flow, with the fluctuating toroidal velocity being the strongest. The mean poloidal component of motion is negligible in both cases, consistent with the constraint of the Proudman-Taylor theorem on motions parallel to the axis of rotation. Although the mean toroidal component, representing differential rotation, appears weak in both cases plotted in Figure 5.5, it is known to be the component most strongly affected in the presence of magnetic fields [193].

This observation leads us to consider the features of the magnetic energy densities plotted in the first row of Figure 5.5. Here, the differences between the two illustrated cases are more pronounced. The total magnetic energy density of the case in Figure 5.5(a) is approximately six times larger than that in Figure 5.5(d). More significantly, there is an essential qualitative difference in the balance of magnetic energy components. The axisymmetric poloidal component $\overline{M}_p$ is dominant in the case shown in Figure 5.5(a), while it contributes relatively less in the

case of Figure 5.5(d). The axial dipole coefficient H_1^0 and the axial quadrupole coefficient H_2^0 in Figure 5.5(c) and (f) reveal that this difference arises from the fact that the case on the left is dominated by a strong dipole, while the case on the right is less strongly dipolar, with the time series suggesting the presence of magnetic field oscillations.

The solutions depicted in Figure 5.5(a,b,c) and 5.5(d,e,f) represent two types of dipolar dynamos observed in numerical simulations [193, 48, 197, 155]: those with $\mathscr{D} > 1$, referred to as "Mean Dipolar" (**MD**), and those with $\mathscr{D} \leq 1$, termed "Fluctuating Dipolar" (**FD**). The typical spatial structures of the **MD** and **FD** dynamos are illustrated in Figure 5.6.

The radial magnetic field plotted in the second column of Figure 5.6 demonstrates the predominant dipolar symmetry of the dynamos, particularly evident in the **MD** case, where the north and south hemispheres exhibit entirely opposite polarities. In contrast, the **FD** case displays a band of reversed polarity near the equator, which propagates towards the poles over time, leading to periodically occurring reversals. The stationary dipole of the **MD** case is stronger in intensity and inhibits differential rotation.

This observation is supported by the profiles of differential rotation plotted in the left part of the third column of Figure 5.6, which exhibit marked differences. The **FD** case is characterized by stronger geostrophic rotation largely aligned with the tangent cylinder, while the mean zonal flow of the **MD** case is weaker and displays non-geostrophic rotation, particularly retrograde near the equator. Despite these differences, the columnar convective structure remains similar in both the **MD** and **FD** cases.

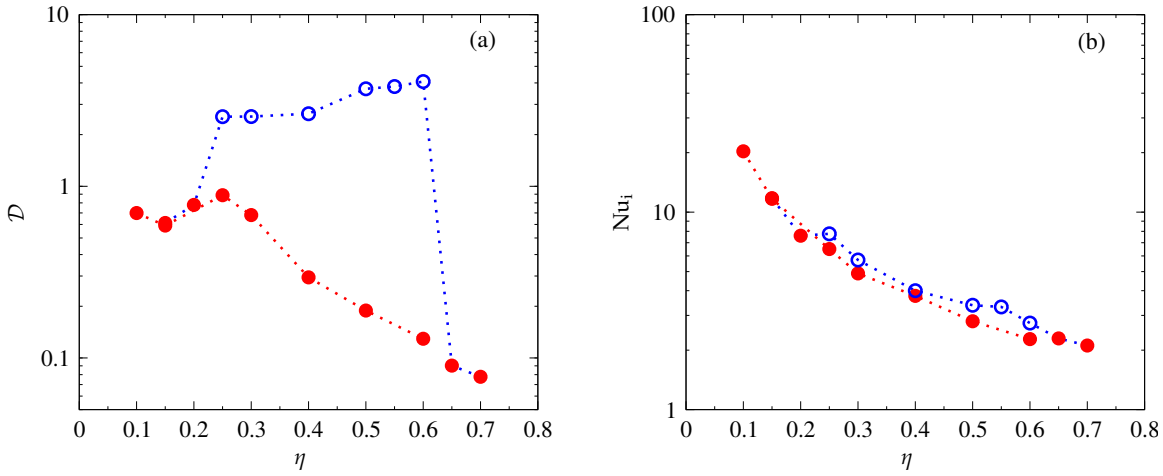

Figure 5.7: Bistability as a function of the shell thickness η. (a) The dipolarity ratio $\mathscr{D} = \overline{M}_p/\widetilde{M}_p$ and (b) the Nusselt number at $r = r_i$ in the cases $R = 3.8 \times R_c$, $\tau = 2 \times 10^4$, $P_r = 0.75$ and $P_m = 1.5$. Full red and empty blue circles indicate **FD** and **MD** dynamos, respectively. Red dotted lines and blue dotted lines connect dynamos that were started from **FD** and **MD** initial conditions, respectively.

5.5 Shell thickness variation: bistability and general effects

One of the most striking features of **MD** and **FD** dynamos is their ability to coexist at identical parameter values. This coexistence phenomenon was initially reported in [197]. Indeed, in each of the Figures 5.5, 5.6, and 5.2, two different cases obtained at the same parameter values are depicted. Within the parameter range where coexistence occurs, the initial conditions determine which of the two chaotic attractors will be realized.

Figure 5.7 illustrates both the dipolarity ratio $\mathscr{D}$ and the Nusselt number Nu_i as functions of the shell thickness aspect ratio η. Several observations can be made immediately. First, bistability seems to be present only for aspect ratios between $\eta = 0.25$ and $\eta = 0.6$. In contrast, outside this bistable region, only **FD** dynamos exist for $\eta < 0.25$ and $\eta > 0.6$. This contrasts with previous studies [197, 191] where alternating regimes appeared on each side of the hysteresis loop when continuation was performed as a function of all remaining parameters R, P_r, P_m, and τ. Our findings suggest that the dynamics are more constrained in our model due to variations in boundary conditions and the fixed governing parameters, leading to a more defined bistable re-

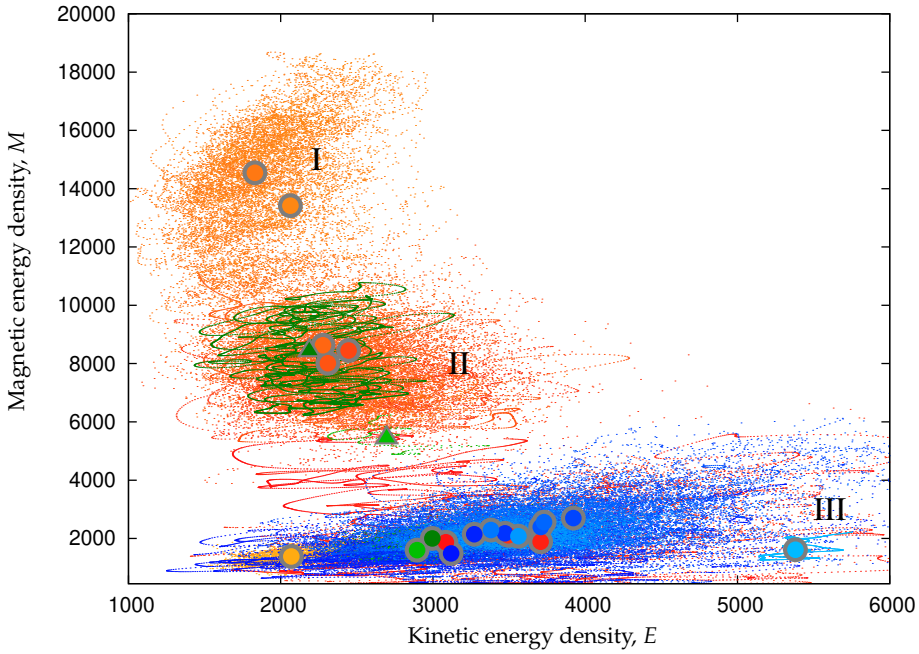

Figure 5.8: A "phase portrait" of magnetic vs. kinetic energy density values for dynamos with $R = 3.8 \times R_c$, $\tau = 2 \times 10^4$, $P_r = 0.75$ and $P_m = 1.5$. Dots are instantaneous values; Large markers are time-averaged values. The aspect ratio η increases from darker to lighter colours (blue to orange). Blue dots and points represent dynamos that were started from **FD** initial conditions. Warm colours and greens represent simulations that were started as from **MD** initial conditions. Green symbols and dots represent simulations that were started as from **MD** initial conditions at $\eta = 0.6$ and $\eta = 0.7$ and that were repeated starting from a higher magnetic energy and lower kinetic energy (triangles) relatively to the original simulations (circles).

gion. Another observation is that **FD** dynamos exhibit decreasing dipolarity as the aspect ratio increases, which corresponds to a decrease in shell thickness. On the other hand, **MD** dynamos show little variation in dipolarity with aspect ratio but can still be categorized into two groups: one for thin shells and another for thick shells. Therefore, it's evident that thinner shells result in dynamos that are more dipole-dominated. Additionally, panel (b) of Figure 5.7 shows that the Nusselt number Nu_i, which measures the efficiency of convective heat transport, decreases steadily as η increases. This trend can be explained by considering the effects of shell geometry on convective processes. As η increases (i.e., as the shell becomes thinner), the available space for convective motions is reduced, which restricts the development of large convective cells.

Consequently, the convective heat transport efficiency diminishes, leading to a decrease in Nu_i. This behavior is expected for a similar $\mathrm{Ra}/\mathrm{Ra}_c$ ratio, as the thinner shell geometry limits the extent of heat transfer, even though the system remains convectively unstable. Thus, the decrease in Nu_i with increasing η reflects the reduced convective vigor in thinner shells.

It is intriguing to observe a distinct division between **MD** and **FD** dynamos in energy density space, as illustrated in Figure 5.8. This figure compiles plots of magnetic energy density as a function of kinetic energy density, highlighting the relationship between the two types of dynamos.

Three distinct regions emerge, corresponding to simulations culminating in **MD** dynamos with varying degrees of dipole stability (regions I and II in Figure 5.8), and simulations concluding as **FD** dynamos (region III). In regions I and II, the **MD** solutions differ in the ratio between the steady and fluctuating parts of the dipole field, with some showing stronger steady dipoles (region I) and others with more fluctuating components (region II). It is clear that the dipolar structure is maintained in most cases, as indicated by the warm-colored dots and circles predominantly found in regions I and II, while all blue dots and symbols are located in region III. An exception occurs when the magnetic energy density of the initial **MD** condition is insufficient, or its ratio to kinetic energy density is small (green circles). In such cases, the solutions transition to an **FD** state and remain there. Conversely, if the initial **MD** condition experiences a sufficient increase in magnetic energy density, the solution persists as an **MD** dynamo (green dots and triangles).

5.6 The cross-helicity effect

To incorporate the influence of turbulence on dynamo behavior, we employ a technique called scale separation. This method is justified by the coexistence of enduring large-scale structures (such as Earth's dipolar field) and intricate turbulent motions at smaller scales in dynamo systems. In this approach, we decompose the velocity field $\mathbf{u}$ and the magnetic field $\mathbf{b}$ into their large-scale components ($\mathbf{U}$ and $\mathbf{B}$) and their fluctuating components ($\mathbf{u}'$ and $\mathbf{b}'$), respectively:

$$\mathbf{u} = \mathbf{U} + \mathbf{u}', \tag{5.6}$$

$$\mathbf{b} = \mathbf{B} + \mathbf{b}'. \tag{5.7}$$

Here, capital letters denote the large-scale components, termed as "mean" components throughout this discussion. As described in the literature [122, 226, 16], there are several ways to perform this scale separation. We carry out this separation by assuming that the steady large-scale components of the flow and magnetic field correspond to their respective time-averaged zonal components. The mean flow $\mathbf{U}$ is then expressed as:

$$\mathbf{U} = \langle \mathbf{u} \rangle = \frac{1}{2\pi\tau} \iint \mathbf{u} \, \mathrm{d}\varphi \, \mathrm{d}t, \tag{5.8}$$

where τ represents a suitable time scale. A similar expression can be formulated for the mean magnetic field. While this separation of scales could theoretically be applied to all main dynamical variables and model equations, in our study, we focus solely on the induction equation to evaluate the impact of turbulent transport on magnetic field generation through dynamo action. When we apply the scale separation technique to the induction equation:

$$\partial_t \mathbf{b} = \nabla \times (\mathbf{u} \times \mathbf{b}) + \lambda \nabla^2 \mathbf{b}, \tag{5.9}$$

where λ denotes the magnetic diffusivity, we obtain the induction equation for the mean magnetic field:

$$\partial_t \mathbf{B} = \nabla \times (\mathbf{U} \times \mathbf{B}) + \nabla \times \mathbf{E}_\mathrm{M} + \lambda \nabla^2 \mathbf{B}, \tag{5.10}$$

where the turbulent electromotive force, $\mathbf{E}_\mathrm{M}$, is defined as:

$$\mathbf{E}_\mathrm{M} = \langle \mathbf{u}' \times \mathbf{b}' \rangle. \tag{5.11}$$

By employing the two-scale direct-interaction approximation (TSDIA) of inhomogeneous magnetohydrodynamic (MHD) turbulence, we express the turbulent electromotive force (see [228] and references therein), in terms of mean variables, as:

$$\mathbf{E}_\mathrm{M} = \alpha \mathbf{B} - \beta \mathbf{J} + \gamma \mathbf{\Omega}. \tag{5.12}$$

Here, $\mathbf{J} = \nabla \times \mathbf{B}$ and $\mathbf{\Omega} = \nabla \times \mathbf{U}$. The coefficients α, β, and γ can be expressed in terms of the turbulent residual helicity, $H = \langle \mathbf{b}' \cdot \mathbf{j}' - \mathbf{u}' \cdot \boldsymbol{\omega}' \rangle$, the turbulent MHD energy, $K = \langle \mathbf{u}'^2 + \mathbf{b}'^2 \rangle / 2$, and the turbulent cross-helicity $W = \langle \mathbf{u}' \cdot \mathbf{b}' \rangle$, respectively [122, 231]. Following [226], they are modelled as

$$\alpha = C_\alpha \tilde{\tau} \langle \mathbf{b}' \cdot \mathbf{j}' - \mathbf{u}' \cdot \boldsymbol{\omega}' \rangle = C_\alpha \tilde{\tau} H, \tag{5.13a}$$

$$\beta = C_\beta \tilde{\tau} \langle \mathbf{u}'^2 + \mathbf{b}'^2 \rangle = C_\beta \tilde{\tau} K, \tag{5.13b}$$

$$\gamma = C_\gamma \tilde{\tau} \langle \mathbf{u}' \cdot \mathbf{b}' \rangle = C_\gamma \tilde{\tau} W, \tag{5.13c}$$

where C_α, C_β, and C_γ are model constants, and $\tilde{\tau}$ is the characteristic time of turbulence, typically expressed as:

$$\tilde{\tau} = K / \varepsilon, \tag{5.14}$$

with the dissipation rate of the turbulent MHD energy, ε, defined by:

$$\varepsilon = \nu \left\langle \frac{\partial u'_a}{\partial x_b} \frac{\partial u'_a}{\partial x_b} \right\rangle + \lambda \left\langle \frac{\partial b'_a}{\partial x_b} \frac{\partial b'_a}{\partial x_b} \right\rangle. \tag{5.15}$$

The coefficients α, β, and γ in the expression for the turbulent electromotive force can be derived from a more general tensorial formulation. However, for practical applications in modeling turbulent magnetohydrodynamics, these coefficients are expressed as scalars. This simplification is justified as it captures the essential mean-field effects of turbulent interactions while facilitating mathematical treatment and numerical simulations. The scalar representation assumes isotropy in the turbulence, allowing us to avoid the complexities associated with tensorial forms. Furthermore, this approach aligns with empirical observations, making it a widely accepted method in the study of turbulent electromotive forces in MHD systems [18].

Substituting (5.12) into the mean induction equation (5.10), we obtain:

$$\partial_t \mathbf{B} = \nabla \times (\mathbf{U} \times \mathbf{B}) + \nabla \times (\alpha \mathbf{B} + \gamma \boldsymbol{\Omega}) - \nabla \times [(\lambda + \beta) \nabla \times \mathbf{B}] \,. \tag{5.16}$$

Thus, in addition to the transport enhancement or structure destruction due to turbulence through the enhanced diffusion $(\lambda + \beta)$, there is also transport suppression or structure formation due to turbulence represented by the helicities α and γ [227]. In the classical mean field theory of dynamos [122, 149], the turbulent electromotive force is composed of the first two terms on the right-hand side of equation (5.12), namely $\alpha \mathbf{B} - \beta \mathbf{J}$. Dynamos resulting from this model are known as "alpha dynamos", where the turbulent diffusion is balanced by an α-effect. The properties of these terms have been discussed widely in the literature, and so we do not repeat this discussion here. Instead, let us now consider the final term on the right-hand side of equation (5.12), $\gamma \boldsymbol{\Omega}$. Unlike the other terms describing the electromotive force, the mean variable in this term depends on the mean velocity and not the mean magnetic field. [226] describes how a fluid element subject to a Coriolis-like force (a mean vorticity field) can contribute to the turbulent electromotive force through γ, a measure of the turbulent cross helicity. Dynamos in which the main balance is between $-\beta \mathbf{J}$ and $\gamma \boldsymbol{\Omega}$ are known as "cross-helicity dynamos", where the cross-helicity term replaces the α-effect term in balancing the turbulent diffusion. Cross-helicity

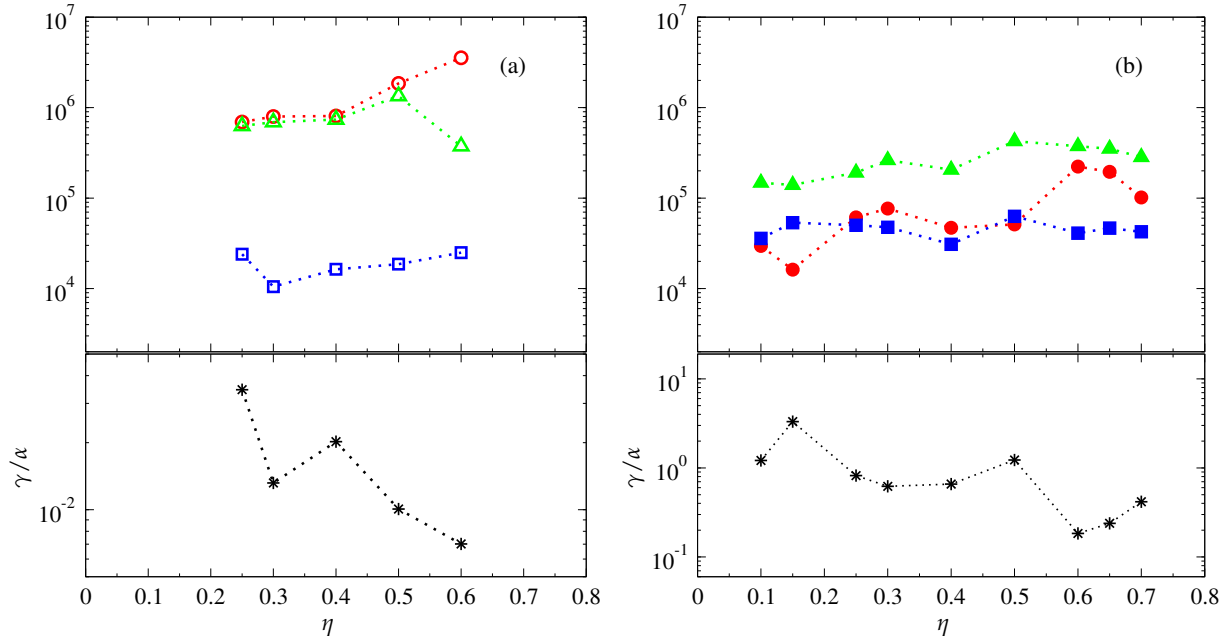

Figure 5.9: Magnitude of α–, β–, and γ–effects with increasing shell thickness aspect ratio η for dynamo solutions with $R = 3.8 \times R_c$, $\tau = 2 \times 10^4$, $P_r = 0.75$ and $P_m = 1.5$. The upper panels show root-mean squared time-averaged values of the α–effect (red circles), β–effect (green triangles up) and γ–effect (blue squares). It is important to note that α represents the scalar value of the α effect, β represents the scalar β effect, and γ represents the scalar γ effect, not the average magnitudes of $|\alpha||\mathbf{B}|$, $|\beta||\mathbf{J}|$, or $|\gamma||\mathbf{\Omega}|$. The lower panels show the ratio of γ– to α–effects. Column (a) contains **MD** dynamo solutions (empty symbols) while column (b) contains **FD** dynamo solutions (full symbols) as shown in Figure 5.7.

dynamos have been studied much less than α dynamos, and this study represents an initial step in addressing this potentially important imbalance. In particular in Figure 5.9, we calculate all three contributions to the turbulent electromotive force in our dynamo simulations in order to determine their relative importance. These results are discussed below.

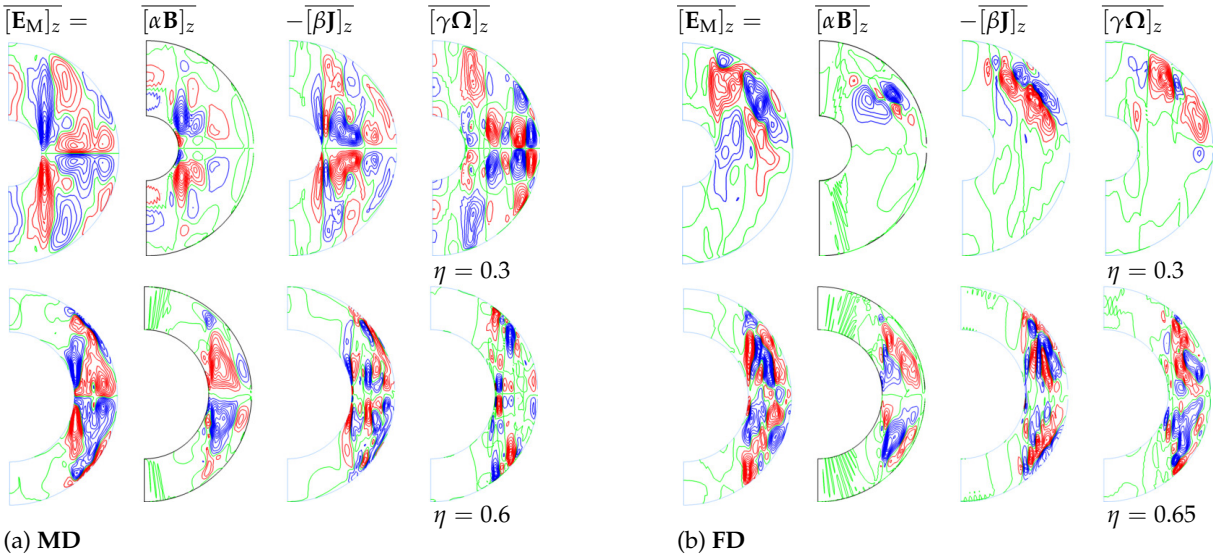

(a) **MD** (b) **FD**

Figure 5.10: Spacial structures of the azimuthally-averaged z-component of the electromotive force $\mathbf{E}_\mathrm{M}$ and its α–, β– and γ–effect constituents as given by Equation (5.12). Four dipolar dynamo solutions are plotted as follows. (a) **MD** dynamo solutions with $\eta = 0.3$, $P_r = 0.75$, $\tau = 2\times10^4$, $R = 2500000$, $P_m = 1.5$ (top row) and $\eta = 0.6$, $P_r = 0.75$, $\tau = 2\times10^4$, $R = 410000$, $P_m = 1.5$ (bottom row). (b) **FD** dynamo solutions with $\eta = 0.3$, $P_r = 0.75$, $\tau = 2\times10^4$, $R = 2500000$, $P_m = 1.5$ (top row) and $\eta = 0.65$, $P_r = 0.75$, $\tau = 2\times10^4$, $R = 300000$, $P_m = 1.5$ (bottom row). In each column contour lines of the quantities denoted at the column heading are plotted with positive contours shown in red, negative contours shown in blue, and the zeroth contour shown in green. **Note on Magnitudes:** The components of the electromotive force are evaluated as $\alpha|\mathbf{B}|$, $\beta|\mathbf{J}|$, and $\gamma|\mathbf{\Omega}|$. It is important to assess their relative contributions to the overall electromotive force, as this influences the dynamo action in both the **MD** and **FD** cases. In particular, the α effect is expected to be stronger in the **MD** case due to the antisymmetry about the equator, while the γ effect's contribution becomes more comparable in the **FD** case due to its more complex spatial structure.

5.7 Characteristics and significance of cross-helicity

The variation of the turbulent transport coefficients α, β, and γ as a function of shell thickness is displayed in Figure 5.9. For simplicity, in this initial investigation, we take $C_A\tilde{\tau} = 1$, where $A = \alpha$, β, or γ. Thus, the three effects are represented by the turbulent residual helicity H, the turbulent MHD energy K, and the turbulent cross-helicity W, respectively.

For **MD** dynamo solutions, there is a clear disparity between the α- and β-effects, and the γ-effect. The γ-effect is, for the range of η considered, about two orders of magnitude smaller than the other effects. Thus, across a wide range of shell thickness aspect ratios, **MD** dynamos can be considered to be operating predominantly as α dynamos.

In contrast, for **FD** dynamo solutions, a different picture emerges. Across the range of η considered, the α- and γ-effects are of a similar magnitude. Thus, both these effects are potentially important in balancing the β-effect. Therefore, **FD** dynamo solutions represent a "mixture" of an α dynamo and a cross-helicity dynamo.

Figure 5.10 displays z-projections of the azimuthally-averaged components of the electromotive force. For the **MD** dynamo solutions, shown in (a), the γ-effect follows an antisymmetric pattern about the equator, just like the other effects. This behavior is expected from the pseudoscalar nature of γ and the symmetry of magnetic fields in **MD** dynamos [226]. For **FD** dynamo solutions, such as those displayed in (b), the components of the electromotive force no longer exhibit antisymmetry about the equator. This behavior is, in part, due to the more complex spatial structure of the magnetic fields of **FD** dynamos compared to **MD** dynamos. This feature, combined with generally weaker magnetic field strengths and different flow profiles (see Figures 5.5 and 5.6, for example), results in the α-effect being weaker for **FD** dynamos. Thus, both the α- and γ-effects become of comparable importance in sustaining dynamo action.

5.8 Concluding remarks

In the realms of celestial bodies, rotating thermal convection plays a fundamental role in shaping their interiors and atmospheres. Within these fluid regions, comprising plasmas or metallic components, intense convection drives large-scale electric currents, giving rise to the characteristic self-sustained magnetic fields of these cosmic objects. This study delves into the comparative significance of two primary mechanisms for magnetic field generation and amplification: the helicity- and cross-helicity effects of mean-field dynamo theory. We aim to investigate whether the turbulent helicity effect, or the α-effect, holds greater importance in the geodynamo, while the cross-helicity effect, or the γ-effect, is more pronounced in the solar global dynamo. This hypothesis stems from differences in the shell aspect ratios between the solar convection zone and Earth's inner core. Here are the key findings presented in this study (i) Critical parameter values determining the onset of convection have been numerically determined as functions of the shell radius ratio, η; (ii) Bistability and the coexistence of two distinct dynamo attractors have been identified as functions of the shell radius ratio, η; (iii) Spatial distributions and time-averaged values of turbulent helicity and cross-helicity electromotive force (EMF) effects have been analyzed for both types of dynamo attractors, and as functions of the shell radius ratio, η.

To explore the α- and γ- electromotive effects, we conducted an extensive suite of over 40 direct numerical simulations of self-sustained dynamo action driven by thermal convection in rotating spherical fluid shells. These simulations varied the shell thickness aspect ratio η and critical Rayleigh number while keeping other parameters constant. Our simulations are grounded in the Boussinesq approximation of the governing nonlinear magnetohydrodynamic equations, incorporating stress-free velocity boundary conditions. While employing fully compressible equations would be ideal, it's not practical for global dynamo simulations due to the short sound wave periods compared to the convective turnover time and magnetic diffusion timescales of primary interest.

In this work, we opt for the Boussinesq approximation to ensure consistency across various shell radius ratios and to isolate the effects of shell thickness from the complexities introduced by density stratification. This approach allows us to focus specifically on how changes in shell thickness impact dynamo behavior. In previous studies [197, 198], distinct chaotic dynamo states have been observed to coexist within certain ranges of governing parameters. Here, we extend this finding by demonstrating that two fundamentally different nonlinear dynamo attractors coexist over an extensive range of shell thickness aspect ratios $\eta \in [0.25, 0.6]$.

This result holds particular significance because it corresponds precisely to the range of values where most celestial dynamos operate. It suggests that the morphologies of magnetic fields may depend on the initial state of the dynamo. We delve deeper into this observation, examining the contrasting properties characterizing the coexisting dynamo regimes, namely, mean-field dipolar (**MD**) dynamos and fluctuating dipolar (**FD**) dynamos. We analyze differences in their temporal behavior and spatial structures, both in terms of the magnetic field and the rotating thermal convection. Our investigation reveals that the relative importance of the electromotive dynamo effects differs between mean-field dipolar and fluctuating dipolar dynamos. In fluctuating dipolar dynamos, the helicity α-effect and the cross-helicity γ-effect exhibit comparable intensities, with their ratio remaining relatively constant across varying shell thickness. Conversely, in mean-field dipolar dynamos, the helicity α-effect dominates by approximately two orders of magnitude, becoming even more pronounced with decreasing shell thickness.

These results suggest that both dynamo mechanisms play crucial roles in the generation of the solar global magnetic field, given that the solar dynamo belongs to the fluctuating dipolar type. Moreover, our findings indicate that the cross-helicity effect may be significant in understanding dynamo mechanisms in stellar dynamos, which may also exhibit a fluctuating dipolar type. This stands in contrast to the solar dynamo, which features dominant large-scale magnetic structures in only one hemisphere [133]. Conversely, since the geodynamo is of a mean-field dipolar type, the helicity effect appears to be more significant in this case, a trend that is expected to

strengthen as the inner solid core grows due to iron freezing. Recent simulations of the geodynamo, considering the nucleation and growth of the inner core, have provided valuable insights. Authors such as [59] and [124] observed that pre-inner core nucleation dynamos exhibit weak thermal convection, low magnetic intensity, and non-dipolar field morphology. However, as the inner core nucleates and grows, the solutions transition to stronger axial dipole morphology. Our findings indicate that multipolar dynamos emerge when the shell radius ratio η is below 0.25. Unlike fluctuating dipolar **FD** dynamos, which primarily exhibit a stable dipole structure with variations in field strength, multipolar dynamos feature multiple regions of opposite magnetic polarity. This leads to a complex magnetic field with several poles, resulting in intricate spatial patterns and significant variations in both field strength and orientation throughout the domain. While both dynamo types can coexist within the same parameter regime, the distinction lies in their magnetic field morphology and stability: multipolar solutions generate a more chaotic and diverse field structure, whereas **FD** dynamos maintain a dominant dipole configuration with temporal fluctuations. Interestingly, our **FD** solutions feature vigorous convection, though with lower magnetic field intensity compared to corresponding **MD** dynamos. The higher magnetic field intensity observed in the **MD** regime may be linked to the strong-field branch described by Dormy [152] , where the magnetic field plays a dominant role in governing flow dynamics, leading to a more coherent and stable dynamo.

Moving forward, it would be valuable to revisit the analysis of helicity and cross-helicity effects using the more general anelastic approximation of the governing equations. Additionally, numerous questions remain unanswered regarding how the dynamic balance between the components of the electromotive force influences various aspects of dynamo action, including the mechanisms underlying the transition between **MD** and **FD** dynamos. These avenues of research hold promise for further advancing our understanding of geodynamo and other celestial dynamo systems.

Chapter 6

A study of global magnetic helicity in self-consistent spherical dynamos

The results presented in this chapter have been published in [91]. This chapter follows the published paper and includes figures from the paper with the agreement of all authors.

6.1 Introduction

Magnetic helicity, a fundamental aspect of both ideal and resistive magnetohydrodynamics, serves as a crucial constraint in understanding the behavior of global magnetic fields within celestial bodies like the Sun and other stars. The measurement and analysis of magnetic helicity density provide valuable insights into the internal dynamics of the dynamos responsible for generating these magnetic fields. In this thesis chapter, we delve into a comprehensive study focusing on the global relative magnetic helicity within self-consistent spherical dynamo solutions of increasing complexity.

The interplay between the poloidal and toroidal magnetic fields, quantified by magnetic helicity, underscores the intricate nature of magnetic field dynamics. Our investigation reveals distinct states of linkage between these fields, suggesting the existence of preferred configurations. This suggests that global magnetic reversals may play a role in maintaining this linkage. If only the poloidal or toroidal field reverses, the preferred state of linkage is lost.

Moreover, our analysis indicates that changes in magnetic helicity can act as early indicators of magnetic reversals, providing a potential method for predicting these events. Notably, the signatures of these reversals may be observable at the outer surface of celestial bodies, providing crucial insights into their internal magnetic dynamics. Through our research, we aim to contribute to a deeper understanding of the mechanisms underlying global magnetic field generation and evolution, shedding light on the intriguing phenomenon of magnetic reversals and their implications for celestial bodies' magnetic behavior. The concept of magnetic helicity stands as a cornerstone in the realm of ideal magnetohydrodynamics (MHD), serving as an invariant that characterizes field line topology weighted by magnetic flux [150, 10]. Its significance spans across diverse domains, from laboratory plasma physics [208] to the study of astrophysical phenomena [165, 132], owing to its near-conservation in the weakly resistive regime [8, 66, 67]. While magnetic helicity has been extensively scrutinized within mean field dynamo models [18, 40, 16], its exploration in the context of self-consistent convection-driven dynamos within spherical shells remains relatively scarce. This scarcity can be attributed to the challenges posed by the scales typically considered in global simulations, where attaining the requisite high magnetic Reynolds number to maintain a nearly constant global magnetic helicity value is often unfeasible. However, despite these limitations, the utility of magnetic helicity in elucidating the nature of self-consistent spherical dynamos cannot be overlooked. Rather than delving into its role in turbulence, such as its influence on the α-effect in mean-field models, this study directs

its focus towards discerning what insights can be gleaned from the global magnetic helicity regarding the topological intricacies of the magnetic field. Specifically, we aim to unravel how the toroidal and poloidal fields interlink and how variations in this linkage manifest, particularly at the outer surface—a phenomenon of particular relevance for observational studies of stars.

Building upon these insights, recent observational studies have begun to explore the implications of global magnetic helicity in celestial bodies beyond the Sun. For instance, investigations [166, 97, 168] into solar activity cycles have revealed promising correlations between helicity flux during solar minima and subsequent solar maxima, presenting a potential improvement over predictions solely based on the polar magnetic field [97]. These helicity measurements primarily focus on current helicity ($\mathbf{J} \cdot \mathbf{B}$), as direct observations often rely on the local twist of the magnetic field lines associated with electric currents in the solar atmosphere. While magnetic helicity ($\mathbf{A} \cdot \mathbf{B}$)—which accounts for the global topology of magnetic fields—would provide more comprehensive insights, its measurement requires knowledge of the vector potential $\mathbf{A}$, which is not directly observable. As a result, certain assumptions or models are needed to estimate the global helicity from surface measurements. Observational measures of helicity are typically based on the magnetic field components derived from solar vector magnetograms, which provide the surface magnetic field $\mathbf{B}$ and allow for estimation of the current density $\mathbf{J}$. Notably, the asymmetry of helicity flux measurements between hemispheres has emerged as a significant factor, hinting at the importance of equatorial symmetry in helicity density at the solar surface. Extending beyond the solar domain, efforts to measure magnetic helicity in other stars have also gained traction [130, 129]. Although limited to surface measurements and constrained by resolution, these studies have uncovered scaling laws linking the strength of surface helicity density to that of the toroidal field [129]. Intriguingly, findings suggest variations in field topology across different evolutionary stages of stars, hinting at the potential utility of

magnetic helicity density, alongside complementary observables, in characterizing stellar evolution and dynamo processes. Such endeavors pave the way for a deeper understanding of the role of magnetic helicity in shaping the magnetic behavior of celestial bodies throughout their evolutionary trajectories.

The primary objective of this study is to delve into the behavior of global magnetic helicity within different types of self-consistent convective dynamos operating within spherical shells. Unlike endeavors aimed at modelling specific celestial bodies like the Sun or particular stars or planets, our focus lies in conducting a broad-spectrum analysis of typical solutions derived from a well-established model for spherical dynamos [193, 39]. These solutions, chosen to encompass various known dynamo regimes, serve as representatives of the diverse dynamical behaviors exhibited in such systems. The three specific solutions under scrutiny are selected to progressively increase in complexity, thereby enabling a comprehensive assessment of the efficacy of magnetic helicity as both a predictive and analytical tool. By subjecting these solutions to scrutiny, we aim to elucidate the utility of magnetic helicity in navigating the intricacies posed by increasingly chaotic spatial and temporal flow and field structures within self-consistent convective dynamos. This pilot investigation sets the stage for a deeper understanding of the role played by magnetic helicity in shaping the dynamics of spherical dynamos across a spectrum of complexities.

Contents. Next, we outline the main equations of our model and provide an overview of the numerical method employed. Subsequently, we offer a simple explanation of magnetic helicity within spherical shells. Each dynamo solution is then individually examined, emphasizing the insights gleaned from magnetic helicity. Finally, we conclude with a summary of our findings and a discussion on their implications.

6.2 Mathematical model

Following the established model of convection-driven spherical dynamo action [32, 195, 196], we consider a spherical shell rotating with constant angular velocity Ω. The static temperature distribution, along with the associated parameters and definitions, is provided in Chapter 3. In this model, the magnetohydrodynamics (MHD) equations are solved under the Boussinesq approximation. The non-dimensional parameters (such as the internal and external Rayleigh numbers R_i, R_e, Coriolis number τ, Prandtl number P_r, and magnetic Prandtl number P_m) and the boundary conditions (no-slip, stress-free, and electrically insulating) are also detailed in Chapter 3. This chapter includes all necessary equations and conditions for velocity and magnetic field boundary specifications. Refer to Chapter 4 for a discussion on the numerical methods used for their solution. The calculations performed in this work have been run with resolutions $(n_r, n_\theta, n_\phi) = (33, 64, 129)$ and $(n_r, n_\theta, n_\phi) = (41, 96, 193)$. Azimuthally averaged components of the fields v, w, h, and g will be indicated by an overbar.

6.2.1 Magnetic helicity

Magnetic helicity serves as a crucial concept in magnetohydrodynamics (MHD), capturing the intricate topology of magnetic fields. Within self-consistent spherical dynamos, the magnetic field arises from and is sustained by convective thermal motions within a spherical shell [38]. Extending beyond this shell, in the absence of ongoing fluid motion, the magnetic field transitions into a freely decaying potential field.

Due to the open nature of the magnetic field, classical helicity [221, 150] is replaced by relative magnetic helicity [10]. [9] demonstrated that within the spherical shell volume V, relative helicity H takes a particularly elegant form:

$$H = 2\int_V \boldsymbol{L}h\cdot\boldsymbol{L}g\,\mathrm{d}V = 2\int_V (\mathrm{curl}^{-1}\boldsymbol{B}_P)\cdot\boldsymbol{B}_T\,\mathrm{d}V, \tag{6.1}$$

where $\mathbf{L} = -\mathbf{r}\times\boldsymbol{\nabla}$. This representation illustrates the global interconnection between the poloidal and toroidal magnetic fields [11]. Although both fields occupy the same spatial region, this formulation provides a generalized concept of linkage, crucial for subsequent analysis.

Expressing $\mathbf{B}_T$ as $\mathbf{L}g$ via simple vector algebra simplifies the equation. However, relating $\mathbf{B}_P$ to $\mathbf{L}h$ isn't as straightforward. In spherical coordinates, the latter can be defined as:

$$\boldsymbol{L}h = \left(0, \frac{1}{\sin\theta}\frac{\partial h}{\partial\phi}, -\frac{\partial h}{\partial\theta}\right). \tag{6.2}$$

The following section outlines a verification test designed to ensure the accurate implementation of the helicity equation in the code.

6.3 Verification test for helicity equation implementation

In order to verify the correct implementation of the helicity formula in the code, the following test was performed. In a magnetically closed spherical shell, linear force-free solutions exist where

$$\boldsymbol{\nabla}\times\boldsymbol{B} = \lambda\boldsymbol{B}, \tag{6.3}$$

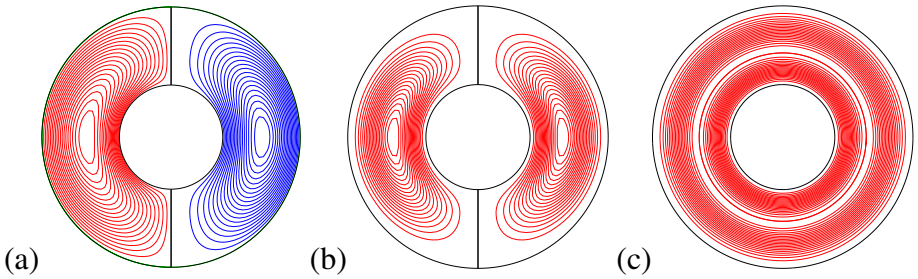

Figure 6.1: (a) shows meridional lines of constant $\overline{B}_\phi$ (left half) and $r\sin\theta\partial_\theta\overline{h}$ (right half); (b) shows averaged helicity density (left half) and unaveraged helicity density at $\phi = 30^\circ$ (right half); (c) shows the helicity density in the equatorial plane.

with constant λ. The values of λ that satisfy equation (6.3) in the given domain form a discrete spectrum of eigenvalues for the curl operator. The corresponding eigenfunction of each eigenvalue has the form (in spherical coordinates)

$$B_r = \frac{1}{r^{3/2}}\left[c_1 J_{3/2}(\lambda r) + c_2 Y_{3/2}(\lambda r)\right]\cos\theta, \tag{6.4a}$$

$$\begin{aligned} B_\theta = &-\frac{1}{2\lambda^{3/2}r^3}\left\{\sin(\pi-\lambda r)\left[c_1\left(\sqrt{\frac{2}{\pi}}\lambda^2 r^2 - \sqrt{\frac{2}{\pi}}\right) + \sqrt{\frac{2}{\pi}}c_2\lambda r\right]\right. \\ &\left. + \cos(\pi-\lambda r)\left[c_2\left(\sqrt{\frac{2}{\pi}}\lambda^2 r^2 - \sqrt{\frac{2}{\pi}}\right) - \sqrt{\frac{2}{\pi}}c_1\lambda r\right]\right\}\sin\theta, \end{aligned} \tag{6.4b}$$

$$B_\phi = \frac{\lambda}{2\sqrt{r}}\left[c_1 J_{3/2}(\lambda r) + c_2 Y_{3/2}(\lambda r)\right]\sin\theta, \tag{6.4c}$$

where $J_{3/2}(x)$ and $Y_{3/2}(x)$ are Bessel functions of the first and second kind, respectively, and c_1 and c_2 are constants determined from the boundary conditions [41].

For a closed magnetic field, we have $B_r = 0$ on the inner and outer boundaries of the spherical shell. The two conditions can be written as the matrix-vector system

$$\begin{bmatrix} J_{3/2}(\lambda r_i) & Y_{3/2}(\lambda r_i) \\ J_{3/2}(\lambda r_o) & Y_{3/2}(\lambda r_o) \end{bmatrix}\begin{bmatrix} c_1 \\ c_2 \end{bmatrix} = \begin{bmatrix} 0 \\ 0 \end{bmatrix}. \tag{6.5}$$

For a non-trivial solution, we require that

$$J_{3/2}(\lambda r_i)Y_{3/2}(\lambda r_o) - Y_{3/2}(\lambda r_i)J_{3/2}(\lambda r_o) = 0, \tag{6.6}$$

and we consider the smallest values of λ satisfying equation (6.6) because it often corresponds to the most stable configuration of the system. . With λ found, c_1 and c_2 are readily determined. For $r_i = 2/3$ and $r_o = 5/3$, $\lambda \approx 3.383384$. The choice $c_1 = 1$ serves as a normalization that simplifies the calculations, and $c_2 \approx 1.974996$.

It is important to note that equation (6.3) admits multiple solutions, as it is a linear equation. These solutions correspond to different eigenmodes of the curl operator, each characterized by distinct spatial structures. The specific solution presented in this test case, with a large-scale dependence on θ, represents the fundamental mode, corresponding to the lowest eigenvalue λ. However, higher-order modes with more complex angular and radial dependencies also satisfy equation (6.3). These modes can arise in different physical scenarios and boundary conditions. The current test focuses on the fundamental mode because it often corresponds to the most stable configuration and provides a straightforward test of the helicity formula implementation. Nevertheless, acknowledging the existence of these higher-order modes is crucial, as they represent other valid solutions that could influence magnetic configurations in more complex systems.

Since this particular magnetic field is force-free, it satisfies $g = \lambda h$ due to the linear dependence between the poloidal component g and the toroidal component h of the magnetic field. This condition ensures that the magnetic field remains stable and self-consistent, with the constant acting as a scaling factor that relates the strength of the poloidal field to the toroidal field. The equation reflects the fundamental nature of the magnetic field in such configurations, demonstrating how the two components interact to maintain a force-free state. Using this property, the

magnetic helicity can be written as

$$H = 2\lambda \int_V |\boldsymbol{L}h|^2 \, \mathrm{d}V = \frac{2}{\lambda} \int_V |\boldsymbol{L}g|^2 \, \mathrm{d}V. \tag{6.7}$$

For this force-free field, the above relations represent an alternative way to calculate H compared to the general equation (6.1), and provide a useful test that the general formula has been coded correctly. For the values used in this work, we find, for the above force-free solution, that $H \approx 6.91$ using either of equations (6.1) and (6.7).

In Figure 6.1(b), the meridional plot of the azimuthal average of the helicity density is equal to that of a specific slice (shown on the right-hand side). This is because the magnetic field is symmetric and, also, not dependent on ϕ in this example. However, this result is connected to a more general one regarding the magnetic helicity of any magnetic field in a spherical shell. That is,

$$\int_0^{2\pi} \boldsymbol{L}h \cdot \boldsymbol{e}_\theta \, \mathrm{d}\phi = \int_0^{2\pi} \boldsymbol{L}g \cdot \boldsymbol{e}_\theta \, \mathrm{d}\phi = 0, \tag{6.8}$$

for given values of r and θ. The proof of this result can be most easily seen by expanding the integrands in terms of their spectral decompositions, e.g.

$$\boldsymbol{L}h \cdot \boldsymbol{e}_\theta = \sum_{l=0}^{\infty} \sum_{m=-l}^{l} \frac{\mathrm{i}m}{\sin\theta} H_l^m(r,t) P_l^m(\cos\theta) \mathrm{e}^{\mathrm{i}m\phi}.$$

The azimuthal average is found by setting $m = 0$, hence confirming (6.8). Thus, plots of the azimuthal average of the helicity density depend only on $(\boldsymbol{L}h \cdot \boldsymbol{e}_\phi)(\boldsymbol{L}g \cdot \boldsymbol{e}_\phi)$. This constraint is another way to check that magnetic helicity has been calculated correctly in the code.

	Case 1: Steady dynamo	Case 2: Quasi-periodically reversing dynamo	Case 3: Aperiodically-reversing dynamo
η	0.35	0.4	0.4
R_i	0	3.5×10^6	8.5×10^5
R_e	10^5	0	0
τ	2000	3×10^4	3×10^4
P_r	1	0.75	0.1
P_m	5	0.65	1
Boundary conditions	no-slip, fixed temperatures, insulating outer space	stress-free, fixed temperatures, insulating outer space	stress-free, fixed temperatures, insulating outer space

Table 6.1: The three dynamo solutions considered in the study.

6.4 Results: Dynamo solutions

We proceed to examine the behavior of global magnetic helicity across different dynamo solutions. Three cases of escalating complexity are explored, as outlined in Table 6.1.

6.4.1 Case 1: Steady dynamo

We commence with an examination of a laminar dynamo solution, renowned within the community as a benchmark case for validating and testing the accuracy of numerical codes [50, 137]. The non-dimensional parameters and boundary conditions pertinent to this case are detailed in the initial column of Table 6.1.

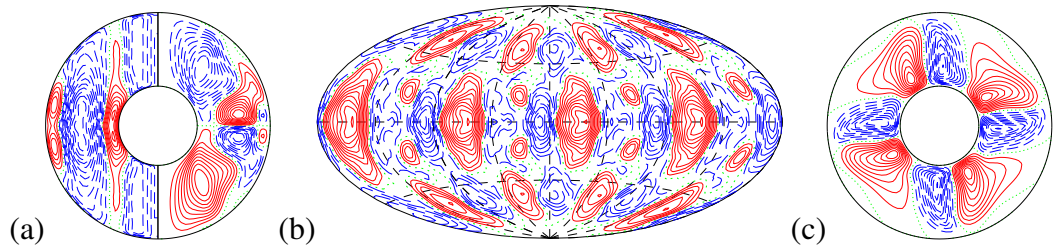

Figure 6.2: Plots of the velocity field for Case 1 at a particular time (this is a steady flow so other times just represent rigid rotations of this solution) (a) shows lines of constant $\overline{u}_\phi$ (left half) and $r\sin\theta\partial_\theta\overline{v}$ (right half) in a meridional plane, visualising the toroidal and poloidal fields respectively; (b) shows lines of constant u_r at $r = r_i + 0.5$. There is a distinct pattern of columnar convection at both the equator and near the poles; and (c) shows lines of constant $r\partial_\phi v$ in the equatorial plane. Blue is negative, red is positive and green is zero in this figure and in all subsequent contour plots.

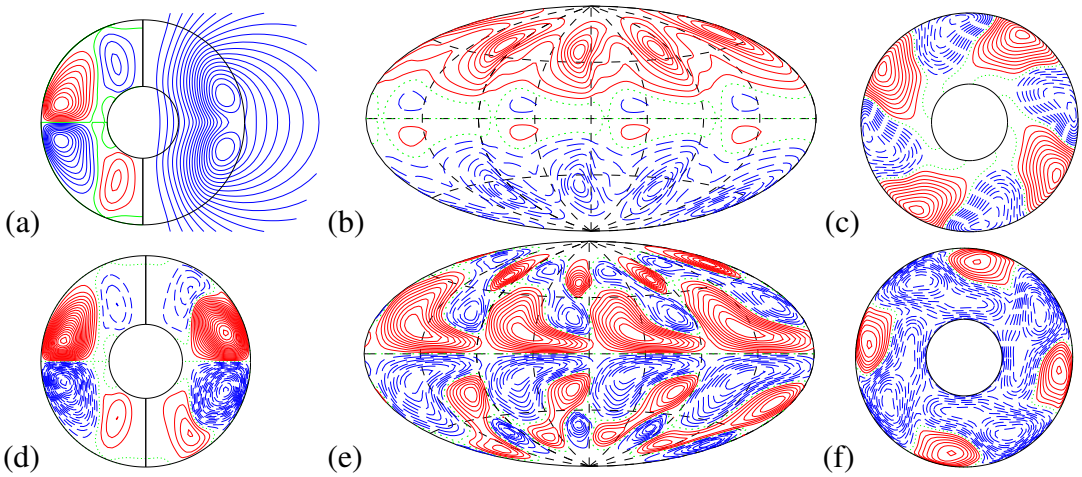

Figure 6.3: Plots of the magnetic field (top row) and magnetic helicity (bottom row) for Case 1 at a particular time. The top panel (a) shows meridional lines of constant $\overline{B}_\phi$ (left half) and $r\sin\theta\partial_\theta\overline{h}$ (right half) visualising the toroidal and poloidal fields respectively; (b) shows lines of constant B_r at $r = r_i + 0.96$; and (c) displays equatorial streamlines, $r\partial_\phi h$ = const. The bottom panel (d) shows contour lines of azimuthally averaged helicity density (left half) and the helicity density in a particular slice $\phi =$ const (right half); (e) shows the helicity density at $r = r_i + 0.96$; and (f) shows the helicity density at the equatorial plane.

A distinctive characteristic of this dynamo is its establishment of a steady-state for both the magnetic and velocity fields. The steady velocity profile showcases columnar convection, depicted in Figure 6.2. Directing our attention to the magnetic field, a global dipole with equatorial inversions manifests. These features, alongside additional details, are depicted in Figure 6.3.

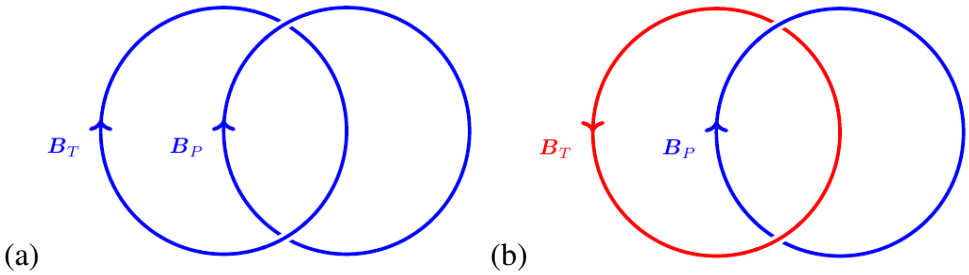

Figure 6.4: A representation of the linkage of toroidal and poloidal fields. Colours correspond to those in figure 6.3(a). The (Gauss) linkage in (a) is -1 and in (b) is $+1$. These signs correspond with those of the helicity density in figure 6.3(d).

In Figure 6.3, the top row provides insights into the magnetic field behavior across distinct planes: (a) the meridional plane, (b) a near-outer spherical surface, and (c) the equatorial plane. The leftmost plot delineates the toroidal and poloidal components of the magnetic field. Notably, these quantities, illustrated in the hemispheres, represent meridional averages. In the left hemisphere, showcasing the large-scale toroidal field behavior, a perfect antisymmetry about the equator is evident. Conversely, in the right hemisphere, depicting the dominant poloidal field behavior, a pronounced dipolar field prevails, albeit with exceptions near the equatorial surface. Here, smaller, relatively weaker positive and negative polarities exist compared to the polar fields, as discerned from the radial magnetic field plot in (b). The radial component exhibits dipolar symmetry, signifying $B_r = 0$ on the equatorial plane. This magnetic profile, maintaining rigid rotation with the sphere, furnishes a lucid basis for interpreting magnetic helicity dynamics.

Descending to the bottom row of Figure 6.3, we encounter contours delineating (d) azimuthally averaged helicity density (left half) and unaveraged helicity density within a specific slice (right half), (e) helicity density at the outer surface, and (f) helicity density within the equatorial plane. Figure 6.3(d) elucidates how helicity density signs across different spherical shell regions hinge upon the linkage of toroidal and poloidal fields. To elucidate the sign conventions of helicity density displayed herein, we schematically outline an idealized toroidal-poloidal field linkage in Figure 6.4. This comprehensive visualization augments our understanding of the intricate interplay between magnetic field components and their resultant helicity dynamics.

In Figure 6.3(a), the left half of the meridional plane illustrates the magnetic field structure, with the Northern Hemisphere (NH) showing a red patch that represents positive toroidal field and the Southern Hemisphere (SH) displaying a blue patch that indicates negative toroidal field. It is important to note that there are also smaller blue and red patches present in the NH and SH, respectively, but the focus here is on the larger structures. The right half of the figure depicts the poloidal field, which is overall negative. This correlates with the helicity densities shown in Figure 6.3(d), where the NH has positive helicity and the SH has negative helicity. In Figure 6.4, the linkage of the toroidal field B_T and poloidal field B_P is illustrated. Plot 6.4 (a) depicts both B_T and B_P in blue and oriented in the same direction, indicating a negative Gauss linking number of -1, which corresponds to the negative helicity density observed in the SH. Conversely, plot 6.4 (b) shows B_T in red and B_P in blue, but oriented in opposite directions, representing a positive Gauss linking number of $+1$. This reflects the positive helicity density in the NH. Overall, the connection between Figures 6.3 and 6.4 highlights how the topological interactions of the toroidal and poloidal fields relate to the helicity structure across different hemispheres, with negative linkage associated with negative helicity in the SH and positive linkage associated with positive helicity in the NH.

Figure 6.3(d) delineates the distribution of helicity density near the surface, presenting a more intricate morphology compared to azimuthal average plots. Nonetheless, a clear predominance of positive helicity density in the north and negative helicity density in the south is evident, maintaining perfect antisymmetry about the equator. This property, coupled with the solution's steadiness, ensures $H = 0$.

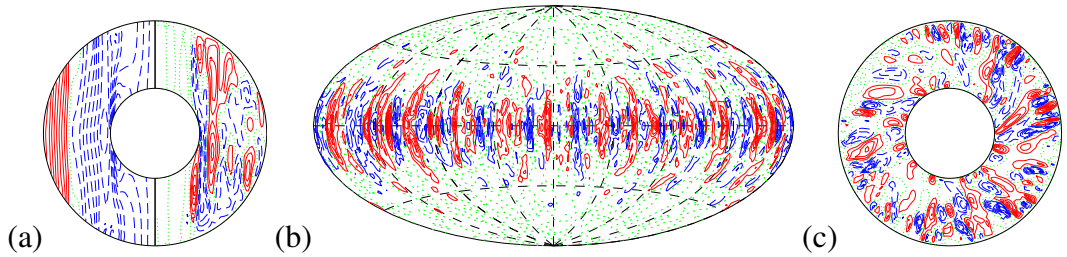

Figure 6.5: Typical structures of the velocity field for Case 2. (a) shows lines of constant $\overline{u}_\phi$ in the left half and streamlines $r\sin\theta\partial_\theta\overline{v}$ = const in the right half, all in the meridional plane; (b) shows lines of constant u_r at $r = r_i + 0.5$; and (c) shows streamlines, $r\partial_\phi v$ = const. in the equatorial plane. These images correspond to the time $t = 5.538$ in the simulation.

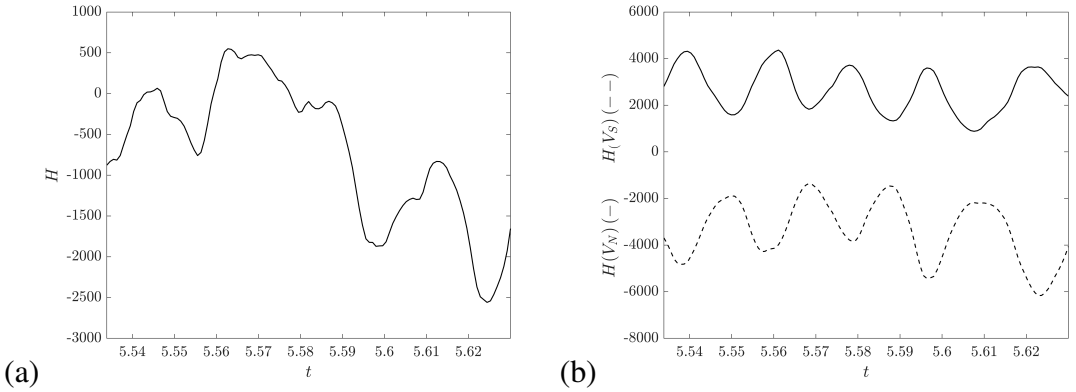

Figure 6.6: Time series of magnetic helicity for Case 2. (a) shows the total helicity as a function of time. (b) shows the helicity density integrated in the northern hemisphere (solid) and the southern hemisphere (dashed).

This straightforward dynamo case serves as a poignant example, illustrating that while the total magnetic helicity equals zero, this result stems from the offsetting of positive and negative large-scale structures. Particularly, the signs of these structures are contingent upon the linkage of poloidal and toroidal fields. However, magnetic helicity isn't solely a measure of linkage; it is also influenced by magnetic flux. This consideration becomes pivotal in comprehending cases exhibiting more irregular temporal behavior and spatial morphology, as discussed subsequently.

6.4.2 Case 2: Quasi-periodically reversing dynamo

Now, we turn our attention to a time-dependent quasi-periodic dynamo solution characterized by regular reversals in the signs of both the poloidal and toroidal components of the magnetic field. The non-dimensional parameters and boundary conditions pertinent to this scenario are outlined in the second column of Table 6.1.

Figure 6.5 illustrates the typical structure of the velocity field. While columnar convection akin to Case 1 persists, the velocity now undergoes chaotic temporal evolution, showcasing much smaller-scale structures.

In contrast to Case 1, where the field structure remained steady over time, rendering the interpretation of helicity density in terms of linkage relatively straightforward, the present situation is more intricate. Moreover, the magnetic Prandtl number P_m is an order of magnitude smaller in this case compared to Case 1, implying that total magnetic helicity is not expected to be strongly conserved. This is indeed borne out upon inspection of Figure 6.6(a).

Given the lack of temporal conservation of magnetic helicity in this dynamo, drawing clear causal conclusions based on helicity conservation alone becomes challenging. However, this does not diminish the utility of magnetic helicity in revealing pertinent information. To elucidate the structure of magnetic helicity in this dynamo solution, we confine its calculation to the northern and southern hemispheres separately. The outcomes are depicted in Figure 6.6(b).

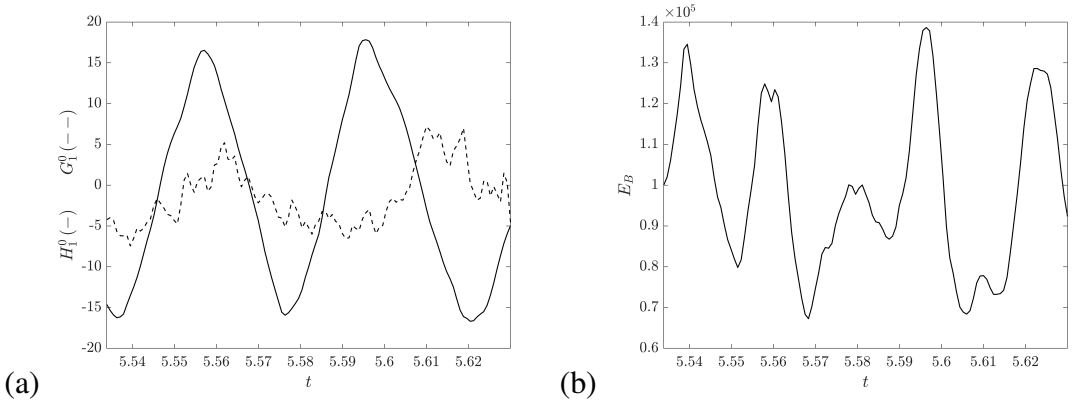

Figure 6.7: Time series related to reversals. (a) displays reversals of the poloidal and toroidal fields. The poloidal and toroidal fields are represented by their dominant spectral expansion components H_1^0 (solid line) and G_1^0 (dashed line), respectively. H_1^0 (solid line) denotes the spherical harmonic expansion coefficient corresponding to the poloidal magnetic field in the $l = 1$ mode, which is the first order in the spectral representation. This component captures the primary variation of the poloidal magnetic field in the system. Similarly, G_1^0 (dashed line) indicates the spherical harmonic expansion coefficient for the toroidal magnetic field, also in the $l = 1$ mode. Similar to H_1^0, this component represents the leading variation of the toroidal magnetic field and provides insights into its dynamics. Both of these quantities are calculated at $r = r_i + 0.5$. (b) displays the total magnetic energy E_B, which oscillates at a frequency similar to the hemispheric helicities displayed in figure 6.6.

The observed asymmetry in magnetic helicity between the northern and southern hemispheres in Case 2 warrants further discussion. Unlike Case 1, where a pure dipolar symmetry resulted in net helicity being zero, the magnetic field structure in Case 2 deviates from this symmetry, leading to a net helicity that is not zero. During the analyzed time series, the absolute value of H_S is consistently greater than that of H_N, resulting in a net helicity $H < 0$ for the majority of the time interval. This discrepancy suggests that the southern hemisphere experiences a more pronounced helicity generation or retention compared to the northern hemisphere. However, it is important to note that this observed asymmetry may only be characteristic of the specific time interval under consideration, and there is no inherent reason for such a pattern to persist indefinitely. As such, future investigations should aim to determine whether this behavior is a transient feature or indicative of a more enduring hemispheric imbalance. Understanding these dynamics could provide valuable insights into the mechanisms driving magnetic helicity generation and the stability of magnetic structures within the dynamo.

Evidently, a distinct wave solution emerges in both hemispheres, with a complete cycle spanning approximately 0.02 time units. This observation suggests that while local variations in magnetic helicity density within a hemisphere may occur, there is no complete alteration in the linkage of hemispheric toroidal and poloidal fields. This global preservation of linkage stems from the nearly simultaneous reversal of the global toroidal and poloidal fields, affording little opportunity for a disparate large-scale linkage to evolve. The reversals of the poloidal and toroidal fields are delineated in Figure 6.7(a). Given that the global toroidal and poloidal fields undergo simultaneous reversals, the linkage, and hence the overall sign, of magnetic helicity in each hemisphere remains unaltered.

This study explores the behavior of magnetic helicity density in the context of geomagnetic reversals using numerical simulations based on Earth-like conditions, rather than direct observations. Our focus is not on any specific celestial body, such as a star or planet, but rather on understanding general dynamo mechanisms. Although measuring magnetic helicity density in Earth's core is currently not feasible, these simulations replicate the dynamics expected in Earth's dynamo, providing valuable theoretical insights into how magnetic helicity density might predict or influence reversals. At $t = 5.54$, there is the clear positive/negative split in the north/south hemispheres. This time corresponds to the peaks of the magnetic helicity magnitudes in the hemispheres (see figure 6.6(b)). As the hemisphere magnitudes decrease to their minima, this is represented in Figure 6.8 by, first, a more mixed pattern of linkage (i.e. increased negative magnetic helicity density in the north and *vice versa* in the south), and then by a decrease in the strength of the magnetic helicity density. These two behaviours can be seen just before and after $t = 5.55$ in Figure 6.8, and repeat for all the cycles shown. The weakening of the density corresponds to the time when the poloidal and toroidal fields reverse and this is followed by the return of these fields to their peak values, resulting in a new phase of dominating positive/negative magnetic helicity density in the north/south hemispheres. While the integrated magnetic helicity density retains its sign within each hemisphere, it undergoes oscillations due to variations in field linkage and magnetic field strength, which are reflected in

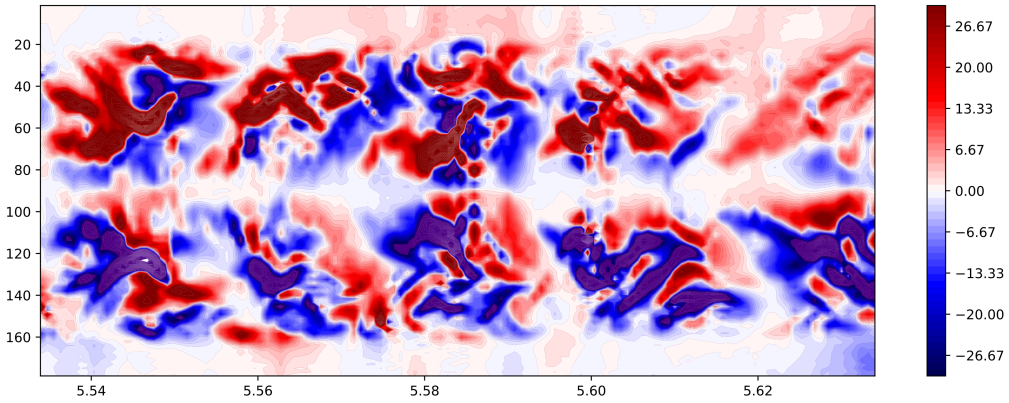

Figure 6.8: A latitude vs time plot of the magnetic helicity density at the surface for Case 2 with a nonlinear colourmap. The color ranges are defined as follows: indigo represents highly negative values (from -400 to -30); seismic colors show values near zero (from -30 to +30); and maroon represents positive values (from +30 to +400). The nonlinear scaling expands the central range, making small variations around zero (in seismic) more visible while compressing larger negative values into a single indigo shade.

the magnetic energy illustrated in Figure 6.7(b). This oscillatory behavior is depicted in Figure 6.6(b). It's crucial to note that global magnetic helicity, whether in each hemisphere or across the entire spherical shell, isn't directly observable in natural dynamos, such as those in stars, because surface measurements only capture localized magnetic field behaviors. However, the magnetic helicity density at the surface serves as an observable quantity that offers insights into the onset of reversals. Figure 6.8 presents a time-latitude plot of magnetic helicity density near the surface, facilitating the identification of reversal occurrences.

Although magnetic helicity density has been more thoroughly studied in solar and stellar dynamos, this research contributes to understanding terrestrial dynamo systems and could be further extended to investigate magnetic reversals in the Sun or other stars. Future technological or theoretical advances may also enable the measurement of magnetic helicity density in Earth-like conditions, enhancing our ability to apply these insights in real-world scenarios.

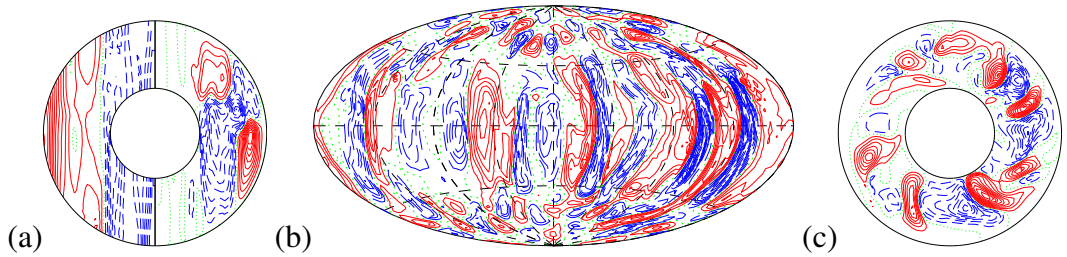

Figure 6.9: Typical structures of the velocity field in the case. (a) shows lines of constant $\overline{u}_\phi$ in the left half and streamlines $r\sin\theta\partial_\theta\overline{v}$ = const. in the right half, all in the meridional plane; (b) shows lines of constant u_r at $r = r_i + 0.5$ and (c) shows streamlines, $r\partial_\phi v$ = const. in the equatorial plane. These images correspond to the time $t = 13.52$ in the simulation.

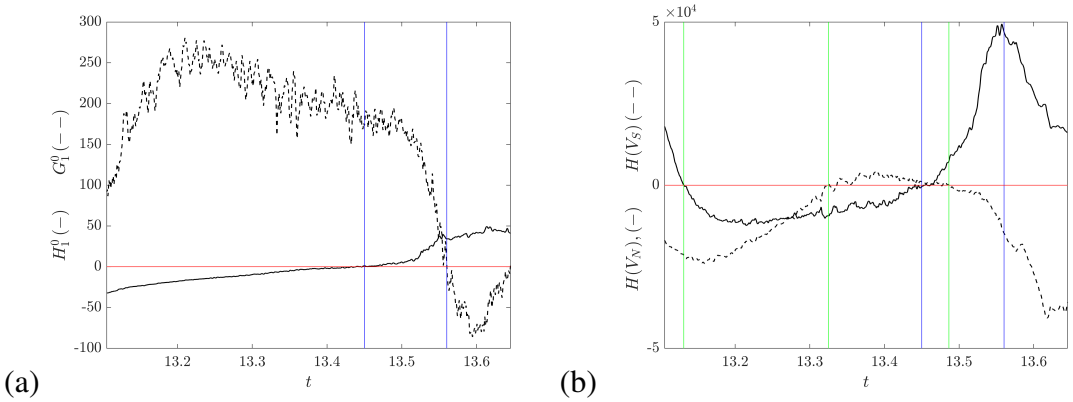

Figure 6.10: Time series during a reversal. H_1^0 (solid) and G_1^0 (dashed) are displayed in (a). Both quantities are evaluated at $r = r_i + 0.5$ The blue vertical lines indicate the reversal times of these quantities. The northern (solid) and southern (dashed) helicities are shown in (b). Reversal times are indicated by green vertical lines. Just before the final green line, there are very small reversals about the $H = 0$ axis, and these are not shown.

6.5 Case 3: Aperiodically-reversing dynamo

Now, we examine a dynamo solution characterized by aperiodic reversals of the global magnetic field. The overall behavior of this dynamo is notably more chaotic compared to the preceding cases, with no discernible precursor pattern for global reversals. The non-dimensional parameters and boundary conditions employed for this case are detailed in the third column of Table 6.1. For comprehensive illustration, we present in Figure 6.9 typical profiles of velocity components for this dynamo solution. Similar to Case 2, the velocity exhibits a columnar yet chaotic morphology.

Given that this particular dynamo solution has been extensively studied in [31], we refrain from reiterating the description provided therein. Instead, our focus shifts to examining the behavior of magnetic helicity during a reversal event. Unlike Case 2, reversals in this dynamo solution do not occur at regular intervals. Nevertheless, despite the dissimilarities between these cases, magnetic helicity once again serves as a valuable tool for interpreting the dynamics of the global magnetic field during a reversal.

Figure 6.10(a) showcases dominant components of the poloidal and toroidal scalars H_1^0 and G_1^0 at a reversal, while Figure 6.10(b) illustrates the integrals of the magnetic helicity density in both the north and south hemispheres. These visualizations offer insights into the evolution of magnetic helicity during reversal events, aiding in the understanding of the underlying dynamics of the dynamo system.

In contrast to Case 2, a notable difference observed in this dynamo solution is the change in sign of hemispheric helicities. The blue lines in Figures 6.10(a) and (b) denote the reversals of H_1^0 and G_1^0 (both evaluated at $r = r_i + 0.5$). Of particular interest are the first two green lines in Figure 6.10(b), which indicate the reversals of $H(V_N)$ and $H(V_S)$, which represent the helicity densities integrated over the northern and southern hemispheres, respectively. Remarkably, these helicity reversals occur significantly earlier than those of H_1^0 and G_1^0. The third green line marks the time at which both $H(V_N)$ and $H(V_S)$ revert to their original signs. Notably, $H(V_S)$ exhibits multiple sign changes immediately prior to this final reversion, indicating a more complex behavior compared to $H(V_N)$. While both helicities revert to their original signs around the same time overall, the multiple fluctuations of $H(V_S)$ prior to its final reversion highlight the intricate dynamics at play in this dynamo solution.

It's important to exercise caution when interpreting reversal times since helicities depend on the magnetic field throughout an entire hemisphere, whereas the values of H_1^0 and G_1^0 presented here are evaluated at a single radius. This approach allows for a more focused analysis of local dynamics, as the magnetic field and helicity can vary significantly with radius. Additionally, computational considerations and the relevance of measurements taken at specific depths make this method practical for connecting with observational data.

Nonetheless, the results suggest a preceding oscillation in hemispheric helicities, leading to sign changes before a global reversal. This observation of the short-term reversals of $H(V_N)$ and $H(V_S)$ could serve as an intriguing early diagnostic of impending global reversals. However, it is essential to note that the long-term decline in H_1^0 might also represent a valid precursor, independent of any helicity diagnostics. In the context of tests involving excursion-like events, where helicity reversals did not occur despite declines or reversals in G_1^0, the analysis suggests that helicity behavior may indeed highlight aspects of the reversal process more effectively than an examination of the magnetic field elements alone.

In essence, the linkage of poloidal and toroidal fields undergoes fluctuations, flipping and returning to its original state, preceding a global reversal. This implies a change in the topology of the magnetic field, reaching an unstable state, albeit transiently. The magnetic field subsequently reverts to a stable (longer-lasting) configuration, and consequently, a stable topological state, through a reversal. This pattern of helicity reversing before a global reversal holds true for other reversals (labelled 2 and 3) occurring in the solution within the simulated time span. These findings are summarized in Table 6.2.

Reversals	H_1^0	G_1^0	$H(V_N)$	$H(V_S)$	$H(V_N)$ and $H(V_S)$
2	26.3232	26.374	26.199	26.3313	26.3504
3	31.2784	31.3534	31.169	31.2532	31.3047

Table 6.2: The helicity and magnetic field reversal times for the other observed reversals.

The quantities discussed thus far in this section are accessible in simulations but not to observers, who only have access to data at the outer surface. Figure 6.11 depicts the magnetic helicity density near the outer surface in a latitude-time plot. This visualization offers insights into the temporal evolution of magnetic helicity density observable from the surface, facilitating the interpretation of dynamical processes within the dynamo system.

The observed trend, where H_N consistently reverses before H_S, can be explained by considering their proximity to the zero line, which represents the equatorial plane. Before the reversals, H_N is typically positive but near the zero line, indicating a weakened state with relatively low magnitude. In contrast, H_S, which starts with a more negative value and is farther from the zero line, reflects a stronger helicity that requires a larger disturbance to reverse. The fact that H_N is weaker and closer to the equator suggests that it can more easily flip its sign when subjected to perturbations in the dynamo. Meanwhile, H_S, being more negative and farther from the zero line, remains more stable and takes longer to reach the reversal point. This behavior can be further understood by recognizing that helicity strengths in stars can vary significantly based on several factors, including the star's type, internal structure, and dynamo dynamics. Asymmetric dynamo action, differential rotation, and local turbulence may amplify or diminish helicity generation differently in each hemisphere, leading to a context-dependent relationship between H_N and H_S. Consequently, H_N reverses first simply because it is already in a near-critical state, requiring less energy to cross the zero line, while H_S, being stronger initially, lags behind in the reversal process due to its more stable configuration. However, the reason for H_N's near-critical state in our simulations remains uncertain and warrants further investigation. Exploring which hemisphere consistently exhibits stronger helicity, whether this behavior varies among different stars, and whether a common pattern exists across stellar types could provide valuable insights into the underlying dynamics of stellar magnetic fields.

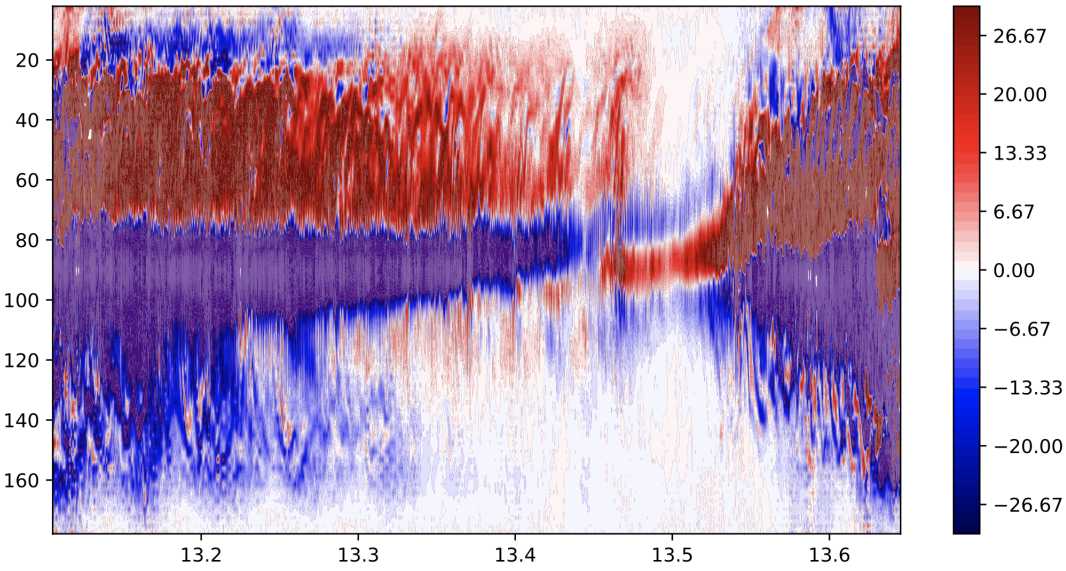

Figure 6.11: A latitude vs time plot of the magnetic helicity density at the surface for Case 3 using a nonlinear colormap. The color ranges are defined as follows: indigo represents highly negative values (from -500 to -30); seismic colors show values near zero (from -30 to +30); and maroon represents positive values (from +30 to +500). The nonlinear scaling expands the central range, making small variations around zero (in seismic) more visible while compressing larger negative values into a single indigo shade.

In Figure 6.11, there is a discernible indication in the behavior of magnetic helicity density at the surface, suggesting the occurrence of reversals. The reversal of H_1^0 in Figure 6.10, denoting the reversal of the poloidal field, transpires around $t \approx 13.45$. Starting from approximately $t \approx 13.28$, there is a notable presence of stronger patches of positive magnetic helicity density near the equator. Around $t \approx 13.45$, a sudden change occurs, resulting in much weaker magnetic helicity density across all latitudes. This subsequently transitions into a phase characterized by strong positive/negative magnetic helicity density, just south/north of the equator. This signature, indicated by a change in sign, is indicative of the reversal of the poloidal field but not the toroidal field. When the toroidal field reverses around $t \approx 13.552$, the distribution of magnetic helicity density returns to its original state. Therefore, even with just information about the magnetic helicity density at the surface, it is possible to discern the reversals of both the global poloidal and toroidal fields.

6.6 Concluding remarks

In this analysis, we have examined three dynamo solutions within rotating spherical shells, investigating the behavior of magnetic helicity in each case. Our methodology involved employing a well-established model (Boussinesq MHD) for convection-driven dynamos in rotating spherical shells and exploring dynamo solutions of increasing complexity—steady (Case 1), periodically-reversing (Case 2), and aperiodically-reversing (Case 3). Despite magnetic helicity not being conserved in the latter two cases, it nonetheless furnishes crucial insights into the magnetic field dynamics across all scenarios.

As per its definition, magnetic helicity serves as a valuable indicator of the linkage between toroidal and poloidal magnetic fields. For dynamo solutions exhibiting reversals, we have elucidated how magnetic helicity correlates with the reversal of both poloidal and toroidal magnetic fields. Moreover, we have highlighted how changes in the magnetic helicity density observable on the surface (a measurable quantity in stars) can signify the onset of reversals.

While magnetic helicity isn't strictly conserved in the simulations under consideration, we refrain from asserting a causal link between reversals and magnetic helicity. However, our findings suggest the existence of preferred states of global magnetic linkage for specific dynamo solutions. When the dynamo deviates from such states, it can revert via a global reversal. For instance, a reversal of the large-scale toroidal field alters the global field linkage. To restore the original linkage, the poloidal field undergoes a reversal, thereby completing the global magnetic field reversal and reinstating the magnetic helicity distribution to its pre-reversal state. Hence, although magnetic helicity may not instigate reversals in these simulations, it unequivocally

signifies the global poloidal-toroidal linkage, intimately associated with reversals. Furthermore, surface maps of magnetic helicity density, measurable in stellar observations, serve as robust indicators of reversal onset, applicable across dynamo solutions featuring distinct reversal mechanisms.

The predominant focus on magnetic helicity in dynamos has revolved around its role in the α-effect within mean-field models. Consequently, there exists an implicit assumption of scale separation of magnetic helicity. In our simulations, we primarily concentrate on large-scale magnetic helicity, which in isolation (without accounting for small-scale contributions) is not conserved. Nonetheless, our findings qualitatively align with certain results from mean-field studies. For instance, in a dynamo model grounded on the Babcock-Leighton α-effect, [46] observed that at the onset of cycles, helicities tend to oppose the preferred hemispheric trends. Temporary alterations in the hemispheric pattern of helicity have also been documented in observational studies [234].

The interpretation of our results in terms of "preferred" states of linkage could offer a fresh perspective on the origin of the hemisphere rule of magnetic helicity. Furthermore, our findings suggest that deviations from this rule may arise from changes in the linkage of large-scale fields (i.e., larger than the small-scale fields considered in mean-field models). While further investigation is warranted in this area, the interpretation of helicity in the context of toroidal/poloidal linkage may aid in refining existing mean-field models that endeavor to elucidate hemisphere imbalances [224].

Chapter 7

Differential rotation in convecting spherical shells with non-uniform viscosity and entropy diffusivity

The results presented in this chapter have been published in [90]. This chapter follows the published paper and includes figures from the paper with the agreement of all authors.

7.1 Introduction

The contemporary understanding of the solar convection zone, derived from sophisticated three-dimensional physics-based simulations, faces a significant challenge. These simulations exhibit notable disparities when compared to observational data. Specifically, they showcase a form of differential rotation that diverges substantially from the rotation pattern inferred through solar helioseismology. Moreover, these simulations display convective flow patterns characterized by a conveyor belt of convective "Busse" columns, a phenomenon not observed in the Sun. This discrepancy, referred to as the "convection conundrum," presents a critical puzzle in solar phys-

ics. Resolving this conundrum is essential for advancing our understanding of solar dynamics and improving the accuracy of solar models. To address this challenge, we investigate the influence of radially non-uniform viscosity and entropy diffusivity on the differential rotation and convective flow patterns within density-stratified rotating spherical fluid shells.

Beyond solar physics, resolving the convection conundrum has implications for our understanding of stellar dynamics and magnetohydrodynamics across a broader astrophysical context. Accurate simulation of solar-like cyclic dipolar dynamos, which are essential for understanding magnetic field generation in stars, depends on a precise grasp of the underlying convective and rotational processes.

As discussed in detail in earlier chapters, the convective motions within the Sun's interior play a critical role in the generation and maintenance of its magnetic fields, which drive a range of solar phenomena, including flares, coronal mass ejections, and the solar dynamo. Recent high-resolution simulations of thermal convection and magnetic field generation in rotating spherical shells have become key tools in investigating these dynamics. These simulations offer valuable insights into the interaction between convection, rotation, and magnetic fields, enhancing our ability to interpret observational data. For example, recent efforts have focused on utilizing time-distance helioseismology techniques to constrain models of meridional circulation, shedding light on the large-scale flow patterns within the Sun's interior [205]. Additionally, studies have delved into minimal models aimed at elucidating the dynamics of the solar cycle, with particular emphasis on the role of non-axisymmetric components of the magnetic field ($m = 1$ or $m = 2$) [192]. By leveraging both simulation and observational approaches, researchers strive to gain a comprehensive understanding of solar dynamics and the underlying processes driving solar magnetic phenomena.

Despite these advances, fundamental challenges persist in modeling the solar dynamo. Notably, the "convection conundrum" emphasizes two major discrepancies. First, simulations of differential rotation and convective velocities do not align with helioseismic observations. Second, the simulated emergence of large-scale Busse columns is not corroborated by observational evidence [45, 103]. Differential rotation, a cornerstone of the Sun's global dynamics, is meticulously measured through helioseismic inversion techniques [211, 104]. Its intricate features include the variation in rotational speed across latitudes, with the equatorial regions exhibiting faster rotation (around 25 days) compared to the slower rotation observed near the poles (around 36 days). This rotation pattern forms a conical profile, characterized by nearly radial orientation of angular velocity isocontours at intermediate latitudes, contributing significantly to the overall dynamical behavior of the solar interior.

In the realm of solar convection simulations, a recurring challenge lies in accurately reproducing isocontours of the angular velocity that deviate significantly from the axis of rotation within the convection zone. Instead, most simulations tend to exhibit isocontours parallel to the axis of rotation, which is at odds with observational data [219, 89, 136]. However, notable exceptions exist, such as the simulations conducted by [142], where conically tilted contours were achieved by introducing a moderately large latitudinal entropy gradient.

The accurate portrayal of differential rotation is of paramount importance due to its pivotal role in various solar phenomena. Notably, it is instrumental in the generation of magnetic fields through the Ω effect, facilitating the conversion of poloidal to toroidal magnetic fields. Additionally, the dynamics of differential rotation are closely tied to the oscillations of dynamo waves, akin to the solar cycle, as evidenced by flux-transport dynamo models [55] and certain global simulations [114, 217, 192, 194].

In the subsequent sections of this chapter, we delve into the demonstration that significantly large latitudinal entropy gradients can emerge self-consistently within our simulations, obviating the need for additional imposition. This discovery holds promise in enhancing the agreement between our simulation results and observational data, thereby advancing our understanding of solar dynamics and convection processes.

In contrast to planetary cores and atmospheres, where the basic density and material properties of the fluid change only weakly, the solar interior, including the convection zone, exhibits significant radial variations in thermodynamic quantities and properties. Reference-state radial distributions of density, temperature, and pressure in the convection zone can be estimated based on helioseismic arguments or solar evolution models [23]. While molecular viscosity and thermal diffusivity profiles can theoretically be inferred from molecular dynamics calculations [71], the strong turbulence present in the solar convection zone complicates the use of these molecular values to adequately represent the profiles of effective viscosity and thermal diffusivity in global convective dynamo models. Consequently, the radial distributions of viscosity and entropy diffusivity remain largely modelling choices, yet crucial ones, as they are expected to influence the style and spatial location of convection, thereby affecting the properties of the global dynamo process. For instance, the radial profile of entropy diffusivity directly influences the entropy distribution, and consequently, the local convective stability. Early studies by Glatzmaier and Gilman [81] explored various choices of viscosity and entropy diffusivity profiles, finding that under moderate shell rotation rates, convection shifts from the outer to inner regions as diffusivities are increased in the outer regions and decreased in the inner regions. Several subsequent studies of solar convection have assumed viscosity and diffusivity profiles as functions involving a negative power of the mean density (e.g., [24, 23, 25, 81]), rather than the more commonly used uniform profiles (e.g., [218, 136, 217, 115, 194, 21, 143]). In a recent investigation by [181], the effects of a radial distribution of entropy diffusivity on critical modes of anelastic thermal convection in a rotating spherical shell were explored. Their findings indicated strong effects on convection morphology and location, albeit limited to linear onset analysis and con-

sidering only uniform viscosity. Extending this work to nonlinear regimes, particularly with a focus on improving the agreement between computed and observed solar differential rotation, constitutes the goal of the present study. By delving into the nonlinear dynamics of convective processes with non-uniform viscosity and entropy diffusivity profiles, we aim to provide deeper insights into the mechanisms shaping solar convection and its implications for the observed solar dynamics.

Contents. In this study, we conducted a series of numerical simulations based on the framework proposed by [194], which we expanded to include radially non-uniform profiles of viscosity and entropy diffusivity. By comparing these simulations with baseline reference simulations utilizing uniform profiles, we aimed to elucidate the specific effects of these assumptions on the dynamics of the convecting spherical shells. To ensure the robustness of our findings, we explored scenarios encompassing both high and low values of the Prandtl number. The structure of this thesis is organized as follows: In Section 7.2, we provide an introduction to the mathematical model employed in our study. Following this, Section 7.3 presents our primary results, focusing on the influence of non-uniform material properties on the structure of differential rotation. Section 7.4 delves deeper into our findings, proposing a plausible mechanism to account for the observed effects, presenting additional supporting evidence, and discussing the limitations inherent in our study's approach. Finally, we draw our conclusions in Section 7.5, summarizing the key insights gleaned from our investigations into the convection conundrum and outlining avenues for future research in this field.

7.2 Mathematical model

In this work, we extend the model of Jones et al. [105] by including radially non-uniform viscosity and entropy diffusivity. Our numerical implementation, methods of solution, and analysis follow Simitev [194].

We consider a model previously detailed in Chapter 3, Section 3.2.1, where an electrically conducting perfect gas is confined to a spherical shell that rotates about the vertical axis with a fixed angular velocity ($\Omega_0\hat{\mathbf{k}}$) and an imposed entropy contrast (ΔS) between the inner and outer surfaces. The gravitational field is assumed to vary as the inverse square of the radial distance, leading to a hydrostatic, polytropic reference state. For more comprehensive details on the governing equations and parameters, please refer to Chapter 3.

Convection and magnetic field generation in this system are described by the evolution equations of continuity, momentum, energy, and magnetic flux, using the Lantz-Braginsky-Roberts formulation of the anelastic approximation [105]. These equations are detailed in Chapter 3.

The viscosity (ν) and entropy diffusivity (κ) are assumed to have radially non-uniform profiles:

$$\nu(r) = \nu_c \left(\frac{\overline{\rho}}{\rho_c}\right)^p, \quad \kappa(r) = \kappa_c \left(\frac{\overline{\rho}}{\rho_c}\right)^q, \tag{7.1}$$

where ν_c and κ_c are their values in the mid-shell, while p and q are modelling constants.

The formulation is characterized by seven non-dimensional parameters: the radius ratio (η), the polytropic index (n), the density scale number (N_ρ), the Rayleigh number (R), the thermal Prandtl number (P_r), the magnetic Prandtl number (P_m), and the Coriolis number (τ). These parameters are crucial for understanding the dynamics of the system. The equations are supplemented by no-slip boundary conditions on the inner surface and stress-free conditions on the outer surface. For the entropy, a fixed contrast is imposed between the inner and outer surfaces. Lastly, "vacuum" boundary conditions for the magnetic field are derived from the assumption of an electrically insulating external region. The boundary value problem expressed by these equations and conditions is three-dimensional, time-dependent, highly coupled, and nonlinear; for these reasons, it can only be solved numerically. Refer to Chapter 4 for a discussion on the numerical methods used for their solution. The calculations reported below were performed with resolutions of $(n_r, n_\theta, n_\phi) = (71, 193, 193)$, corresponding to the number of radial, latitudinal, and azimuthal (zonal) grid points, respectively.

7.3 Results

Design of the study and choice of parameter values. The development of an equation describing the evolution of differential rotation induced by thermal convection within a rotating spherical shell involves averaging the longitudinal component of the momentum equation. This process reveals that the differential rotation is sustained through a delicate equilibrium involving Reynolds and Maxwell stresses, influenced by factors such as meridional circulation, magnetic tension, and viscous dissipation [141, 206]. Various parameter values influence these stresses, and to specifically analyze the impact of non-uniform viscosity and entropy diffusivity profiles on the differential rotation's shape and structure, we maintain consistency in the non-dimensional parameters where feasible. Specifically, we set

$$\eta = 0.65, \quad n = 2, \quad N_\rho = 3, \quad \mathrm{R} = 3 \times 10^6, \quad \tau = 2000. \tag{7.2}$$

Keeping the parameter values fixed aids in narrowing down the extensive eight-dimensional parameter space to a more manageable size. The choice of $\eta = 0.65$ results in a slightly thicker shell compared to the solar convection zone ($\eta = 0.7$), primarily for computational convenience. Additionally, the size of convective structures is influenced by the shell's thickness; thinner shells necessitate higher-order spherical harmonic expansions to accurately resolve the flow's angular structure. With $\tau = 2000$, the Coriolis number is moderately but not excessively large, reflecting the model assumption that the flow in the deep convection zone is buoyancy- rather than rotation-dominated, although the effects of rotation are also essential. The chosen value of the polytropic index ($n = 2$) exceeds that of an ideal gas ($n = 3/2$), and the density-scale height ($N_\rho = 3$) is considerably smaller than estimates for the solar convection zone. However, pushing N_ρ much beyond 5 becomes computationally impractical. These parameter selections are anticipated to have minimal impact on the system's dynamics and are consistent with our previous research [194].

The flow's structure and strength are notably influenced by the Rayleigh number, which has been extensively studied in prior research (see, for instance, [190, 194] and references therein). In this study, we present a comparison of cases with identical and moderately large Rayleigh numbers, systematically increasing this parameter from its onset in Section 7.4.2. While there is a robust understanding of the Rayleigh number's impact, the influence of the Prandtl number remains less explored, with some insights from studies like [193, 111].

Linear stability analyses [1, 33] and finite-amplitude simulations of thermal convection in a rapidly rotating thick shell under the Boussinesq approximation [190, 193] show that at low Prandtl number values, convection adopts the equatorially attached regime [235, 33], where the Coriolis force's contribution is minimal. As the Prandtl number approaches unity, Coriolis effects

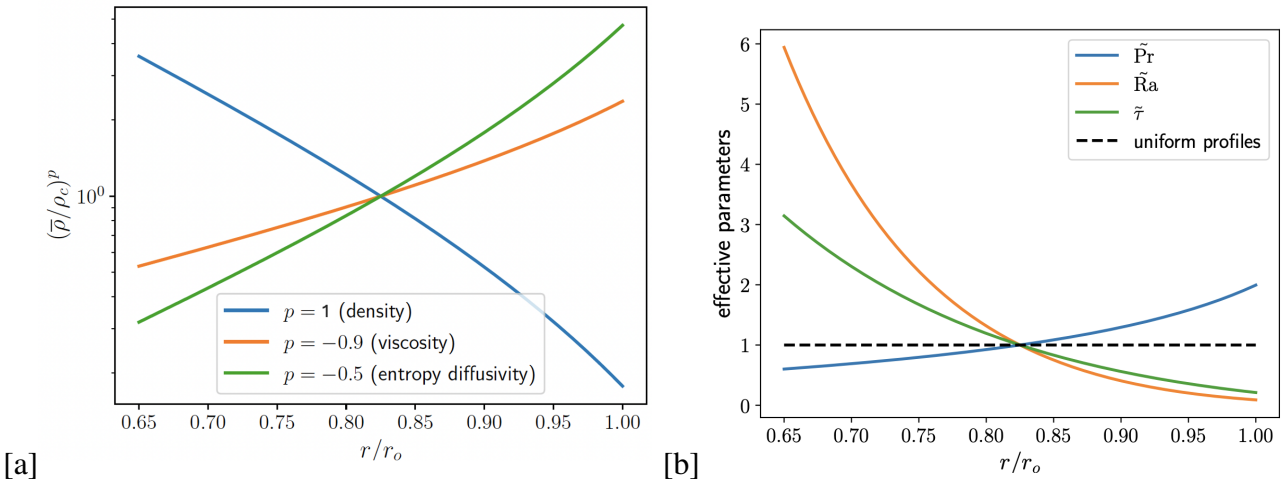

Figure 7.1: Radial profiles for different model parameters. (**a**) Non-uniform viscosity and entropy diffusivity vary relative to the density. (**b**) The effective non-dimensional parameters $\tilde{R}$, $\tilde{P}_r$, and $\tilde{\tau}$ change due to the radial dependence introduced by the non-uniform viscosity $\nu(r)$ and entropy diffusivity $\kappa(r)$. These effective values are derived from the radial profiles of the diffusivities, illustrating how they influence the behavior of the system compared to a uniform profile. For display purposes, all parameters were normalized with respect to their values at the center of the spherical shell.

become more pronounced, leading to a spiraling convection regime characterized by elongated structures from the inner to the outer surface. To further investigate the Prandtl number's influence, we contrast simulations with low ($P_r = 0.3$), moderate ($P_r = 1$), and slightly higher values ($P_r = 5$).

To meet the objectives of our study, we compare simulations employing uniform radial profiles of viscosity and entropy diffusivity with those employing non-uniform profiles where $\bar{\nu} \propto \rho^{-0.9}$ and $\bar{\kappa} \propto \rho^{-0.5}$, respectively. Given the absence of precise observational or theoretical constraints, these dependencies were chosen to maximize the deviation of the two profiles from uniformity under the fixed parameter values mentioned earlier, ensuring well-resolved solutions. The depicted radial profiles of viscosity, entropy diffusivity, and density in the model are illustrated in Figure 7.1a.

Table 7.1: Model parameters and energy densities for six selected dynamo solutions.

	A	B	C	D	E	F
Type	**Uniform**	**Non-Uniform**	**Uniform**	**Non-Uniform**	**Uniform**	**Non-Uniform**
η	0.65	0.65	0.65	0.65	0.65	0.65
R	3×10^6	3×10^6	3×10^6	3×10^6	3×10^6	3×10^6
τ	2000	2000	2000	2000	2000	2000
P_r	0.3	0.3	1	1	5	5
N_ρ	3	3	3	3	3	3
n	2	2	2	2	2	2
P_m	1	1	4	4	10	10
$\overline{E}_{tot}$	11,785.6	18,627.4	846.488	1006.96	29.1356	20.9883
$\overline{E}_p$	23.7465	64.0577	0.97983	4.29216	0.0215626	0.0870345
$\overline{E}_t$	5930.15	11,540.3	182.149	570.75	4.7595	1.32042
$\check{E}_p$	1946.24	1746.21	271.194	175.511	11.0902	6.81947
$\check{E}_t$	1574.74	2261.39	207.107	218.885	9.35735	11.5854
$\overline{M}_{tot}$	1189.03	0.0662693	464.484	14.92	21.4386	0.638192
$\overline{M}_p$	6.26582	0.00139628	4.48705	0.117454	0.463097	0.0718596
$\overline{M}_t$	13.3781	0.0012872	6.38913	0.129885	0.43025	0.0194026
$\check{M}_p$	256.771	0.0164442	111.957	4.44414	5.34042	0.181853
$\check{M}_t$	290.496	0.0153525	105.607	3.82462	4.41429	0.0936899
Rm	153.5291	193.0150	164.5828	44.8767	76.3350	64.7890
Ro	0.1535	0.1930	0.0411	0.0448	0.0076	0.0064
Lo	0.0487	0.0003640	0.0304	0.0054	0.0065	0.001129

The Prandtl, Rayleigh, and Coriolis numbers mentioned earlier correspond to fluid properties at the midpoint of the spherical shell. However, due to the utilization of non-uniform viscosity and entropy diffusivity in this study, these quantities' effective values vary with radius, as depicted in Figure 7.1b. This variation notably influences the local structure and intensity of the flows, a topic further elaborated below. To summarize this discussion, Table 7.1 presents the six primary dynamo solutions that are the focal point of our attention throughout most of this chapter. Additionally, the table furnishes the values of several crucial global average attributes, encompassing energy density components that delineate various aspects of the flow. It is important to note that all simulations presented in this table were performed at the same value of the Rayleigh number R. However, the degree of supercriticality, expressed as R/R_c (where R_c is the critical Rayleigh number), varies between runs. This variation in supercriticality affects the convective behavior and, consequently, the dynamo processes, making it an important factor to consider when interpreting the results. Furthermore, the table includes diagnostic parameters such as the magnetic Reynolds number $Rm = \frac{uL}{\eta}$, which measures the ratio of magnetic advection to diffusion (where u is the characteristic velocity, L is the characteristic length scale, and η is the magnetic diffusivity); the Rossby number $Ro = \frac{u}{\Omega D}$, which compares inertial forces to Coriolis forces (where

u is the characteristic velocity, Ω is the angular rotation rate, and D is the characteristic length scale); and the Lorentz number $Lo = \frac{B^2}{\mu_0 \rho u^2}$, which quantifies the ratio of magnetic forces to inertial forces (where B is the magnetic field strength, μ_0 is the magnetic permeability, ρ is the fluid density, and u is the characteristic velocity). These parameters are essential for understanding the dynamo behavior: Rm quantifies the ratio of magnetic induction to magnetic diffusion, Ro characterizes the relative importance of inertial forces compared to Coriolis forces, and Lo measures the influence of the Lorentz force relative to inertial forces. Specifically, the mean and fluctuating toroidal and poloidal components of the total kinetic energy (E_{tot}) are defined as follows:

$$\bar{E}_p = \langle \left(\nabla \times (\nabla \bar{v} \times \mathbf{r}) \right)^2 / (2\bar{\rho}) \rangle, \quad \bar{E}_t = \langle \left(\nabla r \bar{w} \times \mathbf{r} \right)^2 / (2\bar{\rho}) \rangle, \tag{7.3a}$$

$$\check{E}_p = \langle \left(\nabla \times (\nabla \check{v} \times \mathbf{r}) \right)^2 / (2\bar{\rho}) \rangle, \quad \check{E}_t = \langle \left(\nabla r \check{w} \times \mathbf{r} \right)^2 / (2\bar{\rho}) \rangle, \tag{7.3b}$$

The notation used here employs angular brackets to signify averages over the spherical volume of the shell, bars to denote axisymmetric parts, and check marks to denote non-axisymmetric parts of a scalar field. Similarly, the total magnetic energy (M_{tot}) can be divided in a parallel manner, with components defined akin to Equations (7.3a) and (7.3b), where h and g replace v and w respectively, and excluding the $\bar{\rho}^{-1}$ factor within the angular brackets. It's important to note that the total energies encompass the sum of all these components. **Comparing simulated differential rotation with observational data.** To evaluate the impact of non-uniform viscosity and entropy diffusivity profiles on the overall structure of the differential rotation, it's essential to compare the model solutions with the observed solar differential rotation profile, which has been extensively measured [211]. As previously mentioned, the angular velocity (Ω) is depicted in Figure 7.2a, sourced from Howe [104]. Notably, the highest rotational speeds cluster near the equator, with contours of constant rotation closely aligning with lines oriented at approximately 25° to the axis of rotation. These features characterize what we term "conical" differential rotation, as opposed to "cylindrical" rotation parallel to the rotation axis. To facilitate our numerical implementation, we opted for a simpler yet sufficiently accurate analytical approximation devised by Kosovichev [121], as illustrated in Figure 7.2b. Here, we omitted the

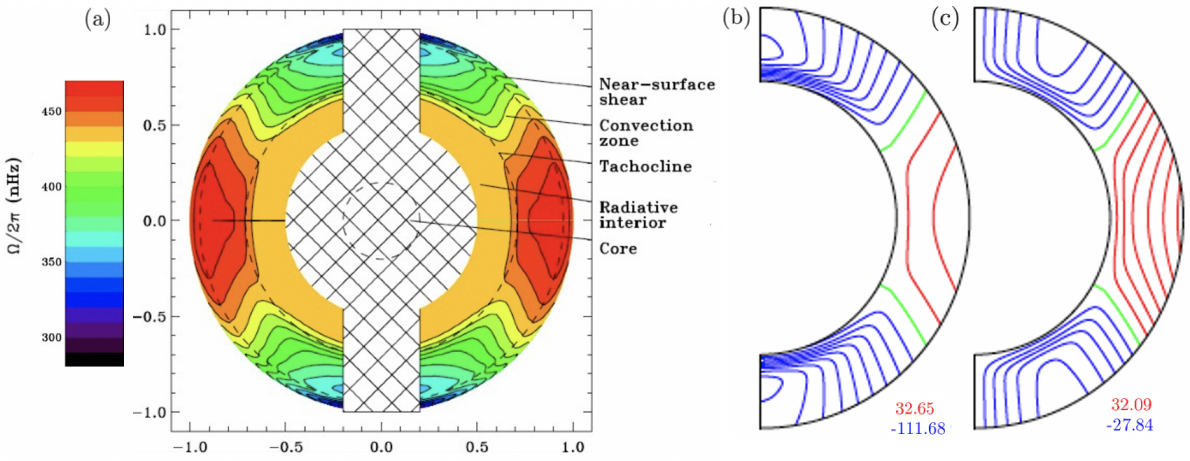

Figure 7.2: The observed profile of the solar differential rotation.(**a**) Cross-sectional view of the Sun's interior, depicting contours of constant angular velocity (Ω) temporally averaged over 12 years of Stanford Michelson Doppler Imager (MDI) data. Image adapted from Howe [104] (Springer Nature, licensed by CC BY 4).(**b**) The solar angular velocity relative to the rotation frame of the Sun $(\Omega - \Omega_\odot)$, with solar frame rotation of $\Omega_\odot = 870\pi$ nHz. A closed-form approximation is used according to Kosovichev [121]. (**c**) Azimuthally averaged zonal velocity $(r\sin\theta(\Omega - \Omega_\odot))$ in the rotating frame is used for comparison with simulation results. Maximum and minimum values are indicated in (**b**,**c**), respectively; contour lines are equidistant, with positive levels in red and negative levels in blue (this style is used throughout).

quiescent radiative interior, the thin near-surface shear layer, and the tachocline layer, as these elements are not encompassed by our mathematical model. This simplification allows us to focus on the primary dynamics of the convection zone, but it is important to note that these layers significantly influence solar behavior. Future research could incorporate these layers to enhance the understanding of their effects on convection and magnetic field dynamics.

Given that the equations of our model are formulated with respect to a rotating coordinate system, we subtracted the Sun's rigid frame rotation ($\Omega_\odot = 870\pi$ nHz). Figure 7.2c showcases the corresponding zonal (linear) velocity ($u_\varphi = r\sin\theta(\Omega - \Omega_\odot)$), with the distance from the center (r) measured in the dimensional units of our model (shell thickness). Figure 7.3 shows a direct comparison of the azimuthally averaged zonal velocity ($\bar{u}_\varphi$) of our model solutions with the latter profile (Figure 7.2c). Our primary interest here is the shape of the differential rotation profile, so we rescaled the reference profile to obtain the same maximum at the equator as the simulation results. We scaled with respect to the equatorial maximum, since our model

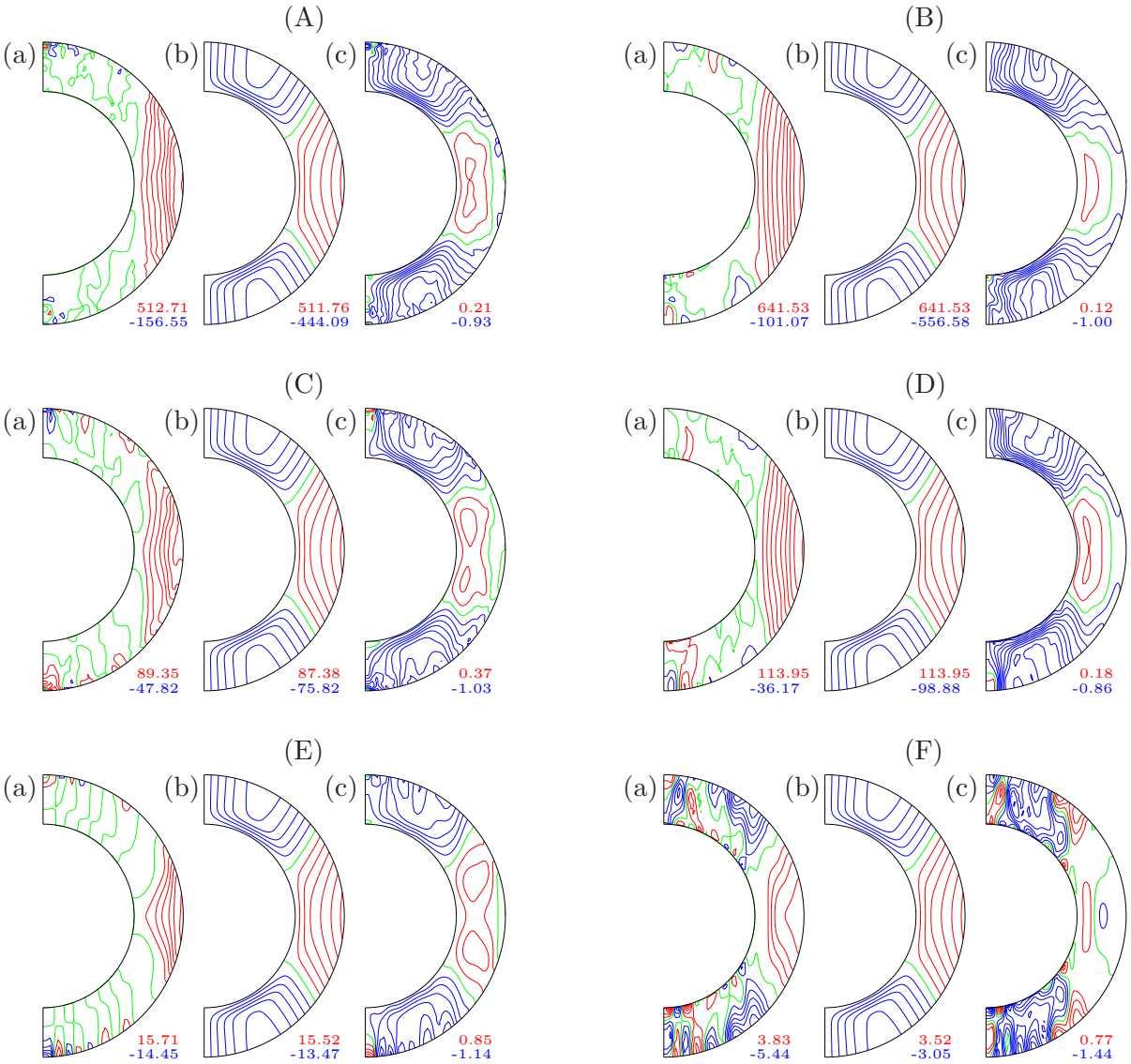

Figure 7.3: Differential rotation of the dynamo solutions under consideration. The three rows correspond to (**A**,**B**) $P_r = 0.3, P_m = 1$, (**C**,**D**) $P_r = 1, P_m = 4$ and (**E**,**F**) $P_r = 5, P_m = 10$; other parameters have the same values as in (7.2) . Cases (**A**,**C**,**E**) have uniform viscosity and entropy diffusivity profiles; cases (**B**,**D**,**F**) have non-uniform profiles. In each group of three subfigures, (**a**) displays isocontours of the azimuthally averaged zonal velocity ($\overline{u}_\varphi$), (**b**) displays the reference observational profile of differential rotation ($r\sin\theta(\Omega - \Omega_\odot)$) rescaled to obtain the same maximum at the equator as in (**a**),(**c**) displays the relative difference between the quantities represented in Figures **a** and **b**, normalized to the maximum value of the data shown in Figure **b**.

is primarily concerned with the profile in the tangent cylinder. For the smallest value of the Prandtl number ($P_r = 0.3$) and with uniform profiles of $\bar{\nu}$ and $\bar{\kappa}$, Figure 7.3(Aa) shows that the differential rotation is geostrophic, with contour lines of $\bar{u}_\varphi$ parallel to the rotation axis and a prominent prograde jet filling the region outside of the tangent cylinder (the coaxial cylinder

with frame rotation axis and tangential to the inner core of the shell at the equatorial plane), while within the tangent cylinder, the zonal velocity vanishes. This pattern compares poorly with the solar profile shown in Figure 7.3(Ab), which is also reflected in Figure 7.3(Ac), where errors appear across all latitudes.

The inclusion of radially non-uniform profiles of $\bar{\nu}$ and $\bar{\kappa}$ seems to have a negligible effect on the differential rotation, which retains the structure just described (Figure 7.3B). Somewhat surprisingly, little further change to the pattern is seen at the moderate value of the Prandtl number ($P_r = 1$) in both uniform and non-uniform profiles of $\bar{\nu}$ and $\bar{\kappa}$ (Figure 7.3C,D). At a large value of the Prandtl number ($P_r = 5$), the contours of zonal velocity start to deviate from a cylindrical shape (Figure 7.3(Ea)). The effect is strongly amplified in the case of non-uniform viscosity and entropy diffusivity (Figure 7.3(Fa)) and assumes a shape very similar to that of the observed solar rotation profile shown in Figure 7.3(Fb), resulting in vanishingly small discrepancies at mid latitudes (Figure 7.3(Fc)).

It is notable that in the latter case, differential rotation develops within the tangent cylinder at high latitudes and in the polar regions. However, the structure of the polar differential rotation in Figure 7.3(Fa) is more complicated and messier compared to the reference solar rotation profile in Figure 7.3(Fb). While this structure features a relatively large retrograde polar jet, similar to the true solar zonal flow, the flow pattern inside the tangent cylinder appears more disordered and less coherent than expected. Additionally, the magnitude of the zonal flow within the tangent cylinder, although present, is relatively small compared to the reference profile. These points are especially evident when examining the error term (Figure 7.3(Fc)), where the discrepancies between the simulated and true profiles remain low in terms of magnitude, suggesting that while the flow structure is less organized, the deviations are not significant.

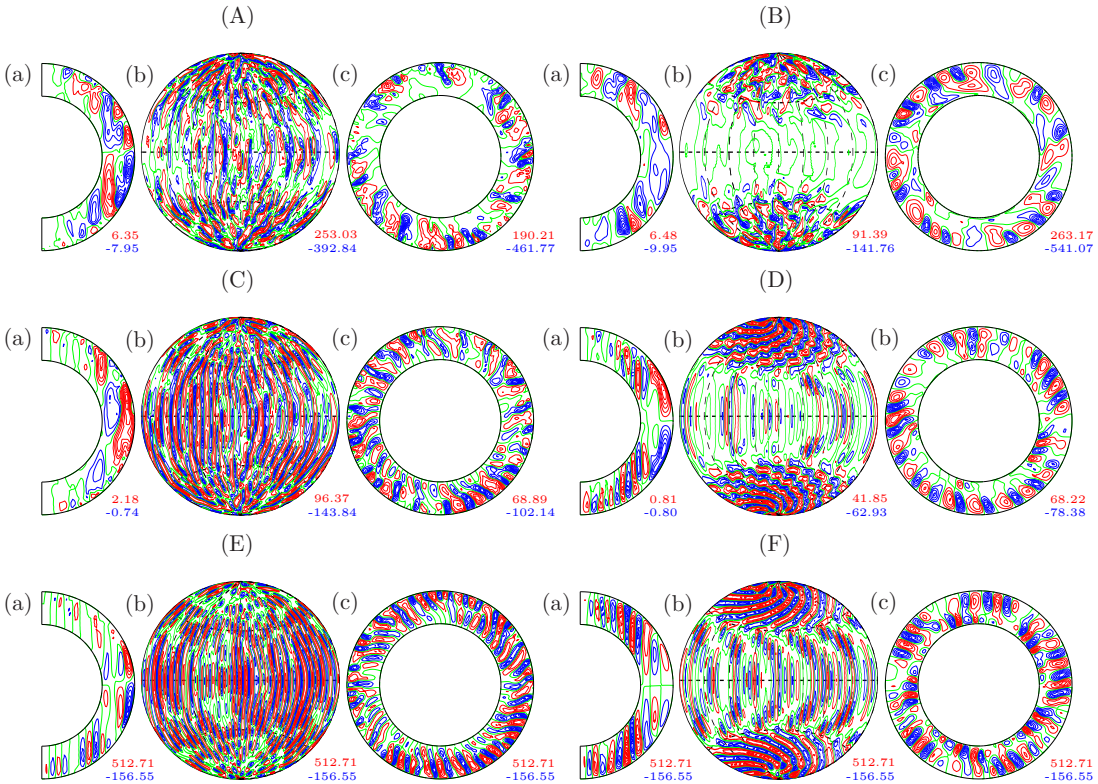

Figure 7.4: Flow structures of the cases shown in Figure 7.3 and labeled in the same way. In each group, (**a**) displays azimuthally averaged meridional circulation in a meridional plane, (**b**) displays isocontours of the radial velocity (u_r) on the spherical surface at $r = 0.5$ and (**c**) shows poloidal streamlines of the velocity field in the equatorial plane.

We note that comparison in the polar regions is subject to greater uncertainty. Firstly, in simulations, numerical error increases when the distance from the axis of rotation tends toward zero, which occurs in the polar region. Secondly, the polar regions of the Sun are not in a direct line of sight, so observational measurements in these regions are less accurate.

In summary, the simulation that produces the most solar-like differential rotation is that described in column F of Table 7.1. Details of this simulation are displayed in Figures 7.3F, 7.4F and 7.5F and discussed further below.

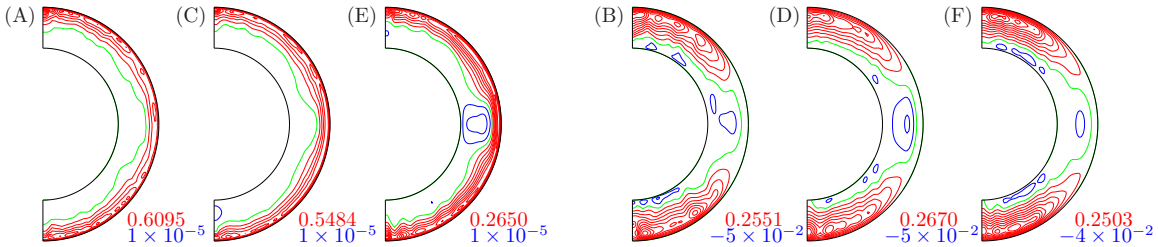

Figure 7.5: Azimuthally and time-averaged entropy ($\langle S \rangle_{\varphi,t}$) for the cases plotted in Figures 7.3 and 7.4 and labeled in the same way, i.e., uniform profiles (**A**,**C**,**E**) and non-uniform profiles (**B**,**D**,**F**) of viscosity and entropy diffusivity, as well as (**A**,**B**) $P_r = 0.3$, (**C**,**D**) $P_r = 1$ and (**E**,**F**) $P_r = 5$, with other parameters from Figure 7.4.

7.4 Discussion including further results

7.4.1 Flow structure and thermal wind balance analysis

To delve into the evolving concurrence between observed and measured zonal flows amid non-uniform viscosity and entropy diffusivity at higher Prandtl numbers, Figure 7.4 offers a comprehensive visualization of the remaining fluid flow components for the same simulations referenced in Figure 7.3. Outside the tangent cylinder, convection manifests as rolls aligned with the rotation axis, resembling properties akin to thermal Rossby waves, drifting progradely in the azimuthal direction. This convection, minimizing variations in the axis of rotation direction, is best discerned through equatorial plane streamlines, as depicted in the third and sixth columns (c) of Figure 7.4. These equatorial cross-sections illustrate the spiral configuration of the convection columns, which gradually diminishes in prominence with increasing Prandtl number (P_r).

The convection columns extend into the region near the tangent cylinder, which is a vertical cylinder tangent to the outer surface of the shell at the inner radius. This is evident in the plots of radial velocity projected onto the spherical surface at the mid-shell (second and fifth columns (b) of Figure 7.4). A notable effect of non-uniform profiles of viscosity ($\bar{\nu}$) and entropy diffusivity

($\bar{\kappa}$), in contrast to uniform-profile simulations, is the emergence of predominant convection flow in the polar regions within the tangent cylinder. Here, with gravity and rotation vectors nearly parallel, the convection mimics that of a horizontally heated layer rotated about a vertical axis, modulated by interactions with external convection outside the tangent cylinder.

As observed in relation to Figure 7.3, differential rotation in the polar regions is retrograde, which tends to alleviate rotational constraints, fostering a feedback loop that bolsters the polar flow. At the highest Prandtl number ($P_r = 5$), the polar flows become notably robust and organized into elongated rolls resembling bicycle wheel spokes, originating from the rotation axis and gently spiraling in the retrograde direction towards the opposite periphery, counter to the drift of equatorial structures.

The conspicuous presence of robust and well-structured polar convection suggests an augmented entropy transport in the polar regions compared to the equatorial regions. To confirm this, Figure 7.5 depicts the latitude gradient of entropy across all cases discussed in Figures 7.3 and 7.4.

A notable disparity emerges between the uniform cases (Figure 7.5A, C, E) and the non-uniform cases (Figure 7.5B, D, F), with a break in positive $\langle S \rangle_{\varphi,t}$ from all latitudes to high latitudes. This finding holds significance as deviations from geostrophic (cylindrical) differential rotations are known to be accentuated by the presence of non-zero latitudinal entropy gradients [206, 162, 141].

However, as seen in case (F) (non-uniform viscosity/diffusivity, $P_r = 5$), there is a notable discrepancy between the largest latitudinal entropy gradient (Figure 7.5F) and the weaker zonal flows shown in Figure 7.3. While thermal wind balance suggests that stronger entropy gradients should lead to stronger zonal flows, in this case, the large entropy gradients are accompanied

by weaker flows inside the tangent cylinder. This counter-intuitive result can be explained by the significant convection in the polar regions, which is particularly strong and organized into structured rolls. These rolls disrupt the development of strong zonal flows by dissipating energy into vertical motions. Additionally, the retrograde polar jets seen in Figure 7.3 (F(a)) may counteract the mid-latitude zonal flows, contributing to their reduced strength. The high Prandtl number and non-uniform profiles also introduce non-linear feedbacks that limit the zonal flow development, even in the presence of large entropy gradients.

In our simulations, where pressure gradients, Coriolis and buoyancy forces achieve dominant balance, akin to conditions potentially prevailing in the bulk of the solar convection zone, the zonal component of the curl of the momentum equation simplifies to the well-known thermal wind balance [146].

$$\hat{\mathbf{k}} \cdot \nabla \langle \mathbf{u}_\varphi \rangle_t \quad \propto \quad \frac{\partial \langle S \rangle_{\varphi,t}}{\partial \theta}, \tag{7.4}$$

which is a generalisation of the Taylor–Proudman theorem for rotating fluids in the presence of buoyancy. This relation shows that in or close to an adiabatic state, if $\partial \langle S \rangle_{\varphi,t} / \partial \theta \approx 0$, then the rotation profile must be close to cylindrical and when, on the other hand, significant latitudinal entropy gradients are present. As in the cases of non-uniform viscosity and diffusivity profiles shown in Figure 7.5, non-cylindrical differential rotation is promoted.

To summarise, the radially non-uniform viscosity and entropy diffusivity profiles allow enhanced convection to develop at the poles, resulting in a non-vanishing entropy gradient with increased latitude. In turn, this helps to produce more solar-like differential rotation according to Equation (7.4).

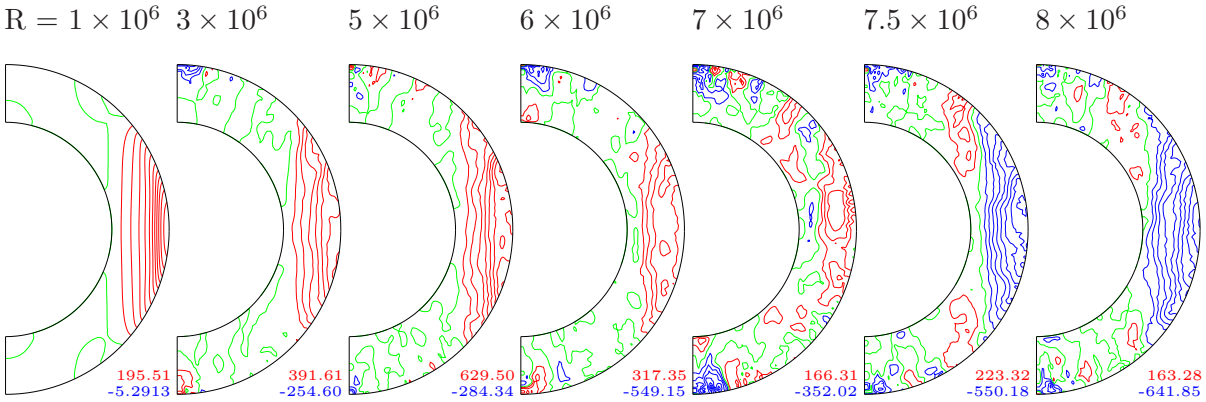

Figure 7.6: Differential rotation as a function of the Rayleigh number and the solar/antisolar transition. Isocontours of azimuthally averaged zonal velocity ($\overline{u}_\varphi$) are plotted for the Rayleigh number values indicated in the plot at specific moments in time. The rest of the parameter values are specified in (7.2), with $P_r = 0.3$ and uniform $\bar{\nu}$ and $\bar{\kappa}$ values.

7.4.2 Secondary aspects to consider

In this initial investigation, our exploration of the model's behavior within the available parameter space was not exhaustive. Our primary emphasis was directed towards the principal novel enhancements of our model, specifically the incorporation of non-uniform $\bar{\nu}$ and $\bar{\kappa}$ profiles. Nevertheless, we acknowledge the existence of additional effects and processes that could potentially influence the described outcomes, albeit perhaps in quantitative terms. We briefly discuss two such considerations here.

Solar–antisolar transition. Firstly, in Figures 7.3–7.5, our discussion was limited to a few cases featuring an identical but fixed value/profile of the effective Rayleigh number. The Rayleigh number serves as a gauge of buoyancy's contribution to the overall force balance within the system; even when uniform viscosity and entropy diffusivity are assumed, it exerts a significant influence on convection dynamics. This dependence has been extensively investigated through linear instability analyses and finite-amplitude simulations under various conditions and approximations. Noteworthy references to our own studies include [190, 38, 135], while recent review papers such as [45] offer comprehensive overviews.

Here, we emphasize that as buoyancy-driven forcing increases, an abrupt transition occurs from prograde solar-like differential rotation to retrograde antisolar differential rotation in the equatorial region. Figure 7.6 illustrates this phenomenon across a range of cases with increasing Rayleigh numbers. This transition, documented since early investigations [79], has recently garnered attention from researchers exploring solar and stellar convection dynamics [194, 111]. Given buoyancy's anticipated dominance in the force balance of solar convection, the results presented earlier for a moderate Rayleigh number may appear transient. However, the critical Rayleigh number (R) for the transition from solar to antisolar rotation is contingent upon the remaining parameter values. For instance, while we observed a transition at $P_r = 0.3$, as depicted in Figure 7.6, no such transition was evident at $P_r = 1$ and $P_r = 5$. The transition's occurrence hinges on factors like the background density stratification parameter (N_ρ), which in our simulations notably deviated from estimates for the solar convection zone. Therefore, we posit that the effects delineated in our work likely persist in regimes characterized by prograde equatorial rotation.

Another noteworthy observation from Figure 7.6 is that although strong buoyancy-driven convection tends towards turbulent states, it alone fails to induce conical differential rotation. In fact, both before and after the transition, the rotation remains predominantly geostrophic in the depicted cases with uniform profiles.

Effects of self-sustained magnetic fields. Until now, we have refrained from discussing the impacts of self-sustained magnetic fields on convective flow and associated differential rotation. Figures 7.7 and 7.8 offer a comparison between a non-magnetic convection simulation and a dynamo solution obtained with identical parameter values, featuring a magnetic Prandtl number (Pm) of 10 to ensure the persistence of a non-decaying magnetic field. While dynamos with lower Pm values are included in our table, we selected this simulation because it produces a

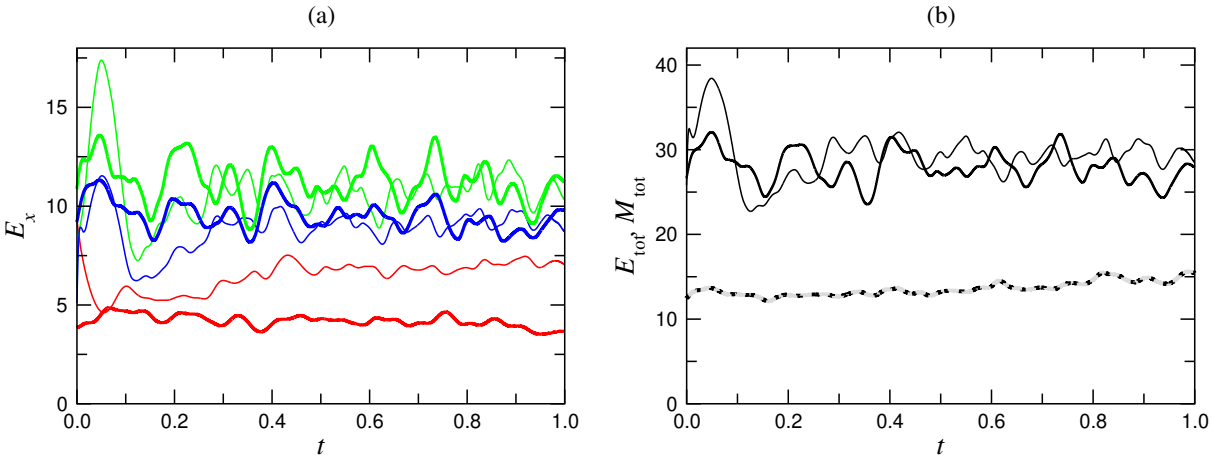

Figure 7.7: Time series of energy densities of the self-sustained dynamo case first shown in Figure 7.3E (thick lines) against non-magnetic convection under identical parameters (thin lines labeled E′ in Figure 7.8). (**a**) Selected kinetic energy densities. The equatorially symmetric components of the mean toroidal ($\bar{E}_t^s$ (red)), fluctuating poloidal ($\check{E}_p^s$ (green)) and fluctuating toroidal ($\check{E}_t^s$ (blue)) energies. (**b**) Total kinetic energy densities and total magnetic energy density for the dynamo case (grey dotted line).

conical differential rotation profile for both uniform and non-uniform cases. The differential rotation profile becomes more solar-like when non-uniform profiles are considered, making this simulation particularly relevant for exploring these dynamics. Figure 7.7 specifically presents a direct comparison of the kinetic energy components between the two cases.

The principal effect of the self-generated and self-sustained magnetic field in the dynamo simulation is a reduction in the kinetic energy component associated with zonal flow—approximately 25% in this instance. This reduction arises because, even in this notably diffusive scenario, the poloidal components of the magnetic field exhibit a degree of "freezing" in the fluid, opposing and decelerating zonal jets. Zonal flow, being non-convective in nature, distorts and suppresses convective motions. Thus, with the magnetic field now impeding zonal flow, the mean and fluctuating poloidal and toroidal kinetic energies experience slight increases, though not to a significant extent.

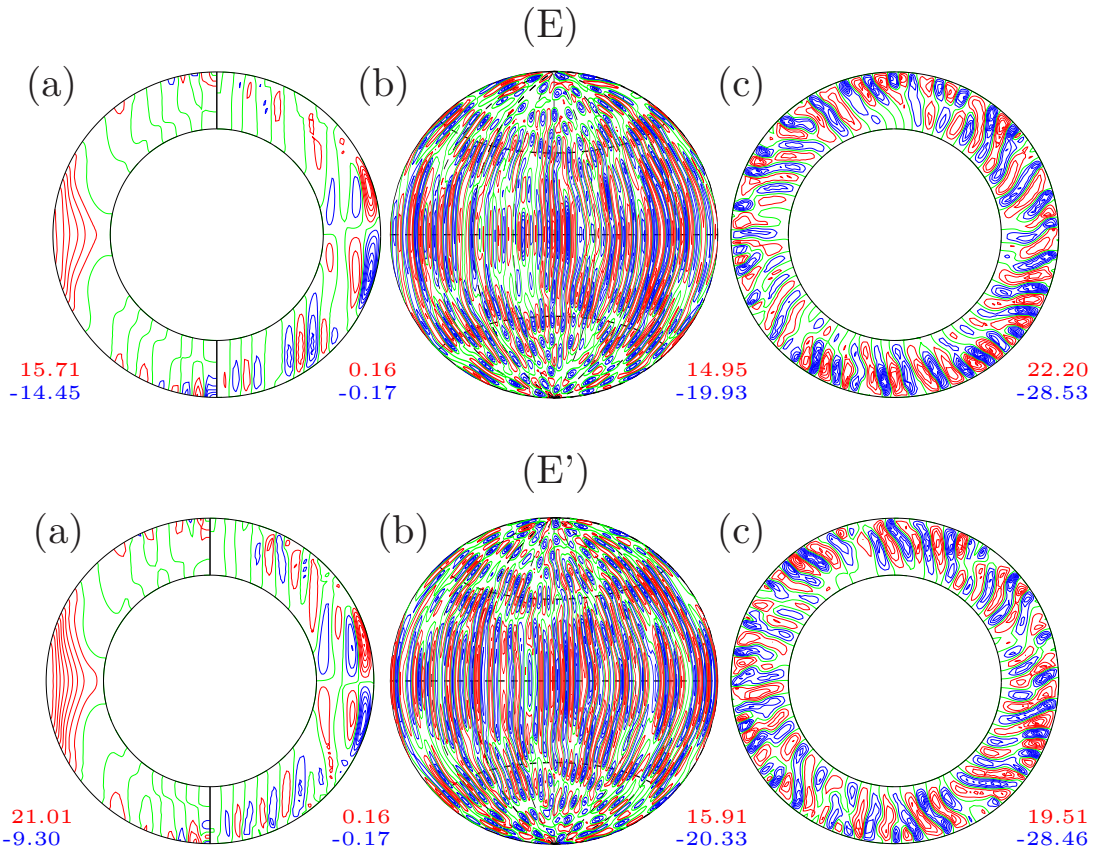

Figure 7.8: Comparison of a dynamo solution (E) and a non-magnetic convection solution (E′) under identical parameter values. The dynamo is the same case (E) plotted in Figures 7.3–7.5 and 7.7. The contour plots in (**a**–**c**) show the same solution components as those plotted in (**a**–**c**) of Figure 7.4, plus the differential rotation in the left half of (**a**).

Furthermore, Figure 7.7 underscores the chaotic temporal behavior of the solutions, while Figure 7.8 provides a side-by-side comparison of the spatial structure between the non-magnetic and dynamo solutions. Beyond a slight disparity in differential rotation isocontours, which are marginally more compressed in the non-magnetic scenario, the remaining flow components appear nearly identical, including dominant azimuthal, radial, and latitudinal wave numbers and typical length scales. Consequently, we deduce that the self-sustained magnetic field does not substantially alter convective and zonal flows. We have observed this behavior in other simulations as well, where the magnetic field, despite being non-decaying, does not substantially alter the overall flow dynamics due to the relatively minor role of the Lorentz force. These solutions are arguably not strong-field solutions, as the Lorentz force plays only a minor role in shaping the dynamics. This could be attributed to the relatively weak magnetic field strength in

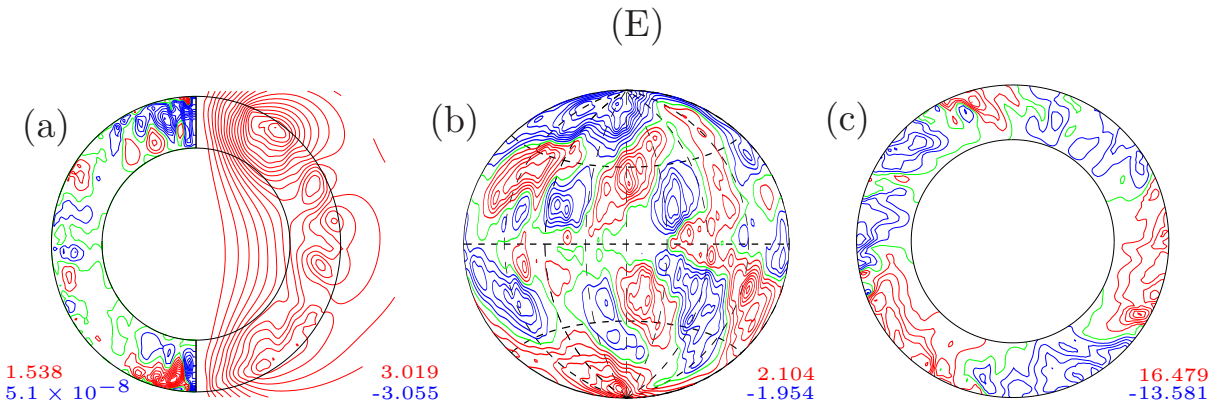

Figure 7.9: Magnetic field components of the dynamo solution (E) of Figure 7.8. (**a**) Toroidal and poloidal field strength in the meridional plane to the left and right, respectively. (**b**) Radial magnetic field continued slightly above the shell surface ($B_r(r = 1.2)$) (**c**) Field lines in a plane at a constant latitude of $\theta = 30°$, parallel to the equator.

these simulations, which does not significantly impact the flow structure. Additionally, Figure 7.9 illustrates the morphology of the generated magnetic field. The dynamo solution exhibits a prevailing dipolar symmetry in the polar regions, featuring extensive patches of magnetic field with opposite polarity situated at the north and south "caps" of the spherical shell, which persist over time. These polar magnetic fluxes are also evident in azimuthally averaged toroidal and poloidal field lines plotted in the meridional plane. In the vicinity of the equatorial plane up to mid latitudes, the magnetic field adopts a more complex quadrupolar symmetry, characterized by magnetic field patches of the same polarity across the equatorial plane. These quadrupolar patches predominantly exhibit an azimuthal wave number ($m = 3$) and undergo longitudinal drifts and latitudinal oscillations.

While this model does not precisely replicate the solar dynamo, notable similarities exist, such as the overall dipolar structure, indications of cyclicity and active longitudes, reminiscent of those observed on the Sun [215]. The oscillation period is directly linked to the amplitude of the differential rotation [32].

In the case of non-uniform simulations, the magnetic field strength is relatively weak, and thus, we cannot definitively claim its effect on the differential rotation profile. In future research, we plan to explore parameter spaces where the magnetic field is strong enough in the non-uniform case to allow us to assess its impact on the differential rotation profile. However, in the uniform case, we observed that the magnetic field did not significantly alter the differential rotation profile, while non-uniform diffusivity profiles did help to produce solar-like rotation profiles.

When we initially ran the simulations, we did not anticipate that the magnetic field strength would be so weak in the non-uniform cases. As a result, further investigation is needed to understand the role of the magnetic field on differential rotation. If the magnetic field indeed has no substantial effect on the differential rotation profile, future studies could focus on differential rotation in purely hydrodynamic (HD) simulations. Additionally, it is important to note that in these simulations, we did not use a radially dependent resistivity profile, as explored by [106], but this could be another avenue for future investigation.

7.5 Concluding remarks

In this study, we embarked on an initial exploration of the effects of non-uniform viscosity and entropy diffusivity on the differential rotation engendered by convection in rotating spherical shells. Our objective was to address the so-called convective conundrum, wherein many models of the solar dynamo fail to faithfully replicate the solar differential rotation profile as measured through helioseismology. Our approach centered on probing a select yet illustrative portion of the parameter space to establish a correlation between non-uniform viscosity and entropy diffusivity and differential rotation.

By maintaining all parameter values constant except for the Prandtl number and Magnetic Prandtl number, our primary finding indicates that Prandtl numbers slightly exceeding unity ($P_r = 5$ in our case) yield a differential rotation profile markedly more aligned with observed profiles compared to cases with lower Prandtl numbers or uniform profiles of viscosity and entropy diffusivity. While agreement is notable from the equatorial region up to mid latitudes, discrepancies persist towards the poles, where both simulations and observations exhibit lesser precision.

For non-uniform viscosity and entropy diffusivity profiles, the differential rotation profile is intricately linked to the presence of heightened convection at the poles for higher P_r values. Elevated entropy levels at the poles induce a non-trivial entropy gradient in θ, pivotal in disrupting the Taylor–Proudman state through the thermal wind balance. Consequently, conical rather than cylindrical profiles of differential rotation are favored in the presence of sufficiently pronounced radially non-uniform viscosity and entropy diffusivity profiles. Notably, spherically symmetric radial non-uniformity can instigate latitudinal non-uniformity, developing self-consistently—an observation contrasting with prior studies [142].

The finding is that a large Prandtl number unexpectedly improves agreement with observations is noteworthy. While solar values of P_r are anticipated to be minuscule based on molecular estimates [218], turbulent mixing suggests values around unity. This apparent agreement may stem, in part, from the specific region of parameter space examined, tailored to capture the presumed force balance in the solar convection zone while ensuring computational feasibility. Notably, the high P_r results may suggest a distinct approach to navigating the relevant parameter regime, focusing on maintaining appropriate force balances, similar to the strategies employed in analogous studies of the geodynamo [210, 151]. This perspective highlights the potential for more effective exploration of parameter space, allowing for the identification of conditions that yield solar-like dynamics.

Our results underscore the possibility of achieving solar-like differential rotation in simulations, laying a strong foundation for comprehensive parameter sweeps encompassing both fundamental non-dimensional parameters and profiles of non-uniform viscosity and entropy diffusivity. This avenue promises deeper insights into the interplay between differential rotation and the dynamo mechanism, warranting further investigation.

Chapter 8

Conclusion

In this thesis, we have explored the dynamics of convection-driven dynamos in rotating spherical shells, addressing fundamental questions that deepen our understanding of celestial dynamics:

- Investigating the relative importance of the helicity and cross-helicity electromotive dynamo effects for self-sustained magnetic field generation by chaotic thermal convection in rotating spherical shells as a function of shell thickness. This research has deepened the understanding of the Earth's geodynamo and the solar dynamo by elucidating the roles of helicity and cross-helicity effects in these systems. Specifically, it has highlighted how the thicker convective shell in Earth's outer fluid layer promotes large-scale columnar structures and helicity generation, contributing to the dominant, rarely reversing dipole. Conversely, the thinner convection zone in the Sun leads to less regular vorticity structures, making the cross-helicity effect more significant and resulting in a regular periodic cycle. This distinction, along with the exploration of bistability and its impact on magnetic field polarity reversals, provides new insights into the different dynamo mechanisms at play in these celestial bodies.

- Exploring the behavior of global magnetic helicity in self-consistent spherical dynamos, revealing insights into how it describes the linkage between poloidal and toroidal magnetic fields. The study also highlights the potential implications for understanding global magnetic field reversals, particularly in the context of maintaining the preferred state of this linkage during such events.
- Analyzing the impact of radially non-uniform viscosity and entropy diffusivity on differential rotation and convective flow patterns in density-stratified rotating spherical fluid shells, highlighting their role in deviating from observed solar differential rotation geostrophy and addressing the convection conundrum in solar physics.

These findings collectively advance our understanding of celestial dynamics and provide a foundation for future research aimed at unraveling the complexities of geophysical and astrophysical processes. Chapters 5, 6, and 7 each examine distinct phenomena and their implications. This concluding chapter synthesizes the key findings from these investigations and suggests directions for future research.

8.1 Summary of findings

8.1.1 Effects of shell thickness on cross-helicity generation in convection-driven spherical dynamos (Chapter 5)

Thermal convection, influenced by rotation, is widespread in celestial bodies' interiors and atmospheres, often involving plasmas or metals. This vigorous convection leads to large-scale electric currents and generates the magnetic fields typical of these cosmic objects. In Chapter 5, we discussed the relative importance of helicity (α-effect) and cross-helicity (γ-effect) effects in

mean-field dynamo theory for magnetic field generation and amplification. The study includes over 40 detailed numerical simulations of self-sustained dynamos, driven by thermal convection in rotating spherical fluid shells with varying thickness ratios, using the Boussinesq approximation for nonlinear magnetohydrodynamic equations with stress-free boundary conditions. The key findings are as follows:

1. Critical parameter values for onset of convection. We numerically determined the critical values for the onset of convection as a function of the shell radius ratio (η). These results show that as the shell thickness decreases, the critical Rayleigh number and critical frequency for the onset of thermal convection also decrease, while the critical wave number increases. Determining these critical values is essential because variations in shell thickness directly impact the dynamics of thermal convection. By establishing these parameters, we ensure that our simulations accurately capture the transition from non-conductive to conductive behavior across different shell thicknesses. These findings align well with theoretical predictions and provide essential insights into the behavior of convection in rotating spherical shells, which is crucial for accurately modelling the geodynamo and solar dynamo.

2. Bistability and coexistence of dynamo attractors. Our simulations revealed the coexistence of two distinct dynamo attractors—mean-field dipolar (**MD**) and fluctuating dipolar (**FD**)—across a range of shell thicknesses ($\eta \in [0.25, 0.6]$). This finding demonstrates that multiple dynamo states can exist within the same physical system, leading to different magnetic field configurations based on initial conditions. Since this range corresponds to where most celestial dynamos operate, this result is significant as it suggests that the observed magnetic field morphologies of celestial bodies may be dependent on the initial state of the dynamo.

3. Spatial distributions and temporal behavior of electromotive effects. We examined the spatial distributions and time-averaged values of turbulent helicity and cross-helicity electromotive force (EMF) effects. Our findings reveal that in the fluctuating dipolar dynamo regime, the helicity α-effect and the cross-helicity γ-effect exhibit comparable intensities, with their ratio showing little variation across different shell thicknesses. In contrast, within the mean-field dipolar dynamo regime, the helicity α-effect predominates by roughly two orders of magnitude and strengthens as the shell thickness decreases. This highlights the differential roles of these effects in various dynamo regimes.

4. Insights into dynamo mechanisms in solar, stellar and geodynamo systems. Our findings suggest that both dynamo mechanisms play crucial roles in generating the global magnetic field of the Sun, given its fluctuating dipolar nature. Additionally, we observe that the cross-helicity effect could be significant in elucidating dynamo mechanisms in stellar systems. These stellar dynamos may also exhibit a fluctuating dipolar type, differing notably from the solar dynamo, where large-scale magnetic structures may dominate predominantly in one hemisphere.

Given that the geodynamo operates as a mean-field dipolar system, our findings suggest that the helicity effect is particularly notable in this context. Our results indicate that this effect strengthens as the inner solid core expands due to iron freezing. Recent simulations of the geodynamo, focusing on inner core nucleation and growth, highlight distinct phases: earlier stages exhibit weak thermal convection, low magnetic intensity, and non-dipolar field shapes, while later stages show a stronger axial dipole morphology with increasing inner core size. Similarly, our research reveals that fluctuating dipole (**FD**) and multipolar dynamos occur when the shell radius ratio (η) is less than 0.25. Notably, our **FD** solutions, despite having lower magnetic field intensity compared to corresponding mean-dipole (**MD**) dynamos, exhibit vigorous convection and can be characterized as strong-field dynamos. Moreover, we observe that for η greater than 0.25, both **MD** and **FD** dynamos coexist, a discrepancy possibly stemming from

significant variations in thermal and velocity boundary conditions between our model and those used in previous studies. It's crucial to note that while parameters in earlier studies are influenced by thermochemical evolution models and vary with inner core size, our study maintains fixed parameter values aside from η.

Future directions. In future research, exploring the helicity and cross-helicity effects using the broader anelastic approximation of the governing equations could provide deeper insights. Additionally, there is a need to investigate how the dynamic balance among the components of the electromotive force influences various aspects of dynamo behavior, such as the transition between mean-dipole **MD** and fluctuating dipole **FD** dynamos. Addressing these questions will enhance our understanding of dynamo mechanisms across different celestial bodies and their magnetic field generation processes.

8.1.2 A study of global magnetic helicity in self-consistent spherical dynamos (Chapter 6)

In Chapter 6, we discussed three dynamo solutions within rotating spherical shells to investigate the behavior of magnetic helicity. We adopted a well-established Boussinesq MHD model for convection-driven dynamos in rotating spherical shells and examined dynamo solutions of increasing complexity: steady (Case 1), periodically-reversing (Case 2), and aperiodically-reversing (Case 3). Although magnetic helicity is not conserved in the latter two cases, it still provides crucial information about the magnetic field in all scenarios. Our findings demonstrate that magnetic helicity effectively describes the linkage between toroidal and poloidal magnetic fields. For the cases involving reversals, we detailed how magnetic helicity correlates with the reversal of both poloidal and toroidal magnetic fields, showing that variations in the surface magnetic helicity density can signal the onset of reversals. The key findings are as follows:

1. Magnetic helicity and reversals. Magnetic helicity is not strictly conserved in the simulations studied, thus reversals cannot be causally linked to magnetic helicity. The results suggest preferred states of global magnetic linkage for specific dynamo solutions. When the dynamo deviates from these states, it can return through a global reversal. Magnetic helicity, even if not causing reversals, serves as a clear indicator of the global poloidal-toroidal linkage associated with reversals. Surface maps of magnetic helicity density, which can be measured in stellar observations, indicate the onset of reversals. This finding is robust across dynamo solutions with varying reversal mechanisms.

2. Comparison with mean-field models: The main focus of magnetic helicity in dynamos has been its role in the α-effect in mean-field models, assuming a scale separation of magnetic helicity. The simulations focus mainly on large-scale magnetic helicity, which alone is not conserved, aligning qualitatively with some mean-field study results. In a Babcock-Leighton α-effect based dynamo model, helicities tend to be opposite of the preferred hemispheric trends at the start of cycles, with temporary changes in the helicity hemisphere pattern observed in actual observations.

3. Hemispheric imbalances. The interpretation of the results in terms of "preferred" states of linkage offers a new perspective on the origin of the hemisphere rule of magnetic helicity. The findings suggest that imbalances in this rule can arise from changes in the linkage of large-scale fields, which are larger than the small-scale fields considered in mean-field models. Further research is needed in this area, but understanding helicity in terms of toroidal/poloidal linkage could help refine existing mean-field models that aim to explain hemisphere imbalances.

Future directions. In future research, to achieve a closer comparison with solar models and observations, transitioning from Boussinesq MHD to studying global magnetic helicity in anelastic models is recommended. This approach will allow for more accurate replication of solar parameters and those of other specific stars.

8.1.3 Differential rotation in convecting spherical shells with non-uniform viscosity and entropy diffusivity (Chapter 7)

In Chapter 7, we have conducted an initial exploration of the impact of non-uniform viscosity and entropy diffusivity on differential rotation generated by convection in rotating spherical shells. Our investigation aimed to address the "convective conundrum," where many models of the solar dynamo struggle to accurately reproduce the observed profile of solar differential rotation measured using helioseismology. The key findings are as follows:

1. Impact of Prandtl number. We focused on a specific region of the parameter space and found that higher values of the Prandtl number ($P_r = 5$) significantly improve the agreement of the differential rotation profile with observational data from the equatorial region up to mid-latitudes. However, discrepancies persist towards the poles, where both simulations and observations exhibit lower accuracy.

2. Role of non-uniform profiles. For simulations utilizing non-uniform viscosity and entropy diffusivity profiles, we observed that stronger convection at the poles for higher Prandtl numbers led to an increased entropy gradient in latitude θ. This gradient played a critical role in disrupting the Taylor–Proudman state, favoring conical rather than cylindrical profiles of differential rotation. This development occurred self-consistently due to spherically symmetric radial non-uniformity, contrasting with previous simulations that required imposed latitudinal entropy gradients

3. Surprising influence of Prandtl number on differential rotation. It is somewhat surprising that a large value of the Prandtl number leads to better agreement with observations. While the Prandtl number in the Sun is expected to be very small based on molecular estimates, turbulent mixing suggests values around unity. This agreement may partly result from the chosen parameter space, aimed at capturing the presumed force balance in the solar convection zone, highlighting the importance of accurate force balances over strict adherence to estimated parameter values.

Future directions. The finding that a higher Prandtl number improves agreement with observed differential rotation raises intriguing questions about the role of turbulence and mixing in solar convection zones. Future research should explore a broader range of fundamental non-dimensional parameters and non-uniform viscosity/entropy diffusivity profiles. This exploration will deepen our understanding of how differential rotation influences the dynamo mechanism responsible for solar magnetic fields.

Moreover, extending parameter sweeps beyond the confines of this initial study could elucidate additional nuances in the relationship between fluid dynamics and magnetic field generation. Investigating the detailed balance of angular momentum transport mechanisms, particularly how processes such as meridional circulation, Reynolds stress, Maxwell stress, mean magnetic

fields, and viscous diffusion contribute to the Sun's angular momentum evolution, will be crucial (as discussed in Chapter 2, section 2.2.1). Such efforts may reveal further insights into the complex interplay between convection, differential rotation, and magnetic field dynamics in both solar and stellar contexts.

8.2 Closing remarks

In this thesis, we have significantly deepened our understanding of the dynamics of convection-driven dynamos in rotating spherical shells. Through detailed investigation, we have uncovered important aspects of how magnetic fields are generated and maintained in celestial bodies, such as the Earth and the Sun.

Our exploration of the helicity and cross-helicity effects has provided new insights into the mechanisms that contribute to the stability or periodicity of magnetic fields in these systems. We have shown that the Earth's thicker convective shell favors large-scale, stable magnetic structures, while the Sun's thinner convection zone leads to more chaotic flows, influencing its regular magnetic cycle.

Moreover, by examining global magnetic helicity, we have shed light on the intricate relationship between poloidal and toroidal fields, offering a new perspective on how reversals of the global magnetic field may occur. The interplay between these fields points to deeper mechanisms that govern magnetic polarity changes, potentially observable at the surface of stars like the Sun.

Additionally, our analysis of the effects of non-uniform viscosity and entropy diffusivity has revealed important deviations from the expected solar differential rotation, addressing long-standing challenges such as the 'convection conundrum.' This work contributes to bridging the gap between theoretical models and observed astrophysical phenomena.

Collectively, these findings not only enhance our understanding of geophysical and astrophysical dynamos but also lay a strong foundation for future research. As we continue to unravel the complexities of celestial magnetic fields and fluid dynamics, the insights gained from this work will serve as a stepping stone for future studies aimed at decoding the behavior of dynamo processes in diverse astrophysical contexts.

Bibliography

[1] M. Ardes, F. H. Busse and J. Wicht. “Thermal convection in rotating spherical shells”. In: *Phys. Earth Planet. Inter.* 99 (1997), pp. 55–67. DOI: 10.1016/S0031-9201(96)03200-1.

[2] Julien Aubert, John A. Tarduno and Catherine L. Johnson. “Observations and Models of the Long-Term Evolution of Earth’s Magnetic Field”. In: 155.1-4 (Aug. 2010), pp. 337–370. DOI: 10.1007/s11214-010-9684-5.

[3] K. Augustson, A.S. Brun and M. et al Miesch. “Grand minima and equatorward propagation in a cycling stellar convective dynamo”. In: *Astrophys J* 809 (2015), p. 149. DOI: 10.1088/0004-637X/809/2/149.

[4] K.C. Augustson, A.S. Brun and J. Toomre. “The magnetic furnace: intense core dynamos in B stars”. In: *Astrophys J* 829.2 (2016), p. 92. DOI: 10.3847/0004-637X/829/2/92.

[5] G. Backus. “A Class of Self-Sustaining Dissipative Spherical Dynamos”. In: *Annals of Physics* 4 (1958), pp. 372–447.

[6] S.L. Baliunas, R.A. Donahue and W.H. et al. Soon. “Chromospheric variations in main-sequence stars. II”. In: *Astrophysical Journal* 438 (1995), p. 269. DOI: 10.1086/175072.

[7] S. Basu, H.M. Antia and D. Narasimha. “Helioseismic Measurement of the Extent of Overshoot Below the Solar Convection Zone”. In: *Mon. Not. R. Astron. Soc.* 267 (1994). Related online version (cited on 15 March 2005): http://adsabs.harvard.edu/cgi-bin/bib_query?1994MNRAS.267..209B, pp. 209–224.

[8] M.A. Berger. “Rigorous new limits on magnetic helicity dissipation in the solar corona”. In: *Geophys. Astrophys. Fluid Dyn.* 30 (1984), pp. 79–104.

[9] M.A. Berger. “Structure and stability of constant-alpha force-free fields”. In: *Astrophys. J., Suppl. Ser.* 59 (1985), pp. 433–444.

[10] M.A. Berger and G.B. Field. “The topological properties of magnetic helicity”. In: *J. Fluid Mech.* 147 (1984), pp. 133–148.

[11] M.A. Berger and G. Hornig. “A generalized poloidal-toroidal decomposition and an absolute measure of helicity”. In: *J. Phys. A Math.* 51 (2018), p. 495501.

[12] A. Bonanno and E. Corsaro. “On the origin of the dichotomy of stellar activity cycles”. In: *Astrophysical Journal Letters* 939.2 (2022), p. L26. DOI: 10.3847/2041-8213/ac9c05. arXiv: 2210.11305 [astro-ph.SR].

[13] S. Boro Saikia, T. Lueftinger and S.V. et al. Jeffers. “Direct evidence of a full dipole flip during the magnetic cycle of a sun-like star”. In: *Astronomy & Astrophysics* 620 (2018), p. L11. DOI: 10.1051/0004-6361/201834347. arXiv: 1811.11671 [astro-ph.SR].

[14] S. Boro Saikia, C.J. Marvin and S.V. et al. Jeffers. “Chromospheric activity catalogue of 4454 cool stars. Questioning the active branch of stellar activity cycles”. In: *Astronomy & Astrophysics* 616 (2018), A108. DOI: 10.1051/0004-6361/201629518. arXiv: 1803.11123 [astro-ph.SR].

[15] S. Braginsky and P.H. Roberts. “Equations governing convection in Earth’s core and the geodynamo”. In: *Geophysical and Astrophysical Fluid Dynamics* 79 (1995), pp. 1–97. DOI: 10.1080/03091929508228992.

[16] A. Brandenburg. “Advances in mean-field dynamo theory and applications to astrophysical turbulence”. In: *J. Plasma Phys.* 84 (2018), p. 735840404.

[17] A. Brandenburg, S. Mathur and T.S. Metcalfe. “Evolution of co-existing long and short period stellar activity cycles”. In: *Astrophysical Journal* 845.1 (2017), p. 79. DOI: 10.3847/1538-4357/aa7cfa. arXiv: 1704.09009 [astro-ph.SR].

[18] A. Brandenburg and K. Subramanian. “Astrophysical magnetic fields and nonlinear dynamo theory”. In: *Physics Reports* 417 (2005), pp. 1–209. DOI: 10.1016/j.physrep.2005.06.005.

[19] B.P. Brown, M.S. Miesch and M.K. et al Browning. “Magnetic cycles in a convective dynamo simulation of a young solar-type star”. In: *Astrophys J* 731 (2011), p. 69. DOI: 10.1088/0004-637X/731/1/69.

[20] T.M. Brown et al. “Inferring the Sun’s internal angular velocity from observed p-mode frequency splittings”. In: *Astrophysical Journal* 343 (1989), pp. 526–546. DOI: 10.1086/167727.

[21] M. K. Browning. “Differential Rotation and Magnetism in Simulations of Fully Convective Stars”. In: *Proc. Int. Astron. Union* 6 (2010), pp. 69–77. DOI: 10.1017/S1743921311017467.

[22] M.K. Browning, M.S. Miesch and A.S. et al Brun. “Dynamo action in the solar convection zone and tachocline: pumping and organization of toroidal fields”. In: *Astrophys J Lett* 648 (2006), pp. L157–L160. DOI: 10.1086/507869.

[23] A. S. Brun, M. S. Miesch and J. Toomre. “Global-Scale Turbulent Convection and Magnetic Dynamo Action in the Solar Envelope”. In: *Astrophys. J.* 614 (2004), pp. 1073–1098. DOI: 10.1086/423835.

[24] A. S. Brun and J. Toomre. “Turbulent Convection under the Influence of Rotation: Sustaining a Strong Differential Rotation”. In: *Astrophys. J.* 570 (2002), pp. 865–885. DOI: 10.1086/339228.

[25] A. S. Brun et al. “Powering Stellar Magnetism: Energy Transfers in Cyclic Dynamos of Sun-like Stars”. In: *Astrophys. J.* 926 (2022), p. 21. DOI: 10.3847/1538-4357/ac469b.

[26] A.S. Brun and M.K. Browning. “Magnetism, dynamo action and the solar-stellar connection”. In: *Living Reviews in Solar Physics* 14 (2017). DOI: 10.1007/s41116-017-0007-8.

[27] A.S. Brun and A. Palacios. “Numerical simulations of a rotating red giant star. I. Three-dimensional models of turbulent convection and associated mean flows”. In: *Astrophys J* 702 (2009), pp. 1078–1097. DOI: 10.1088/0004-637X/702/2/1078.

[28] Edward Crisp Bullard. “The magnetic field within the Earth”. In: *Proceedings of the Royal Society of London. Series A. Mathematical and Physical Sciences* 197.1051 (1949), pp. 433–453.

[29] Edward Crisp Bullard and H Gellman. “Homogeneous dynamos and terrestrial magnetism”. In: *Philosophical Transactions of the Royal Society of London. Series A, Mathematical and Physical Sciences* 247.928 (1954), pp. 213–278.

[30] F. Busse and R. Simitev. “Planetary Dynamos”. In: *Treatise on Geophysics*. Elsevier, 2015, pp. 239–254. DOI: 10.1016/b978-0-444-53802-4.00172-x.

[31] F. Busse and R. Simitev. “Toroidal flux oscillation as possible cause of geomagnetic excursions and reversals”. In: *Phys. Earth Planet. Inter.* 168 (2008), pp. 237–243.

[32] F. Busse and R.D. Simitev. “Parameter dependences of convection-driven dynamos in rotating spherical fluid shells”. In: *Geophys. Astrophys. Fluid Dyn.* 100 (2006), pp. 341–361.

[33] F. H. Busse and R. D. Simitev. “Inertial convection in rotating fluid spheres”. In: *J. Fluid Mech.* 498 (2004), pp. 23–30. DOI: 10.1017/S0022112003006943.

[34] F.H. Busse. “Thermal instabilities in rapidly rotating systems”. In: *J. Fluid Mech.* 44 (1970), p. 441. DOI: 10.1017/S0022112070001921.

[35] F.H. Busse and R. Simitev. “Dynamos driven by convection in rotating spherical shells”. In: *Astr. Nachr.* 326 (2005), p. 231. DOI: 10.1002/asna.200410382.

[36] F.H. Busse and R. Simitev. “Dynamos of giant planets”. In: *Procs. Int. Astr. Union, Symposium S239*. Vol. 2. 2007, p. 467. DOI: 10.1017/S1743921307000920.

[37] F.H. Busse and R. Simitev. “Toroidal flux oscillations as possible causes of geomagnetic excursions and reversals”. In: *Phys. Earth Planet. Inter.* 168 (2008), p. 237.

[38] F.H. Busse and R.D. Simitev. “Dynamos driven by convection in rotating spherical shells”. In: *Astron. Nachrichten* 326 (2005), pp. 231–240. DOI: 10.1002/asna.200410382.

[39] F.H. Busse and R.D. Simitev. “Remarks on some typical assumptions in dynamo theory”. In: *Geophys. Astrophys. Fluid Dyn.* 105 (2011), pp. 234–247.

[40] R. Cameron, M. Dikpati and A. Brandenburg. “The global solar dynamo”. In: *Space Sci. Rev.* 210 (2017), pp. 367–395.

[41] J. Cantarella et al. “The spectrum of the curl operator on spherically symmetric domains”. In: *Phys. Plasma* 7 (2000), pp. 2766–2775.

[42] C. Canuto et al. *Spectral Methods in Fluid Dynamics*. New York: Springer, 1988.

[43] Alberto Carrassi et al. “Data assimilation in the geosciences: An overview of methods, issues, and perspectives”. In: *Wiley Interdisciplinary Reviews: Climate Change* 9.5 (2018), e535.

[44] P. Charbonneau. “Solar Dynamo Theory”. In: *Annual Review of Astronomy and Astrophysics* 52 (2014), pp. 251–290. DOI: 10.1146/annurev-astro-081913-040012.

[45] Paul Charbonneau. “Dynamo models of the solar cycle”. In: *Living Reviews in Solar Physics* 17 (2020), pp. 1–104.

[46] A.R. Choudhuri, P. Chatterjee and D. Nandy. “Helicity of Solar Active Regions from a Dynamo Model”. In: *Astrophys. J. Lett.* 615 (2004), pp. L57–L60.

[47] U. Christensen, P. Olson and G.A. Glatzmaier. “Numerical modelling of the geodynamo: a systematic parameter study”. In: *Geophys. J. Int.* 138 (1999), pp. 393–409. DOI: 10.1046/j.1365-246x.1999.00886.x.

[48] U.R. Christensen and J. Aubert. “Scaling properties of convection-driven dynamos in rotating spherical shells and application to planetary magnetic fields”. In: *Geophysical Journal International* 166 (2006), pp. 97–114. DOI: 10.1111/j.1365-246x.2006.03009.x.

[49] Ulrich R. Christensen and Johannes Wicht. “Numerical dynamo simulations”. In: *Core Dynamics* 8 (2007), pp. 245–282.

[50] Ulrich R. Christensen et al. “A numerical dynamo benchmark”. In: *Physics of the Earth and Planetary Interiors* 128.1-4 (2001), pp. 25–34.

[51] R.S. Coe, L. Hongre and G.A. Glatzmaier. “An examination of simulated geomagnetic reversals from a palaeomagnetic perspective”. In: *Philosophical Transactions of the Royal Society of London, Series A* 358 (2000), pp. 1141–1170. DOI: 10.1098/rsta.2000.0577.

[52] T. Corbard and M.J. Thompson. “The Subsurface Radial Gradient of Solar Angular Velocity from MDI f-mode Observations”. In: *Solar Phys.* 205 (2002). Related online version (cited on 15 March 2005): http://adsabs.harvard.edu/cgi-bin/bib_query?2002SoPh..205..211C, pp. 211–229.

[53] Thomas George Cowling. “The magnetic field of sunspots”. In: *Monthly Notices of the Royal Astronomical Society, Vol. 94, p. 39-48* 94 (1933), pp. 39–48.

[54] G.A. De Wijs et al. “The viscosity of liquid iron at the physical conditions of the Earth’s core”. In: *Nature* 392.6678 (1998), pp. 239–243. DOI: 10.1038/32575.

[55] M. Dikpati and P. Charbonneau. “A Babcock-Leighton Flux Transport Dynamo with Solar-like Differential Rotation”. In: *The Astrophysical Journal* 518 (1999), pp. 508–520. DOI: 10.1086/307269.

[56] Mausumi Dikpati and Peter A. Gilman. “Flux-transport dynamos with α-effect from global instability of tachocline differential rotation: a solution for magnetic parity selection in the Sun”. In: *The Astrophysical Journal* 559.1 (2001), p. 428.

[57] S.B.F. Dorch. “Magnetic activity in late-type giant stars: numerical MHD simulations of non-linear dynamo action in Betelgeuse”. In: *Astron Astrophys* 423 (2004), pp. 1101–1107. DOI: 10.1051/0004-6361:20040435.

[58] E. Dormy et al. “The onset of thermal convection in rotating spherical shells”. In: *Journal of Fluid Mechanics* 501 (2004), pp. 43–70. DOI: 10.1017/s0022112003007316.

[59] P.E. Driscoll. “Simulating 2 Ga of geodynamo history”. In: *Geophysical Research Letters* 43 (2016), pp. 5680–5687. DOI: 10.1002/2016gl068858.

[60] B.R. Durney. “Meridional Motions and the Angular Momentum Balance in the Solar Convection Zone”. In: *Astrophys. J.* 528 (2000), pp. 486–492.

[61] T.L. Jr. Duvall, W.A. Dziembowski and P.R. Goode. “Internal rotation of the Sun”. In: *Nature* 310.5972 (1984), pp. 22–25. DOI: 10.1038/310022a0.

[62] J.R. Elliott, M.S. Miesch and J. Toomre. “Turbulent solar convection and its coupling with rotation: the effect of Prandtl number and thermal boundary conditions on the resulting differential rotation”. In: *Astrophys J* 533.1 (2000), pp. 546–556. DOI: 10.1086/308643.

[63] Walter M Elsasser. “Induction effects in terrestrial magnetism part I. Theory”. In: *Physical Review* 69.3-4 (1946), p. 106.

[64] C. Emeriau-Viard and A.S. Brun. “Origin and evolution of magnetic field in PMS stars: influence of rotation and structural changes”. In: *Astrophys J* 846.1 (2017), p. 8. DOI: 10.3847/1538-4357/aa7b33.

[65] Y. Fan. “Magnetic Fields in the Solar Convection Zone”. In: *Living Rev. Solar Phys.* 1 (2004). URL (cited on 15 March 2005): https://doi.org/10.12942/lrsp-2004-1, lrsp-2004–1.

[66] D. Faraco and S. Lindberg. “Proof of Taylor’s Conjecture on Magnetic Helicity Conservation”. In: *Comm. Math. Phys.* 373 (2019), pp. 707–738.

[67] D. Faraco et al. “On the proof of Taylor’s conjecture in multiply connected domains”. In: *Appl. Math. Lett.* 124 (2022), p. 107654.

[68] N.A. Featherstone, M.K. Browning and A.S. et al Brun. “Effects of fossil magnetic fields on convective core dynamos in A-type stars”. In: *Astrophys J* 705.1 (2009), pp. 1000–1018. DOI: 10.1088/0004-637X/705/1/1000.

[69] N.A. Featherstone, P.V.F. Edelmann, R. Gassmoeller et al. *Rayleigh 1.1.0*. https://doi.org/10.5281/zenodo.6522806. 2022.

[70] Nicholas A. Featherstone and Bradley W. Hindman. “The Emergence of Solar Supergranulation as a Natural Consequence of Rotationally Constrained Interior Convection”. In: *The Astrophysical Journal Letters* 830.1 (Oct. 2016), p. L15. DOI: 10.3847/2041-8205/830/1/L15.

[71] M. French et al. “Ab initio simulations for material properties along the Jupiter adiabat”. In: *Astrophys. J. Suppl. Ser.* 202 (2012), p. 5. DOI: 10.1088/0067-0049/202/1/5.

[72] T. Gastine et al. “From solar-like to antisolar differential rotation in cool stars”. In: *Monthly Notices of the Royal Astronomical Society: Letters* 438.1 (Nov. 2013), pp. L76–L80.

[73] C. F. Gauss. *Allgemeine Theorie des Erdmagnetismus*. Springer, 1877.

[74] M. Ghizaru, P. Charbonneau and P.K. Smolarkiewicz. “Magnetic cycles in global large-eddy simulations of solar convection”. In: *Astrophys J Lett* 715 (2010), pp. L133–L137. DOI: 10.1088/2041-8205/715/2/L133.

[75] P.M. Giles et al. “A Subsurface Flow of Material From the Sun’s Equator to its Poles”. In: *Nature* 390 (1997). Related online version (cited on 15 March 2005): http://adsabs.harvard.edu/cgi-bin/bib_query?1997Natur.390...52G, pp. 52–54.

[76] P.A. Gilman. “Dynamically consistent nonlinear dynamos driven by convection in a rotating spherical shell, II, Dynamos with cycles and strong feedbacks”. In: *Astrophysical Journal Supplement Series* 53 (1983), pp. 243–268.

[77] P.A. Gilman. “Nonlinear dynamics of Boussinesq convection in a deep rotating spherical shell. I”. In: *Geophys Astrophys Fluid Dyn* 8 (1977), pp. 93–135. DOI: 10.1080/03091927708240373.

[78] P.A. Gilman and M. Dikpati. “Analysis of Instability of Latitudinal Differential Rotation and Toroidal Field in the Solar Tachocline using an MHD shallow water model: I. Instability”. In: (2002).

[79] P.A. Gilman and P. Foukal. “Angular velocity gradients in the solar convection zone”. In: *Astrophys. J.* 229 (1979), pp. 1175–1184. DOI: 10.1086/157056.

[80] P.A. Gilman and J. Miller. “Dynamically consistent nonlinear dynamos driven by convection in a rotating spherical shell”. In: *Astrophysical Journal Supplement* 46 (1981), pp. 211–238.

[81] G. A. Glatzmaier and P. A. Gilman. “Compressible convection in a rotating spherical shell. IV - Effects of viscosity, conductivity, boundary conditions, and zone depth”. In: *Astrophys. J. Suppl. Ser.* 47 (1981), p. 103. DOI: 10.1086/190753.

[82] G. A. Glatzmaier and P. H. Roberts. “A three-dimensional convective dynamo solution with rotating and finitely conducting inner core and mantle”. In: *Physics of the Earth and Planetary Interiors* 91 (1995), pp. 63–75.

[83] G. A. Glatzmaier and P. H. Roberts. “A three-dimensional self-consistent computer simulation of a geomagnetic field reversal”. In: *Nature* 377 (1995), pp. 203–209.

[84] G.A. Glatzmaier. “Numerical simulations of stellar convective dynamos. II - Field propagation in the convection zone”. In: *Astrophys J* 291 (1985), pp. 300–307. DOI: 10.1086/163069.

[85] G.A. Glatzmaier and P.H. Roberts. “A three-dimensional convective dynamo solution with rotating and finitely conducting inner core and mantle”. In: *Physics of the Earth and Planetary Interiors* 91 (1995), pp. 63–75.

[86] G.A. Glatzmaier et al. “The role of the Earth’s mantle in controlling the frequency of geomagnetic reversals”. In: *Nature* 401 (1999), pp. 885–890. DOI: 10.1038/44776.

[87] Gary A Glatzmaier and Paul H Roberts. “An anelastic evolutionary geodynamo simulation driven by compositional and thermal convection”. In: *Physica D: Nonlinear Phenomena* 97.1-3 (1996), pp. 81–94.

[88] D. Gubbins and R.S. Coe. “Longitudinally confined geomagnetic reversal paths from nondipolar transition fields”. In: *Nature* 362 (1993), pp. 51–53. DOI: 10.1038/362051a0.

[89] G. Guerrero et al. “Differential rotation in solar-like stars from global simulations”. In: *The Astrophysical Journal* 779 (2013), p. 176. DOI: 10.1088/0004-637X/779/2/176.

[90] Parag Gupta, David MacTaggart and Radostin D Simitev. “Differential rotation in convecting spherical shells with non-uniform viscosity and entropy diffusivity”. In: *Fluids* 8.11 (2023), p. 288.

[91] Parag Gupta, Radostin D Simitev and David MacTaggart. “A study of global magnetic helicity in self-consistent spherical dynamos”. In: *Geophysical & Astrophysical Fluid Dynamics* 116.5-6 (2022), pp. 521–536.

[92] D.A. Haber et al. “Evolving Submerged Meridional Circulation Cells Within the Upper Convection Zone Revealed by Ring-Diagram Analysis”. In: *Astrophys. J.* 570 (2002). Related online version (cited on 15 March 2005): http://adsabs.harvard.edu/cgi-bin/bib_query?2002ApJ...570..855H, pp. 855–864.

[93] F. Hamba. “Turbulent dynamo effect and cross helicity in magnetohydrodynamic flows”. In: *Physics of Fluids A: Fluid Dynamics* 4 (1992), pp. 441–450. DOI: 10.1063/1.858314.

[94] Shravan M Hanasoge, Thomas L Duvall Jr and Katepalli R Sreenivasan. “Anomalously weak solar convection”. In: *Proceedings of the National Academy of Sciences* 109.30 (2012), pp. 11928–11932.

[95] D. H. Hathaway. “The Solar Cycle”. In: *Living Reviews in Solar Physics* 12.1 (2015), p. 4.

[96] David H. Hathaway et al. “The Sun’s Photospheric Convection Spectrum”. In: *The Astrophysical Journal* 811.2 (Sept. 2015), p. 105. DOI: 10.1088/0004-637X/811/2/105.

[97] G. Hawkes and M. Berger. “Magnetic helicity as a predictor of the solar cycle”. In: *Solar Phys.* 293 (2018), pp. 1–25.

[98] Alfred Herzenberg. “Geomagnetic dynamos”. In: *Philosophical Transactions of the Royal Society of London. Series A, Mathematical and Physical Sciences* 250.986 (1958), pp. 543–583.

[99] Bradley W Hindman, Nicholas A Featherstone and Keith Julien. “Morphological classification of the convective regimes in rotating stars”. In: *The Astrophysical Journal* 898.2 (2020), p. 120.

[100] Rainer Hollerbach and Chris A Jones. “A geodynamo model incorporating a finitely conducting inner core”. In: *Physics of the earth and planetary interiors* 75.4 (1993), pp. 317–327.

[101] H. Hotta and K. Kusano. “Solar differential rotation reproduced with high-resolution simulation”. In: *Nat Astron* 5 (2021), pp. 1100–1102. DOI: 10.1038/s41550-021-01459-0. URL: https://doi.org/10.1038/s41550-021-01459-0.

[102] H. Hotta, M. Rempel and T. Yokoyama. “High-resolution calculation of the solar global convection with the reduced speed of sound technique. II. Near surface shear layer with the rotation”. In: *Astrophysical Journal* 798 (2015), p. 51. DOI: 10.1088/0004-637X/798/1/51. arXiv: 1410.7093 [astro-ph.SR].

[103] H. Hotta et al. “Dynamics of solar large-scale flows”. In: *arXiv preprint* 2023 (2023). eprint: 2307.06481. URL: https://doi.org/10.48550/ARXIV.2307.06481.

[104] R. Howe. “Solar Interior Rotation and its Variation”. In: *Living Reviews in Solar Physics* 6 (2009), p. 1. DOI: 10.12942/lrsp-2009-1.

[105] C. Jones et al. “Anelastic convection-driven dynamo benchmarks”. In: *Icarus* 216 (2011), pp. 120–135. DOI: 10.1016/j.icarus.2011.08.014.

[106] C. A. Jones. “A Dynamo Model of Jupiter’s Magnetic Field”. In: *Icarus* 241 (2014), pp. 148–159.

[107] C.A. Jones. “8.05 - Thermal and Compositional Convection in the Outer Core”. In: *Treatise on Geophysics (Second Edition)*. Ed. by G. Schubert. Elsevier, 2015, pp. 115–159. DOI: https://doi.org/10.1016/B978-0-444-53802-4.00075-1.

[108] C.A. Jones, A.M. Soward and A.I. Mussa. “The onset of thermal convection in a rapidly rotating sphere”. In: *Journal of Fluid Mechanics* 405 (2000), pp. 157–179. DOI: 10.1017/s0022112099007235.

[109] A. Kageyama, M. Ochi and T. Sato. “Flip-flop transitions of the magnetic intensity and polarity reversals in the magnetohydrodynamic dynamo”. In: *Physical Review Letters* 82.26 (1999), pp. 5409–5412. DOI: 10.1103/PhysRevLett.82.5409.

[110] A. Kageyama, T. Sato and the Complexity Simulation Group. “Computer simulation of a magnetohydrodynamic dynamo, II”. In: *Physics of Plasmas* 2 (1995), pp. 1421–1431.

[111] P. J. Käpylä. “Transition from anti-solar to solar-like differential rotation: Dependence on Prandtl number”. In: *Astron. Astrophys.* 669 (2023), A98. DOI: 10.1051/0004-6361/202244395.

[112] P.J. Käpylä, M.J. Käpylä and A. Brandenburg. “Confirmation of bistable stellar differential rotation profiles”. In: *Astronomy & Astrophysics* 570 (2014), A43. arXiv: 1401.2981 [astro-ph.SR].

[113] P.J. Käpylä, M.J. Korpi and A. et al Brandenburg. “Convective dynamos in spherical wedge geometry”. In: *Astron Nachr* 331 (2010), p. 73. DOI: 10.1002/asna.200911252.

[114] P.J. Käpylä, M.J. Mantere and A. Brandenburg. “Cyclic magnetic activity due to turbulent convection in spherical wedge geometry”. In: *Astrophys J Lett* 755 (2012), p. L22. DOI: 10.1088/2041-8205/755/1/L22.

[115] B. B. Karak et al. “Magnetically controlled stellar differential rotation near the transition from solar to anti-solar profiles”. In: *Astron. Astrophys.* 576 (2015), A26. DOI: 10.1051/0004-6361/201424521.

[116] J.S. Katayama, M. Matsushima and Y. Honkura. “Some characteristics of magnetic field behavior in a model of MHD dynamo thermally driven in a rotating spherical shell”. In: *Physics of the Earth and Planetary Interiors* 111 (1999), pp. 141–159. DOI: 10.1016/S0031-9201(98)00109-1.

[117] H. Kitauchi and S. Kida. “Intensification of magnetic field by concentrate-and-stretch of magnetic flux lines”. In: *Physics of Fluids* 10.2 (1998), pp. 457–468. DOI: 10.1063/1.869576.

[118] O. Kochukhov. “Magnetic fields of M dwarfs”. In: *Astronomy & Astrophysics Reviews* 29.1 (2021), p. 1. DOI: 10.1007/s00159-020-00130-3. arXiv: 2011.01781 [astro-ph.SR].

[119] O. Kochukhov, M.J. Mantere and T. et al. Hackman. “Magnetic field topology of the RS CVn star II Pegasi”. In: *Astronomy & Astrophysics* 550 (2013), A84. DOI: 10.1051/0004-6361/201220432. arXiv: 1301.1680 [astro-ph.SR].

[120] Masaru Kono and Paul H Roberts. “Recent geodynamo simulations and observations of the geomagnetic field”. In: *Reviews of Geophysics* 40.4 (2002), pp. 4–1.

[121] A.G. Kosovichev. “Helioseismic Constraints on the Gradient of Angular Velocity at the Base of the Solar Convection Zone”. In: *Astrophys. J.* 469 (1996), pp. L61–L64. DOI: 10.1086/310253.

[122] F. Krause and K.H. Raedler. *Mean-field magnetohydrodynamics and dynamo theory*. Pergamon, 1980.

[123] S Kumar and Paul Harry Roberts. “A three-dimensional kinematic dynamo”. In: *Proceedings of the Royal Society of London. A. Mathematical and Physical Sciences* 344.1637 (1975), pp. 235–258.

[124] M. Landeau, J. Aubert and P. Olson. “The signature of inner-core nucleation on the geodynamo”. In: *Earth and Planetary Science Letters* 465 (2017), pp. 193–204. DOI: 10.1016/j.epsl.2017.02.004.

[125] SR Lantz and Y Fan. “Anelastic magnetohydrodynamic equations for modeling solar and stellar convection zones”. In: *The Astrophysical Journal Supplement Series* 121.1 (1999), p. 247.

[126] J. Larmor. “How could a rotating body such as the Sun become a magnet?” In: *Reports of the British Association* 87 (1919), pp. 159–160.

[127] J. W. Lord et al. “The Role of Subsurface Flows in Solar Surface Convection: Modeling the Spectrum of Supergranular and Larger Scale Flows”. In: *The Astrophysical Journal* 793.1 (2014), p. 24. DOI: 10.1088/0004-637X/793/1/24.

[128] W. Lowrie. “The Geomagnetic Dynamo”. In: *The Earth’s Magnetic Field*. Oxford University Press, June 2023, pp. 63–78. ISBN: 9780191953729. DOI: 10.1093/oso/9780192862679.003.0004. URL: http://dx.doi.org/10.1093/oso/9780192862679.003.0004.

[129] K. Lund et al. “Field linkage and magnetic helicity density”. In: *Mon. Notices Royal Astron. Soc.* 502 (2021), pp. 4903–4910.

[130] K. Lund et al. “Measuring stellar magnetic helicity density”. In: *Mon. Notices Royal Astron. Soc.* 493 (2020), pp. 1003–1012.

[131] J. Mabuchi, Y. Masada and A. Kageyama. “Differential rotation in magnetized and non-magnetized stars”. In: *Astrophys J* 806 (2015), p. 10. DOI: 10.1088/0004-637X/806/1/10.

[132] D. MacTaggart and A. Hillier. *Topics in magnetohydrodynamic topology, reconnection and stability theory*. Springer, 2020.

[133] D. MacTaggart et al. “Magnetohydrostatic modelling of stellar coronae”. In: *Monthly Notices RAS* 456 (2015), pp. 767–774. DOI: 10.1093/mnras/stv2714.

[134] Y. Masada, T. Takiwaki and K. Kotake. “Convection and dynamo in newly born neutron stars”. In: *Astrophys J* 924.2 (2022), p. 75. DOI: 10.3847/1538-4357/ac34f6.

[135] J.F. Mather and R.D. Simitev. “Regimes of thermo-compositional convection and related dynamos in rotating spherical shells”. In: *Geophys. Astrophys. Fluid Dyn.* 115 (2020), pp. 61–84. DOI: 10.1080/03091929.2020.1762875.

[136] L. I. Matilsky, B. W. Hindman and J. Toomre. “Revisiting the Sun’s Strong Differential Rotation along Radial Lines”. In: *The Astrophysical Journal* 898 (2020), p. 111. DOI: 10.3847/1538-4357/ab9ca0.

[137] H. Matsui et al. “Performance benchmarks for a next generation numerical dynamo model”. In: *Geochem. Geophys.* 17 (2016), pp. 1586–1607.

[138] S.P. Matt, O. Do Cao and B.P. et al. Brown. “Convection and differential rotation properties of G and K stars computed with the ASH code”. In: *Astronomische Nachrichten* 332 (2011), p. 897. DOI: 10.1002/asna.201111624. arXiv: 1111.5585 [astro-ph.SR].

[139] R. T. Merrill, M. W. McElhinny and P. L. McFadden. *The Magnetic Field of the Earth: Paleomagnetism, the Core, and the Deep Mantle*. Vol. 63. Academic Press, 1998.

[140] L. Mestel. *Stellar Magnetism*. Vol. 154. Oxford University Press, 2012.

[141] M. S. Miesch. “Large-Scale Dynamics of the Convection Zone and Tachocline”. In: *Living Reviews in Solar Physics* 2 (2005), p. 1. DOI: 10.12942/lrsp-2005-1.

[142] M. S. Miesch, A. S. Brun and J. Toomre. “Solar Differential Rotation Influenced by Latitudinal Entropy Variations in the Tachocline”. In: *The Astrophysical Journal* 641 (2006), pp. 618–625. DOI: 10.1086/499621.

[143] M. S. Miesch et al. “Structure and Evolution of Giant Cells in Global Models of Solar Convection”. In: *Astrophys. J.* 673 (2008), pp. 557–575. DOI: 10.1086/523838.

[144] M.S. Miesch, J.R. Elliott and J. et al Toomre. “Three-dimensional spherical simulations of solar convection. I. Differential rotation and pattern evolution achieved with laminar and turbulent states”. In: *Astrophys J* 532 (2000), pp. 593–615. DOI: 10.1086/308555.

[145] M.S. Miesch and B.W. Hindman. “Gyroscopic pumping in the solar near-surface shear layer”. In: *Astrophysical Journal* 743 (2011), p. 79.

[146] Mark S Miesch. “Large-scale dynamics of the convection zone and tachocline”. In: *Living Reviews in Solar Physics* 2 (2005), pp. 1–139.

[147] Mark S. Miesch, Allan Sacha Brun and Juri Toomre. “Solar Differential Rotation Influenced by Latitudinal Entropy Variations in the Tachocline”. In: *The Astrophysical Journal* 641.1 (Apr. 2006), p. 618. DOI: 10.1086/499621. URL: https://dx.doi.org/10.1086/499621.

[148] Mark S. Miesch et al. “Structure and Evolution of Giant Cells in Global Models of Solar Convection”. In: *The Astrophysical Journal* 673.1 (2008), p. 557.

[149] H. K. Moffatt. *Magnetic Field Generation in Electrically Conducting Fluids*. Cambridge: Cambridge University Press, 1978.

[150] H.K. Moffatt. “The degree of knottedness of tangled vortex lines”. In: *J. Fluid Mech.* 35 (1969), pp. 117–129.

[151] K. Moffatt and E. Dormy. *Self-Exciting Fluid Dynamos*. Cambridge University Press, 2019. DOI: 10.1017/9781107588691.

[152] J Morin et al. “Weak-and strong-field dynamos: from the Earth to the stars”. In: *Monthly Notices of the Royal Astronomical Society: Letters* 418.1 (2011), pp. L133–L137.

[153] N.J. Nelson, B.P. Brown and A.S. et al Brun. “Magnetic wreaths and cycles in convective dynamos”. In: *Astrophys J* 762 (2013), p. 73. DOI: 10.1088/0004-637X/762/2/73.

[154] B. O’Mara et al. “Velocity amplitudes in global convection simulations: The role of the Prandtl number and near-surface driving”. In: *Advances in Space Research* 58 (2016), pp. 1475–1489. DOI: 10.1016/j.asr.2016.03.038.

[155] P.L. Olson, G.A. Glatzmaier and R.S. Coe. “Complex polarity reversals in a geodynamo model”. In: *Earth and Planetary Science Letters* 304 (2011), pp. 168–179. DOI: 10.1016/j.epsl.2011.01.031.

[156] N. Olspert, J.J. Lehtinen and M.J. et al. Käpylä. “Estimating activity cycles with probabilistic methods. II. The Mount Wilson Ca HK data”. In: *Astronomy & Astrophysics* 619 (2018), A6. DOI: 10.1051/0004-6361/201732525. arXiv: 1712.08240 [astro-ph.SR].

[157] M. Ossendrijver. “The Solar Dynamo”. In: *Astron. Astrophys. Rev.* 11 (2003), pp. 287–367.

[158] M.J. Owens and R.J. Forsyth. “The Heliospheric Magnetic Field”. In: *Living Reviews in Solar Physics* 10 (2013). DOI: 10.12942/lrsp-2013-5.

[159] E.N. Parker. “Cosmical magnetic fields. Their origin and their activity”. In: *OUP* (1979).

[160] E.N. Parker. “Hydromagnetic dynamo models”. In: *Astrophys J* 122 (1955), p. 293. DOI: 10.1086/146087.

[161] E.N. Parker. “The dynamo dilemma”. In: *Sol Phys* 110 (1987), pp. 11–21. DOI: 10.1007/BF00148198.

[162] J. Pedlosky. *Geophysical Fluid Dynamics*. Springer, 1987. DOI: 10.1007/978-1-4612-4650-3.

[163] Chaim Leib Pekeris, Y Accad and B Shkoller. “Kinematic dynamos and the Earth’s magnetic field”. In: *Philosophical Transactions of the Royal Society of London. Series A, Mathematical and Physical Sciences* 275.1251 (1973), pp. 425–461.

[164] K Petrovay. “What makes the sun tick?-the origin of the solar cycle”. In: *arXiv preprint astro-ph/0010096* (2000).

[165] A.A. Pevtsov et al. “Magnetic Helicity, Tilt, and Twist”. In: *Space Sci. Rev.* 186 (2014), pp. 285–324.

[166] V.V. Pipin and A.A. Pevtsov. “Magnetic Helicity of the Global Field in Solar Cycles 23 and 24”. In: *Astrophys. J.* 789 (2014), p. 21.

[167] V.V. Pipin and N. Yokoi. “Generation of a Large-scale Magnetic Field in a Convective Full-sphere Cross-helicity Dynamo”. In: *The Astrophysical Journal* 859 (2018), p. 18. DOI: 10.3847/1538-4357/aabae6.

[168] V.V. Pipin et al. “Evolution of magnetic helicity in solar cycle 24”. In: *Astrophys. J. Lett.* 877 (2019), p. L36.

[169] J.-P. Poirier. “Physical properties of the Earth’s core”. In: *Comptes Rendus de l’Académie des Sciences. Série II, Mécanique, Physique, Chimie, Sciences de l’univers, Sciences de la Terre* 318 (1994), pp. 341–350.

[170] R. Raynaud, J. Guilet and H.T. et al Janka. “Magnetar formation through a convective dynamo in protoneutron stars”. In: *Sci Adv* 6.11 (2020), eaay2732. DOI: 10.1126/sciadv.aay2732.

[171] A. Reiners, D. Shulyak and P.J. et al. Käpylä. “Magnetism, rotation, and nonthermal emission in cool stars. Average magnetic field measurements in 292 M dwarfs”. In: *Astronomy & Astrophysics* 662 (2022), A41. DOI: 10.1051/0004-6361/202243251. arXiv: 2204.00342 [astro-ph.SR].

[172] P.H. Roberts. “On the Thermal Instability of a Rotating-Fluid Sphere Containing Heat Sources”. In: *Philos. Trans. R. Soc. Lond. A* 263 (1968), pp. 93–117. DOI: 10.1098/rsta.1968.0007.

[173] P.H. Roberts and M. Stix. “Ac-effect dynamos, by the Buliard-Geflman formalism”. In: *Astron Astrophys* 18 (1972), p. 453.

[174] Paul H Roberts and Eric M King. “On the genesis of the Earth’s magnetism”. In: *Reports on Progress in Physics* 76.9 (2013), p. 096801.

[175] PH Roberts. “Dynamo theory of geomagnetism(Geomagnetism theory of dynamos in homogeneous fluid masses, considering Rikitake self reversing, kinematic and hydromagnetic dynamo problems)”. In: *World magnetic survey 1957-1969.(A 72-12080 02-13) Paris, International Union of Geodesy and Geophysics, 1971*, (1971), pp. 123–131.

[176] G. Rüdiger, M. Küker and R.S. Schnerr. “Cross helicity at the solar surface by simulations and observations”. In: *Astronomy & Astrophysics* 546 (2012), A23. DOI: 10.1051/0004-6361/201219268.

[177] C.T. Russell. “The Magnetosphere”. In: *Annual Review of Earth and Planetary Sciences* 19 (1991), pp. 169–182. DOI: 10.1146/annurev.ea.19.050191.001125.

[178] J.L. van Saders, T. Ceillier and T.S. et al. Metcalfe. “Weakened magnetic braking as the origin of anomalously rapid rotation in old field stars”. In: *Nature* 529 (2016), pp. 181–184. DOI: 10.1038/nature16168. arXiv: 1601.02631 [astro-ph.SR].

[179] G.R. Sarson and C.A. Jones. “A convection driven geodynamo reversal model”. In: *Physics of the Earth and Planetary Interiors* 111 (1999), pp. 3–20. DOI: 10.1016/S0031-9201(98)00119-4.

[180] G.R. Sarson, C.A. Jones and A.W. Longbottom. “Convection driven geodynamo models of varying Ekman number”. In: *Geophysical and Astrophysical Fluid Dynamics* 88 (1998), pp. 225–259. DOI: 10.1080/03091929808203123.

[181] Y. Sasaki et al. “Effects of radial distribution of entropy diffusivity on critical modes of anelastic thermal convection in rotating spherical shells”. In: *Phys. Earth Planet. Inter.* 276 (2018), pp. 36–43. DOI: 10.1016/j.pepi.2017.09.003.

[182] J. Schou et al. “A Comparison of Solar p-mode Parameters from the Michelson Doppler Imager and the Global Oscillation Network Group: Splitting Coefficients and Rotation Inversions”. In: *Astrophys. J.* 567 (2002). Related online version (cited on 15 March 2005): http://adsabs.harvard.edu/cgi-bin/bib_query?2002ApJ...567.1234S, pp. 1234–1249.

[183] J. Schou et al. “Helioseismic Studies of Differential Rotation in the Solar Envelope by the Solar Oscillations Investigation Using the Michelson Doppler Imager”. In: *The Astrophysical Journal* 505 (1998), pp. 390–417. DOI: 10.1086/306146.

[184] C.J. Schrijver and M.L. DeRosa. “Photospheric and Heliospheric Magnetic Fields”. In: *Solar Phys.* 212 (2003). Related online version (cited on 15 March 2005): https://doi.org/10.1023/A:1022932404066, pp. 165–200.

[185] Martin Schrinner et al. “Mean-field concept and direct numerical simulations of rotating magnetoconvection and the geodynamo”. In: *Geophysical & Astro Fluid Dynamics* 101.2 (2007), pp. 81–116.

[186] A. Schuster. “A Critical Examination of the Possible Causes of Terrestrial Magnetism”. In: *Proceedings of the Physical Society of London* 24.1 (1911), p. 121.

[187] L. Silva, J.F. Mather and R.D. Simitev. “The onset of thermo-compositional convection in rotating spherical shells”. In: *Geophys. Astrophys. Fluid Dyn.* 113 (2019), pp. 377–404. DOI: 10.1080/03091929.2019.1640875.

[188] L.A.C. Silva and R.D. Simitev. “Spectral Code For Linear Analysis Of The Onset Of Thermo-Compositional Convection In Rotating Spherical Fluid Shells”. In: (2018). DOI: 10.5281/ZENODO.1307245.

[189] Luis Silva et al. “Effects of shell thickness on cross-helicity generation in convection-driven spherical dynamos”. In: *Fluids* 5.4 (2020), p. 245.

[190] R. Simitev and F. H. Busse. “Patterns of convection in rotating spherical shells”. In: *New J. Phys.* 5 (2003), pp. 97–97. DOI: 10.1088/1367-2630/5/1/397.

[191] R. Simitev and F.H. Busse. “Solar cycle properties described by simple convection-driven dynamos”. In: *Phys. Scr.* 86 (2012), p. 018407.

[192] R. D. Simitev and F. H. Busse. “How Far Can Minimal Models Explain the Solar Cycle?” In: *Astrophysical Journal* 749 (2012), p. 9. DOI: 10.1088/0004-637X/749/1/9.

[193] R. D. Simitev and F. H. Busse. “Prandtl-number dependence of convection-driven dynamos in rotating spherical fluid shells”. In: *J. Fluid Mech.* 532 (2005), pp. 365–388. DOI: 10.1017/S0022112005004398.

[194] R. D. Simitev, A. G. Kosovichev and F. H. Busse. “Dynamo effects near the transition from solar to anti-solar differential rotation”. In: *The Astrophysical Journal* 810 (2015), p. 80. DOI: 10.1088/0004-637X/810/1/80.

[195] R.D. Simitev and F. Busse. “Bistability and hysteresis of dipolar dynamos generated by turbulent convection in rotating spherical shells”. In: *Europhys. Lett.* 85 (2009), p. 19001.

[196] R.D. Simitev and F. Busse. “How far can minimal models explain the solar cycle?” In: *Astrophys. J.* 749 (2012), p. 9.

[197] R.D. Simitev and F.H. Busse. “Bistability and hysteresis of dipolar dynamos generated by turbulent convection in rotating spherical shells”. In: *EPL (Europhysics Letters)* 85 (2009), p. 19001. DOI: 10.1209/0295-5075/85/19001.

[198] R.D. Simitev and F.H. Busse. “Bistable attractors in a model of convection-driven spherical dynamos”. In: *Physica Scripta* 86 (2012), p. 018409. DOI: 10.1088/0031-8949/86/01/018409.

[199] Radostin D Simitev. “Convection and magnetic field generation in rotating spherical fluid shells”. PhD thesis. Universität Bayreuth, 2004.

[200] P.K. Smolarkiewicz and P. Charbonneau. “EULAG, a computational model for multiscale flows: an MHD extension”. In: *Journal of Computational Physics* 236 (2013), pp. 608–623.

[201] A.M. Soward. “On the Finite amplitude thermal instability of a rapidly rotating fluid sphere”. In: *Geophysical & Astrophysical Fluid Dynamics* 9 (1977), pp. 19–74. DOI: 10.1080/03091927708242315.

[202] E.A. Spiegel and J.P. Zahn. “The solar tachocline”. In: *Astronomy and Astrophysics* 265 (1992), pp. 106–114.

[203] M Steenbeck. “A calculation of the mean electromutive force in an electrically conducting fluid in turbulent motion, under the influence of Coriolis forces”. In: *Z. Naturforsch.* 21 (1966), pp. 369–376.

[204] M. Steenbeck and F. Krause. “On the dynamo theory of stellar and planetary magnetic fields. I. AC dynamos of solar type”. In: *Astron Nachr* 291 (1969), pp. 49–84. DOI: 10.1002/asna.19692910201.

[205] A. M. Stejko et al. “Constraining Global Solar Models through Helioseismic Analysis”. In: *The Astrophysical Journal* 934.2 (Aug. 2022), p. 161. ISSN: 1538-4357. DOI: 10.3847/1538-4357/ac7a44. URL: http://dx.doi.org/10.3847/1538-4357/ac7a44.

[206] J. L. Tassoul. *Stellar Rotation*. Cambridge University Press, 2000. DOI: 10.1017/cbo9780511546044.

[207] J.-L. Tassoul. *Theory of Rotating Stars*. Princeton, U.S.A.: Princeton University Press, 1978.

[208] J. Taylor. “Relaxation and magnetic reconnection in plasmas”. In: *Rev. Mod. Phys.* 58 (1986), p. 741.

[209] J.B. Taylor. “The magneto-hydrodynamics of a rotating fluid and the Earth’s dynamo problem”. In: *Proceedings of the Royal Society of London Series A* 274 (1963), pp. 274–283. DOI: 10.1098/rspa.1963.0130.

[210] R.J. Teed and E. Dormy. “Solenoidal force balances in numerical dynamos”. In: *J. Fluid Mech.* 964 (2023), A26. DOI: 10.1017/jfm.2023.332.

[211] M. J. Thompson et al. “Differential Rotation and Dynamics of the Solar Interior”. In: *Science* 272 (1996), pp. 1300–1305. DOI: 10.1126/science.272.5266.1300.

[212] M.J. Thompson et al. “The Internal Rotation of the Sun”. In: *Annu. Rev. Astron. Astrophys.* 41 (2003). Related online version (cited on 15 March 2005): http://adsabs.harvard.edu/cgi-bin/bib_query?2003ARA&A..41..599T, pp. 599–643.

[213] A. Tilgner. “Spectral methods for the simulation of incompressible flows in spherical shells”. In: *Int. J. Numer. Methods Fluids* 30 (1999), pp. 713–724. DOI: 10.1002/(SICI)1097-0363(19990730)30:6<713::AID-FLD859>3.0.CO;2-Y.

[214] P. Ultre-Guerard et al. “Improving geomagnetic field models for the period 1980–1999 using Oersted data”. In: *Earth, Planets and Space* 50 (1998), pp. 635–640. DOI: 10.1186/BF03352188.

[215] I. Usoskin et al. “Long-term persistence of solar active longitudes and its implications for the solar dynamo theory”. In: *Adv. Space Res.* 40 (2007), pp. 951–958. DOI: 10.1016/j.asr.2006.12.050.

[216] I.G. Usoskin. “A history of solar activity over millennia”. In: *Living Reviews in Solar Physics* 14 (2017). DOI: 10.1007/s41116-017-0006-9.

[217] J. Warnecke. “Dynamo cycles in global convection simulations of solar-like stars”. In: *Astronomy Astrophysics* 616 (2018), A72. DOI: 10.1051/0004-6361/201732413.

[218] J. Warnecke et al. “Numerical evidence for a small-scale dynamo approaching solar magnetic Prandtl numbers”. In: *Nat. Astron.* 7 (2023), pp. 662–668. DOI: 10.1038/s41550-023-01975-1.

[219] J. Warnecke et al. “Solar-like differential rotation and equatorward migration in a convective dynamo with a coronal envelope”. In: *Proceedings of the International Astronomical Union* 8 (2012), pp. 307–312. DOI: 10.1017/S1743921313002676.

[220] J. Wicht and S. Sanchez. “Advances in geodynamo modelling”. In: *Geophys. Astrophys. Fluid Dyn.* 113 (2019), pp. 2–50. DOI: 10.1080/03091929.2019.1597074.

[221] L. Woltjer. “A theorem on force-free magnetic fields”. In: *Proc. Natl. Acad. Sci. U.S.A.* 44 (1958), p. 489.

[222] M.F. Woodard. “Theoretical Signature of Solar Meridional Flow in Global Helioseismic Data”. In: *Solar Phys.* 197 (2000). Related online version (cited on 15 March 2005): http://adsabs.harvard.edu/cgi-bin/bib_query?2000SoPh..197...11W, pp. 11–20.

[223] N.J. Wright, E.R. Newton and P.K.G. et al. Williams. “The stellar rotation-activity relationship in fully convective M dwarfs”. In: *Monthly Notices of the Royal Astronomical Society* 479.2 (2018), pp. 2351–2360. DOI: 10.1093/mnras/sty1670. arXiv: 1807.03304 [astro-ph.SR].

[224] S. Yang et al. “The origin and effect of hemispheric helicity imbalance in solar dynamo”. In: *J. Plasma Phys.* 86 (2020), p. 775860302.

[225] J.I. Yano. “Asymptotic theory of thermal convection in rapidly rotating systems”. In: *Journal of Fluid Mechanics* 243 (1992), p. 103. DOI: 10.1017/s0022112092002659.

[226] N. Yokoi. “Cross helicity and related dynamo”. In: *Geophysical & Astrophysical Fluid Dynamics* 107 (2013), pp. 114–184. DOI: 10.1080/03091929.2012.754022.

[227] N. Yokoi. “Turbulence, Transport and Reconnection”. In: (2020). Ed. by D. MacTaggart and A. Hillier, pp. 177–265. DOI: 10.1007/978-3-030-16343-3_6.

[228] N. Yokoi. “Turbulence, transport and reconnection”. In: *Topics in magnetohydrodynamic topology, reconnection and stability theory* (2020), pp. 177–265.

[229] N. Yokoi and G. Balarac. “Cross-helicity effects and turbulent transport in magnetohydrodynamic flow”. In: *Journal of Physics: Conference Series* 318 (2011), p. 072039. DOI: 10.1088/1742-6596/318/7/072039.

[230] H. Yoshimura. “Solar-cycle dynamo wave propagation”. In: *Astrophys J* 201 (1975), pp. 740–748. DOI: 10.1086/153940.

[231] A. Yoshizawa. “Self-consistent turbulent dynamo modeling of reversed field pinches and planetary magnetic fields”. In: *Physics of Fluids B: Plasma Physics* 2 (1990), pp. 1589–1600. DOI: 10.1063/1.859484.

[232] A. Yoshizawa and N. Yokoi. “Turbulent Magnetohydrodynamic Dynamo for Accretion Disks Using the Cross-Helicity Effect”. In: *The Astrophysical Journal* 407 (1993), p. 540. DOI: 10.1086/172535.

[233] J.-P. Zahn. “Circulation and Turbulence in Rotating Stars”. In: *Astron. Astrophys.* 265 (1992), pp. 115–132.

[234] H. Zhang et al. “A new dynamo pattern revealed by solar helical magnetic fields”. In: *Mon. Notices Royal Astron. Soc.* 402 (2010), pp. L30–L33.

[235] K. K. Zhang and F. H. Busse. “On the onset of convection in rotating spherical shells”. In: *Geophys. Astrophys. Fluid Dyn.* 39 (1987), pp. 119–147. DOI: 10.1080/0309192870820880

[236] J. Zhao and A.G. Kosovichev. “Torsional Oscillation, Meridional Flows, and Vorticity Inferred in the Upper Convection Zone of the Sun by Time-Distance Helioseismology”. In: *Astrophys. J.* 603 (2004). Related online version (cited on 15 March 2005): http://adsabs.harvard.edu/cgi-bin/bib_query?2004ApJ...603..776Z, pp. 776–784.

[237] J. B. Zirker et al. “Global magnetic patterns of chirality”. In: *Solar Physics* 175 (1997), pp. 27–44.

[238] C. Zwaan. “Elements and Patterns in the Solar Magnetic Field”. In: *Annual Review of Astronomy and Astrophysics* 25 (1987), pp. 83–111. DOI: 10.1146/annurev.aa.25.090187.000503.